Investigation of quantum coherence within modal strong coupling systems between localized surface plasmon resonance and Fabry-Pérot nanocavity modes

Thesis by

Yen-En Liu

In Partial Fulfillment of the Requirements

For the Degree of

Doctor of Philosophy

RESEARCH INSTITUTE FOR ELECTRONIC SCIENCE
HOKKAIDO UNIVERSITY
SAPPORO, JAPAN
2026

Dedication

To my family for their endless love and support,

and to my current and former supervisors who insightfully

guide me academically and personally.

Table of contents

Acknowledgements

I would like to express my deepest gratitude to my supervisor, Prof. Hiroaki Misawa, for his invaluable guidance and support throughout my eight years at Hokkaido University (two years in the master's course and six years in the doctoral course). During this period, I have learned countless lessons from him—not only in research but also in how to think as a scientist. He taught me how to identify new research directions from existing studies, design and refine experiments to overcome challenges, interpret results from multiple perspectives to uncover unexpected phenomena, and develop theoretical models to explain experimental findings. Beyond academic guidance, I also acquired extensive technical experience under his supervision. I became proficient in operating advanced facilities such as electron beam lithography, sputtering, atomic layer deposition, photoemission electron microscopy, and transient absorption microscopy—skills that form a solid foundation for my future career in both academia and industry.

I would also like to express my sincere appreciation to Prof. Hiroshi Masuhara and Prof. Teruki Sugiyama from National Yang Ming Chiao Tung University, Taiwan, for recommending me to join Misawa Lab and giving me this invaluable opportunity to study in Japan. All three professors—Prof. Misawa, Prof. Masuhara, and Prof. Sugiyama—have kindly offered me career advice and personal guidance, helping me plan my future with greater clarity and confidence.

From Misawa Lab, I would like to thank Prof. Xu Shi, who frequently discussed experiments with me and provided valuable technical advice whenever I encountered difficulties. I am also grateful to Prof. Kosei Ueno and Prof. Tomoya Oshikiri for their insightful comments and suggestions, which greatly improved the quality and efficiency of my research. I also appreciate Prof. Quan Sun for his experimental assistance, particularly in the photoemission electron microscopy measurements.

My heartfelt thanks go to Ms. Yumiko Yamaguchi, the secretary of Misawa Lab, for her continuous help with various administrative matters, including visa applications, purchase orders, and conference reimbursements. I am also deeply thankful to all the

members of Misawa Lab for their kindness, friendship, and assistance over the years.
The postdoctoral researchers—Ms. J. Li, Mr. He, Mr. Zu, Ms. Qiao and Mr. Y. Li—offered valuable feedback during experimental discussions.
My colleagues in the same cohort—Mr. Jo, Mr. Tatsumi, and Mr. Shimizu—shared many lectures and experiences with me.
My seniors—Mr. Nakamura, Ms. Y. Cao, Mr. Wang, Ms. Zhang, and Mr. Yamada—generously supported me whenever I faced difficulties.
I would also like to thank Mr. E. Cao, who joined the team half a year after me; we often conducted experiments together and supported each other.
Finally, I am grateful to my juniors—Mr. Suganami, Mr. Yamada, Ms. Onishi, Mr. Kudo, Mr. Furuya, Mr. Arai, Ms. Fan, Mr. Kato, Mr. Kaneko, Mr. Araki, Mr. Ishihara, and Mr. Kumagai—for bringing joy and warmth to my life in the laboratory.
I would also like to extend my appreciation to the professors and staff members of the Research Institute for Electronic Science and the Graduate School of Information Science and Technology. Special thanks to Prof. Mamoru Hashimoto, who kindly allowed me to continue my research at Hokkaido University after Prof. Misawa's retirement, and to Prof. Yasutaka Matsuo, who permitted me to keep using the facilities in RIES. I am also grateful to Mr. Onishi, Ms. Nakano, Ms. Hirai, Ms. Mori, and Mr. Takei for their generous experimental support and technical guidance, from which I learned a great deal.
Finally, I would like to acknowledge the Honjo International Scholarship Foundation, the DX Fellowship from Hokkaido University, and Prof. Misawa for their generous financial support, which allowed me to pursue my research without financial concern. Without these supports—and the unconditional love of my family—I would not have been able to complete my research and doctoral studies.
Once again, I sincerely thank all of you for your support and encouragement throughout this journey.

Thesis Abstract

Artificial photosynthesis is a promising approach to convert solar energy into storable chemical fuels. Over the past decades, numerous efforts have been devoted to realizing efficient artificial photosynthetic systems. Among them, Shi et al. demonstrated a modal strong coupling photoanode composed of plasmonic nanoparticles on a Fabry-Pérot nanocavity built with a TiO_2 semiconductor and an Au mirror. This configuration significantly extended the operational wavelength range into the visible and near-infrared regions and remarkably enhanced the quantum efficiency of water splitting compared with conventional plasmonic photoanodes.

In this study, I employed well-designed Au nanostructures instead of randomly distributed nanoparticles to construct controlled modal strong coupling systems. By precisely tuning their structural parameters, the detailed mechanisms governing modal strong coupling—particularly the role of quantum coherence—were systematically investigated.

Chapter 2 describes the fabrication of modal strong coupling systems composed of Au nanodisks with various particle number densities. Their optical spectra confirmed the achievement of the strong coupling regime. Interestingly, unlike conventional plasmonic structures where absorption increases monotonically with the number of absorbers, both the absorption and near-field intensities of the modal strong coupling structures exhibited saturation behavior with increasing particle number density. Moreover, the splitting energy between the upper and lower branches deviated positively from the classical square-root dependence on particle number density at high values. These unconventional trends motivated further investigation into the role of quantum coherence, discussed in the following chapter.

Chapter 3 explores the apparent quantum coherence in the hot-electron injection process from Au nanodisks into the TiO_2 layer. The degree of coherence was found to increase with PND for both branches—a dependence absent in conventional plasmonic systems. Combined with photoemission electron microscopy observations, a mechanism of quantum coherence-assisted hot-electron injection was proposed. Under

modal strong coupling conditions, plasmonic nanostructures within a certain coherence area can share energy through the nanocavity. This behavior explains both the absorption saturation and the positive deviation of the splitting energy. Furthermore, when fast-damping sites that efficiently inject electrons exist within the coherence area, the shared energy converges toward these sites, enhancing the apparent quantum efficiency. Photoelectrochemical measurements further confirmed that this efficiency enhancement translates into improved single-proton oxidation reaction performance.

Chapter 4 investigates the dephasing effect by incorporating Au-nanotriangles into Au-nanodisks arrays. Because Au-NTs exhibit faster dephasing than Au-NDs, increasing the percentage of triangles led to a reduction in splitting energy and broadening of both excitation branches. Interestingly, the apparent quantum efficiency showed a branch-asymmetric dependence on the percentage of triangles, suggesting complementary functional roles between Au-nanodisks and Au-nanotriangles mediated by quantum coherence.

Chapter 5 experimentally determined the dephasing times of the mixed structures, revealing a gradual decrease with increasing percentage of triangles for both branches. Notably, under upper-branch excitation, the dephasing time exhibited a drastic drop at high triangle ratios. Near-field simulations showed branch-dependent spatial distributions: under lower-branch excitation, the fields were delocalized across nanostructures, with hot spots concentrated at the sharp tips of Au-nanotriangles—efficient sites for hot-electron generation. Under upper-branch excitation, however, the fields were strongly localized along the edges of Au-nanotriangles, where hot-electron generation is less efficient. These results led to the conclusion that the sharp tips of Au-nanotriangles act as reaction centers, while the long-dephasing Au-nanodisks function as optical antennas. The interplay between coherence-mediated energy sharing and dephasing dynamics gives rise to the observed asymmetric apparent quantum efficiency dependence on the percentage of triangles.

Chapter 6 summarizes the findings and discusses future perspectives. Overall, this work demonstrates that quantum coherence plays a central role in governing energy transfer and hot-carrier dynamics in modal strong coupling systems. A clear understanding of

coherence effects—especially the influence of dephasing and near-field distributions—provides a foundation for controlling and optimizing hot-electron transfer. Based on these insights, next-generation modal strong coupling photoelectrodes can be rationally designed to achieve dramatically enhanced efficiencies in artificial photosynthesis, paving the way toward practical and scalable solar-to-chemical energy conversion.

Chapter 1

Introduction

1.1 Background

1.1.1 Utilization of solar energy

Achieving carbon neutrality by 2050 has been established as a critical global objective by multiple international organizations, including the United Nations and the International Energy Agency, in order to mitigate the greenhouse effect and prevent irreversible climate change. Despite rapid advances in renewable technologies over the past decades, fossil fuels—including coal, oil, and natural gas—still dominate the global energy portfolio. According to recent statistics, fossil fuels account for approximately 60% of electricity generation worldwide (**Figure 1.1**)[1], a figure that has only gradually decreased from nearly 70-80% at the beginning of the 21st century. This persistent dependence illustrates the enormous challenge of transitioning to a low-carbon society within the coming decades.

Excluding nuclear power, which contributes around 10% of global electricity but is often limited by safety concerns, waste disposal issues, and high capital costs, renewable energy sources collectively supply only about 30% of the electricity demand.

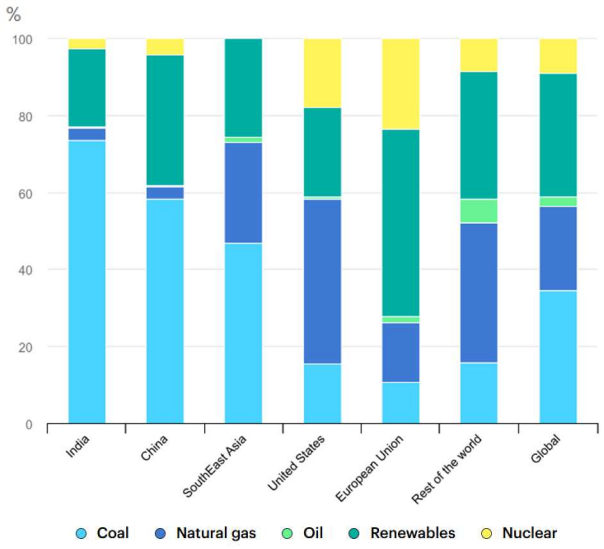

Figure 1.1 Distribution of power generation by energy source[1].

Among them, hydropower represents the most mature technology, but its expansion potential is constrained by geographical and ecological limitations. Wind power has grown rapidly in many regions, yet it remains highly intermittent and location dependent. Solar energy, in contrast, is virtually inexhaustible and universally accessible, making it uniquely attractive for large-scale decarbonization.

From a resource perspective, the amount of solar energy reaching the Earth's surface far exceeds human consumption. It is estimated that the solar flux incident on Earth is approximately 1.7×10^{17} W, which is more than 10,000 times the current global energy demand. Even harnessing a tiny fraction of this resource with sufficient efficiency would be adequate to sustain human civilization. As a result, solar energy has been regarded as the most abundant renewable energy source, representing more than 99% of the total renewable energy available on Earth (**Figure 1.2**)[2,3]. However, its effective utilization remains a central technological challenge.

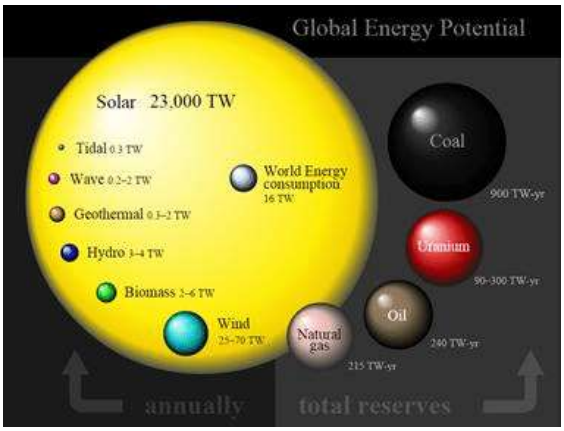

Figure 1.2 Proportion of solar energy in the global energy potential[3].

Currently, most commercial solar energy conversion systems are based on semiconductor devices. Photovoltaic (PV) solar cells, photoelectrodes for solar fuel production, and photocatalysts for environmental remediation are all designed to directly convert solar photons into electricity or chemical fuels. Despite their success, these technologies primarily exploit the ultraviolet (UV) portion of sunlight due to the wide bandgap of many semiconductors. Semiconductors such as TiO_2, one of the most studied materials since the pioneering work of Fujishima and Honda in 1972, absorb

strongly in the UV but poorly in the visible and infrared regions[4]. Building upon this foundation, subsequent studies demonstrated that TiO_2 thin films fabricated via the sol-gel method exhibit improved photoelectrochemical (PEC) properties under UV illumination, highlighting the potential of material engineering in enhancing photocatalytic activity[5,6]. However, this characteristic still severely limits their efficiency, because UV photons account for only ~5% of the solar spectrum. By contrast, visible light contributes nearly 48%, and infrared light accounts for about 47% (**Figure 1.3**). Consequently, a vast majority of solar photons remain unexploited in traditional systems.

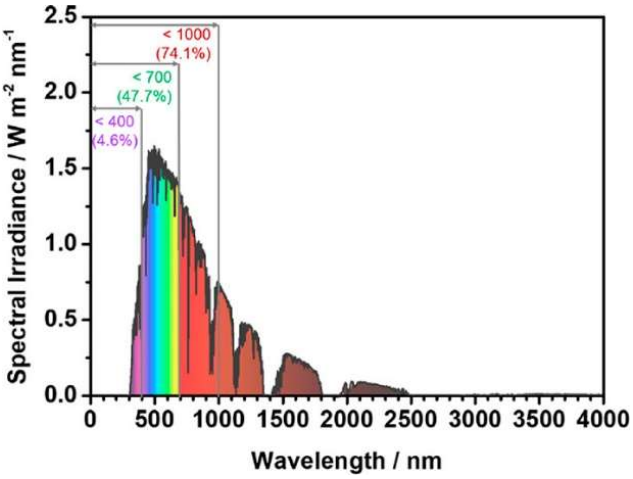

Figure 1.3 Solar spectrum and the corresponding energy composition[2].

The efficiency gap between the theoretical potential of solar energy and its practical utilization is further illustrated by the Shockley–Queisser limit[7], which predicts a maximum efficiency of ~33% for a single-junction solar cell under standard illumination. While modern silicon-based PV cells have achieved record efficiencies of ~26%, they are still fundamentally constrained by spectral mismatch: photons with energies below the semiconductor bandgap cannot be absorbed, while those with much higher energies generate excess heat rather than usable electricity. This mismatch underscores the importance of strategies that can extend absorption into the visible and infrared ranges or that can utilize high-energy photons more efficiently.

Given its universality, abundance, and the rapid pace of technological development, solar energy remains one of the most promising candidates for achieving carbon

neutrality. However, its intermittency and low storage compatibility mean that solar energy alone cannot guarantee reliable energy supply. Therefore, a central research focus has shifted toward not only improving solar-to-electric conversion but also coupling solar energy with chemical processes that allow for energy storage, such as **artificial photosynthesis**. By addressing both efficiency and storage challenges, solar energy may ultimately transition from a supplementary energy source to the cornerstone of a sustainable energy future.

1.1.2 Artificial photosynthesis

In the context of solar energy utilization, PV solar cells are currently the most widely recognized and commercially successful technology, largely due to their continuous improvement in efficiency, cost reduction, and large-scale deployment[8]. Nevertheless, solar cells primarily provide electrical power, and the direct conversion of sunlight into electricity poses inherent challenges for long-term energy storage. Electricity is a high-grade energy form but is difficult to store efficiently and economically on the scale required to balance daily and seasonal fluctuations in solar irradiance. Technologies such as lithium-ion batteries[9] or other electrochemical storage systems can serve as temporary solutions, yet their limited lifetime, high cost, and dependence on rare materials present significant obstacles to their universal adoption. As a consequence, even though solar energy is the most abundant renewable energy resource on Earth, the issue of its intermittent availability—particularly its complete absence during the night—remains a fundamental barrier to its widespread utilization in meeting global energy demands.

Artificial photosynthesis has emerged as a promising alternative strategy to address this storage issue by mimicking the basic principles of natural photosynthesis. Instead of directly producing electricity, artificial photosynthesis converts solar energy into chemical energy that can be stably stored in the form of chemical compounds. For example, in artificial water splitting, incident photons are used to generate energetic charge carriers that drive the decomposition of water into hydrogen and oxygen (**Figure 1.4**)[10]. The molecular hydrogen produced can subsequently be stored, transported, and

utilized either as a clean fuel through combustion or in fuel cells, or as an essential feedstock for the chemical industry. In this way, artificial photosynthesis offers a pathway not only for sustainable fuel production but also for decarbonizing energy-intensive industrial processes that rely heavily on fossil resources.

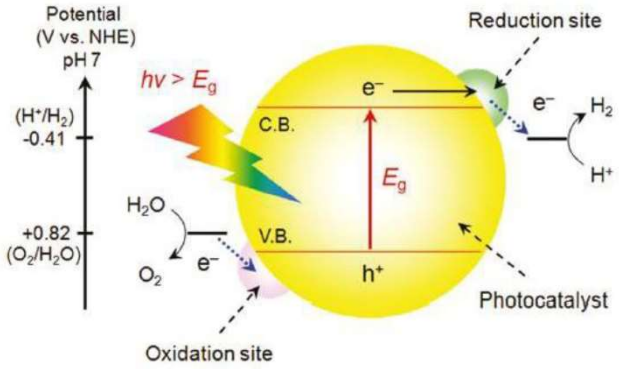

Figure 1.4 Schematic illustration of artificial water splitting[10].

Historically, the concept of artificial photosynthesis can be traced back to the pioneering work[4] of Fujishima and Honda in 1972. Inspired by the Hill reaction in natural photosynthesis[11], they demonstrated that a semiconductor photoelectrode—specifically, a TiO_2 single crystal—could drive PEC water splitting under ultraviolet light irradiation. This seminal work established the foundation for PEC research and provided the proof-of-concept that solar energy could be directly converted into storable chemical fuels. Since then, the scope of artificial photosynthesis has expanded beyond water splitting to include a wide range of redox reactions, such as nitrogen fixation to produce ammonia[12], carbon dioxide reduction to generate carbon-based fuels or value-added chemicals[13], and the redox transformation of organic molecules for fine chemical synthesis[14]. Each of these reactions holds significant social relevance, with ammonia being indispensable for fertilizers, carbon dioxide reduction directly addressing climate change, and organic redox reactions enabling green chemistry applications.

Despite these achievements, semiconductor-based artificial photosynthetic systems still encounter several intrinsic challenges that limit their overall efficiency and scalability. A primary limitation arises from the light absorption characteristics of semiconductors. Many conventional semiconductors, such as TiO_2, have wide bandgaps that restrict

their absorption primarily to the ultraviolet region, which accounts for less than 6% of the solar spectrum. As a result, the vast majority of visible and infrared (IR) photons, which constitute over 90% of solar energy, cannot be effectively harvested. On the other hand, narrowing the bandgap to extend light absorption into the visible region often results in reduced redox potential of photogenerated carriers, thereby compromising the driving force required for targeted chemical reactions. This trade-off between light absorption and carrier energy represents a fundamental material constraint.

Another critical issue is the rapid recombination of photogenerated charge carriers. Upon photon absorption, electron-hole pairs are created, but in many semiconductors, these excited carriers recombine on ultrafast timescales before reaching the surface to participate in redox reactions. This loss pathway significantly decreases the quantum efficiency of the overall process. Additionally, surface defects and trap states exacerbate recombination by acting as nonradiative decay centers, further reducing carrier lifetimes. Even when carriers successfully reach the interface, the catalytic activity of the bare semiconductor surface is often insufficient to sustain efficient chemical transformations. This necessitates the introduction of co-catalysts, which play essential roles in lowering activation barriers, providing reaction-specific active sites, and stabilizing intermediates. Typical examples include platinum nanoparticles for hydrogen evolution and transition metal oxides or hydroxides for oxygen evolution. While these co-catalysts enhance reaction kinetics, they can also introduce additional pathways for charge recombination or alter interfacial energetics in unfavorable ways, resulting in complex trade-offs.

Moreover, for overall water splitting, the energetic positions of the semiconductor band edges must appropriately straddle the redox potentials of both water oxidation (1.23 V vs. NHE) and hydrogen reduction (0 V vs. NHE). This stringent requirement dramatically narrows the pool of suitable semiconductor candidates. For instance, materials with adequate oxidative power may lack sufficient reductive potential, while others with favorable band alignments may suffer from instability under aqueous PEC conditions due to photocorrosion. These issues collectively highlight the multifaceted challenges in designing efficient and durable semiconductor photoelectrodes.

To overcome these limitations, researchers have investigated a variety of strategies to broaden light absorption and improve charge utilization. Dye sensitization is one such approach, in which organic or organometallic dye molecules are anchored onto the semiconductor surface[15]. These dyes, often inspired by natural photosynthetic pigments, extend the absorption range into the visible spectrum and inject excited electrons into the semiconductor conduction band (**Figure 1.5**)[16]. While this technique has enabled significant progress, issues of dye photostability and long-term device durability remain unresolved. In addition, various doping strategies have been explored to sensitize TiO_2 itself toward visible-light absorption[17-20]. By introducing nonmetal dopants (such as N, C, or S) or transition metal ions into the TiO_2 lattice, localized energy states are created within the bandgap, allowing sub-bandgap excitation under visible illumination. Although such modifications effectively extend the absorption range, they often introduce recombination centers that compromise charge transport and overall device efficiency. Another avenue involves photon upconversion, where low-energy photons in the IR region are absorbed by specialized materials and subsequently re-emitted as higher-energy photons capable of exciting the semiconductor[21]. Similarly, two-photon excitation techniques exploit nonlinear optical processes to absorb two lower-energy photons simultaneously, thereby reaching an excitation energy equivalent to a higher-

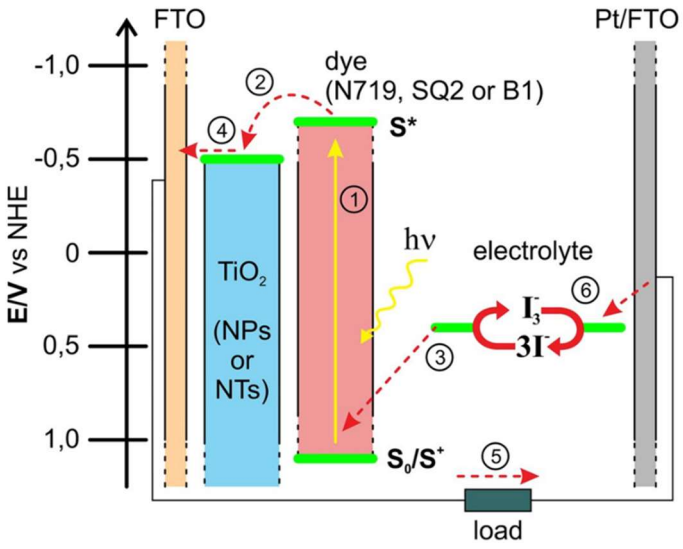

Figure 1.5 Schematic illustration of the PEC reaction using a dye-sensitized semiconductor[16].

energy photon[22]. Both strategies, while conceptually powerful, typically suffer from low conversion efficiencies under solar illumination intensities, limiting their practical applicability.

In parallel, much effort has been devoted to engineering co-catalysts with improved performance. Traditional co-catalysts primarily function to reduce kinetic barriers and stabilize reaction intermediates (**Figure 1.6**)[23], but their influence is generally restricted to surface reactions. In recent years, however, the emergence of plasmonic nanoparticles has revolutionized the role of co-catalysts in PEC systems. Noble metal nanoparticles, such as Au, Ag, and Cu, exhibit **localized surface plasmon resonance** (**LSPR**), a collective oscillation of conduction electrons that strongly couples with incident visible and near-infrared (NIR) light. Unlike conventional co-catalysts, plasmonic nanoparticles can contribute not only catalytically but also optically by enhancing light absorption in regions where semiconductors are intrinsically weak. This dual functionality is particularly attractive because it simultaneously addresses two of the most critical challenges in artificial photosynthesis: limited light harvesting and inefficient interfacial charge transfer.

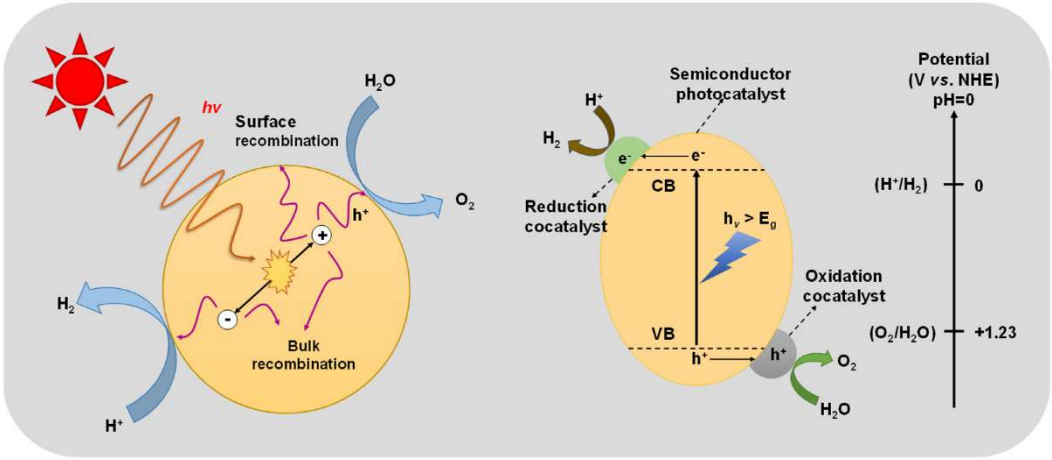

Figure 1.6 Schematic illustration of co-catalyst used in the water splitting reaction[23].

When integrated onto semiconductor photoelectrodes, plasmonic nanoparticles have been shown to extend the spectral response into the visible and IR domains while maintaining the intrinsic electronic properties of the underlying semiconductor.

Furthermore, their strong electromagnetic near-fields can locally enhance excitation rates, while hot carriers generated through plasmon decay can participate directly in redox chemistry or be injected across metal-semiconductor interfaces. Consequently, plasmonic nanoparticles represent a new paradigm in photoelectrode design, acting as multifunctional co-catalysts that both accelerate surface reactions and significantly broaden the light-harvesting window. This concept has enabled the development of tunable, visible-light-responsive photoelectrodes that mark a substantial departure from the limitations of traditional semiconductor systems and lay the groundwork for plasmon-assisted artificial photosynthesis.

1.1.3 Localized surface plasmon resonance

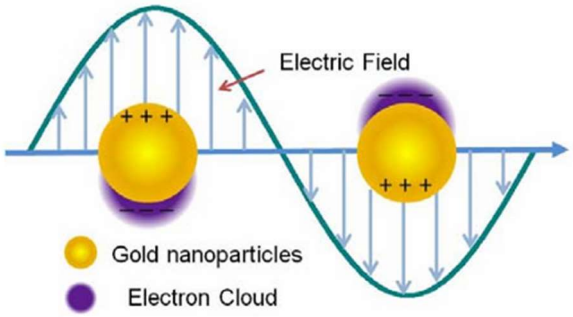

Figure 1.7 Schematic illustration of localized surface plasmon resonance[25].

As mentioned, LSPR is a fundamental optical phenomenon that arises from the collective oscillation of conduction band electrons in metallic nanostructures when they are driven by incident electromagnetic radiation (**Figure 1.7**)[24,25]. In contrast to bulk plasmons, which represent longitudinal charge-density waves propagating through a continuous electron gas within extended metallic media, LSPR is spatially confined to the surface of metallic nanoparticles. This confinement leads to highly localized electromagnetic field enhancements at the nanoscale and produces unique light-matter interactions that are not accessible in bulk systems. Because of these distinctive features, LSPR has attracted significant attention in recent decades across multiple fields, including sensing[26-28], surface-enhanced spectroscopy[29-31], biomedical imaging[32-34], photocatalysis[35-38], and solar energy conversion[39-43].

The resonance frequency of LSPR is determined by the interplay between the restoring force acting on the displaced conduction electrons and the driving frequency of the incident light. Importantly, unlike intrinsic semiconductor band-to-band transitions, the plasmon resonance is not fixed but is highly tunable by modifying the physical and chemical characteristics of the nanostructures. Key parameters that dictate the LSPR response include the particle size, morphology (e.g., spheres, rods, cubes, bipyramids, shells), and composition (typically noble metals such as Au, Ag, and Cu) (**Figure 1.8**)[44,45]. Furthermore, the dielectric constant of the surrounding environment strongly influences the resonance frequency, providing an external handle to modulate optical response simply by altering the nanoparticle embedding medium[46]. This high degree of tunability makes LSPR an exceptionally versatile tool for engineering light-matter interactions across the visible and NIR regions, thereby addressing one of the principal limitations of conventional semiconductors in solar energy conversion—their inherently weak absorption in these spectral windows.

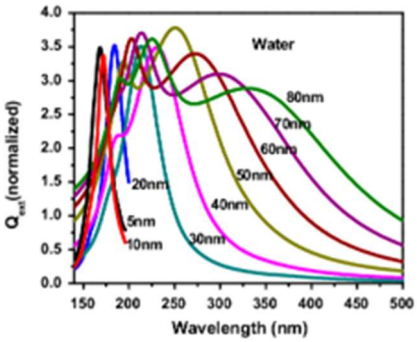

Figure 1.8 Dependence of LSPR wavelength on nanoparticle size[45].

From an optical perspective, metallic nanoparticles can exhibit both strong absorption and scattering cross sections under LSPR excitation. Small nanoparticles (typically <20 nm) are dominated by absorption processes due to enhanced confinement of oscillating electrons, whereas larger nanoparticles (>50 nm) display more pronounced scattering. The relative balance between absorption and scattering is crucial in designing plasmonic systems for different applications. For example, in photocatalysis and artificial photosynthesis, absorption-dominated nanoparticles are often more desirable because they efficiently convert incident photons into energetic carriers (so-called “hot

electrons" and "hot holes")[47,48], which can participate directly in chemical reactions (**Figure 1.9**)[49]. On the other hand, scattering-dominated nanoparticles are useful in solar cell applications, where their ability to redirect and concentrate light enhances the effective optical path length in thin-film absorber layers.

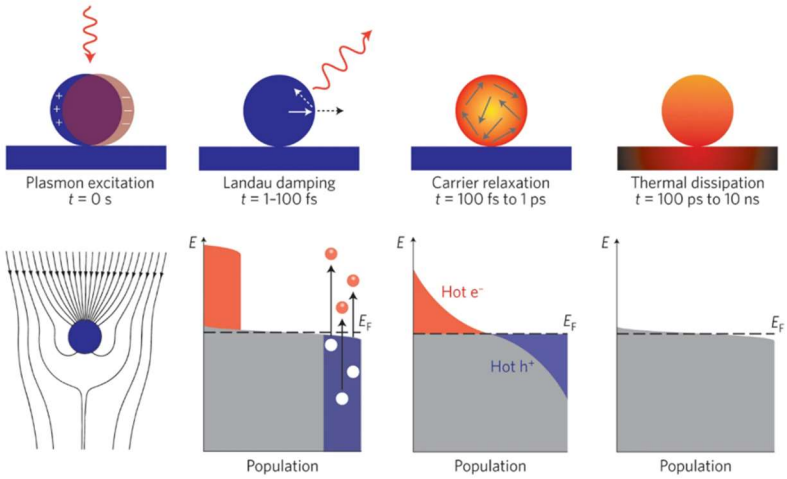

Figure 1.9 Schematic illustration of the photoexcitation and relaxation processes[49].

One of the most celebrated consequences of LSPR is the generation of extremely intense local electromagnetic fields near the nanoparticle surface, particularly at sharp features or tips due to the "lightning rod effect"[50]. These local field enhancements can exceed several orders of magnitude compared to the incident field, giving rise to phenomena such as surface-enhanced Raman scattering (SERS)[51-53] and surface-enhanced infrared absorption (SEIRA)[54-56]. In photocatalysis, such local field enhancements increase the excitation probability of nearby molecules or semiconductors, effectively amplifying light-matter interactions beyond what is achievable by intrinsic absorption processes alone.

In addition to radiative decay channels such as scattering, LSPR can also relax through non-radiative decay processes. When the coherent plasmon oscillation dephases, the collective electron motion dissipates its energy into non-equilibrium electron-hole pairs, commonly referred to as "hot carriers." These hot electrons (and the corresponding hot holes) are distinguished from thermalized carriers by their elevated energies relative to the Fermi level of the metal. Because they occupy non-equilibrium states, hot carriers

possess excess kinetic energy and short lifetimes, typically on the order of tens to hundreds of femtoseconds before thermalization with the Fermi sea. The generation and utilization of hot carriers provide a direct route to harness plasmon energy for driving PEC processes.

For hot electrons to contribute to chemical reactions in a hybrid plasmonic-semiconductor system, their energies must be sufficiently high to overcome the interfacial Schottky barrier and be injected into the semiconductor conduction band. Once injected, these carriers can migrate within the semiconductor and participate in reduction reactions either at the semiconductor-electrolyte interface or via external circuitry in a PEC cell. Meanwhile, the holes left behind in the metallic nanoparticle after hot electron extraction can serve as oxidation centers, enabling the bifurcation of redox processes across spatially separated sites. This synergistic mechanism not only extends the light absorption window of the semiconductor but also introduces new catalytic pathways mediated by plasmon decay dynamics.

It is worth emphasizing that the efficiency of hot-carrier generation and transfer depend strongly on several factors, including the choice of metal, particle geometry, interface engineering, and the energy alignment of the metal-semiconductor junction. For example, Au and Ag are the most widely studied plasmonic metals due to their favorable dielectric functions and relatively low intrinsic damping, which lead to sharp and intense LSPR features in the visible range. Cu, while more abundant and less costly, suffers from rapid oxidation that compromises its stability under operational conditions. Recent studies have also explored aluminum for ultraviolet plasmonics[57] and various alloy systems to tailor both stability and spectral response[58]. From the semiconductor side, band-edge alignment relative to the Fermi level of the plasmonic nanoparticle is a decisive factor in determining whether hot electrons can be efficiently injected and whether back-transfer processes can be suppressed. Careful interface engineering, such as inserting ultrathin oxide layers[59] or constructing heterostructures[60], has been demonstrated to significantly improve carrier injection yields.

Owing to these unique physical properties, LSPR has been extensively employed in applications that require strong and tunable light-matter interactions. In sensing, LSPR-based platforms exploit shifts in resonance frequency in response to changes in the local dielectric environment, enabling highly sensitive detection of biomolecules, gases, or chemical species down to the single-molecule level[61,62]. In spectroscopy, LSPR-induced field enhancement forms the basis of SERS, which revolutionized the detection of trace analytes (**Figure 1.10**)[63,64]. In the biomedical domain, plasmonic nanoparticles have been used for photothermal therapy, where localized heating induced by plasmon decay selectively destroys cancer cells[65-67]. In energy-related fields, plasmonic nanostructures have been incorporated into photovoltaic and photoelectrochemical systems to extend spectral response, enhance light absorption, and introduce new reaction pathways mediated by hot carriers[68-71].

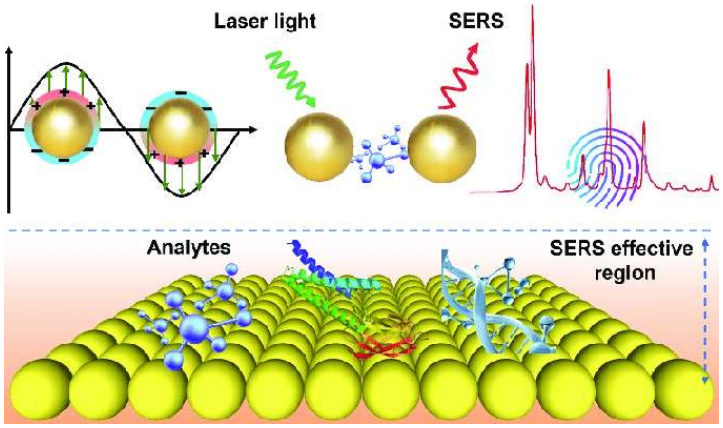

Figure 1.10 Schematic illustration of the mechanism of SERS for detection of analytes[64].

In the context of artificial photosynthesis, the role of LSPR is particularly significant. Conventional semiconductors face severe limitations in harvesting visible and NIR photons, constituting the majority of the solar spectrum. By integrating plasmonic nanoparticles with semiconductor photoelectrodes, it becomes possible to not only enhance optical absorption in these critical spectral regions but also to leverage hot-carrier dynamics to directly participate in redox chemistry. In a typical PEC setup, incident light excites the LSPR of metallic nanoparticles deposited on a semiconductor substrate. The dephasing of the plasmon generates hot electrons, which, if possessing

sufficient energy, can overcome the Schottky barrier and be injected into the semiconductor conduction band. These injected carriers can then drive reduction processes such as hydrogen evolution or carbon dioxide reduction. Concurrently, the holes remaining in the plasmonic nanoparticles can serve as oxidative centers, enabling reactions such as water oxidation. This dual-functionality—light harvesting and catalytic activity—places LSPR at the forefront of strategies for improving solar-to-chemical energy conversion efficiency[72].

Overall, LSPR represents a powerful and versatile mechanism for overcoming the intrinsic limitations of semiconductor-based artificial photosynthesis. Through the careful design of plasmonic nanostructures and their integration with semiconductors, it becomes possible to extend solar energy utilization well beyond the UV domain, accelerate interfacial charge transfer, and introduce new catalytic pathways. These attributes collectively underscore the transformative potential of LSPR in developing next-generation photoelectrodes and PEC cells for sustainable fuel and chemical production.

1.1.4 LSPR in Artificial Photosynthesis

The integration of plasmonic nanoparticles with semiconductor photoelectrodes has opened a promising pathway for advancing the efficiency of artificial photosynthesis. Among the pioneering works, Misawa and coworkers has consistently demonstrated that plasmonic nanoparticles are not merely passive light scatterers but active mediators that reshape interfacial photophysics and catalysis (**Figure 1.11**)[73]. A representative

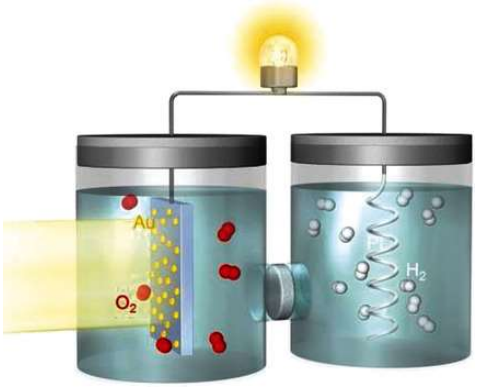

Figure 1.11 Schematic illustration of the LSPR-assisted artificial water splitting[73].

example is the incorporation of Au nanorods onto TiO_2 photoanodes, which enabled visible-to-NIR-driven water oxidation with significantly reduced overpotentials[74]. In these systems, the LSPR acted as an optical antenna that concentrated incident light at the semiconductor interface while simultaneously generating hot carriers through non-radiative decay. Remarkably, Misawa's group showed that the hot holes generated in Au nanorods could participate in the challenging four-electron oxidation of water to O_2, thereby achieving stoichiometric oxygen evolution with high efficiency under sub-bandgap illumination. This work provided direct evidence that plasmonic nanostructures can extend semiconductor functionality far beyond its intrinsic bandgap limitations.

Beyond water oxidation, Misawa and coworkers pushed the scope of plasmon-assisted photocatalysis into chemically demanding multi-electron processes. A striking demonstration was the achievement of visible-light-driven nitrogen fixation by constructing Au/TiO_2 hybrid electrodes (**Figure 1.12**)[75]. Here, plasmon-derived hot carriers were funneled into the reduction of N_2, a reaction that conventionally requires harsh conditions and is nearly inaccessible under direct semiconductor excitation. The realization of nitrogen fixation under mild illumination underscored the ability of

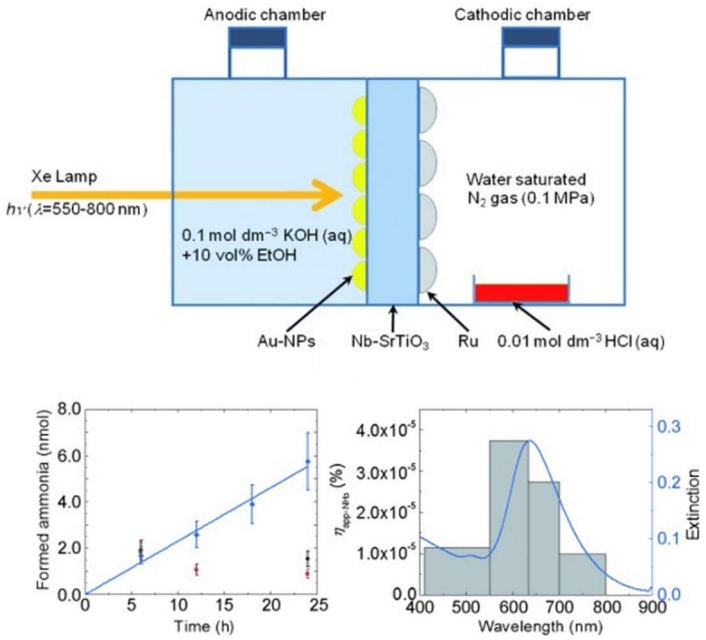

Figure 1.12 LSPR assisted visible-light-driven nitrogen fixation[75].

plasmon-semiconductor interfaces to unlock new chemical pathways that are energetically or kinetically unfavorable in traditional photocatalytic systems.

A consistent theme across Misawa's research is the importance of rational structural design in maximizing plasmonic functionality. His group systematically investigated how nanoparticle size, aspect ratio, interparticle spacing, and surface coverage dictate the resonance wavelength, field intensity, and hot-carrier generation efficiency[39,76,77]. By tuning these parameters, they demonstrated modular spectral engineering, in which the absorption properties of photoelectrodes could be tailored to match specific regions of the solar spectrum. In this context, plasmonic nanoparticles were redefined from being viewed as auxiliary enhancers to becoming integral design elements of PEC architectures. The outcome was a new conceptual framework in which plasmonic nanostructures function simultaneously as light harvesters, charge-separation mediators, and catalytic reaction centers.

Nevertheless, despite these advances, two fundamental issues persisted. First, the ultrafast relaxation dynamics of hot carriers restricted the proportion of carriers that could be harvested before energy dissipation, inherently limiting quantum yields. Second, long-term stability of plasmonic structures under operational aqueous conditions remained a challenge for scalable implementation. Addressing these limitations, Misawa's group began to explore nanophotonic strategies that go beyond single-particle plasmonics. In a seminal breakthrough, they demonstrated a Fabry-Pérot (FP) nanocavity-assisted plasmonic photoanode[78]. By coupling the LSPR mode of Au nanoparticles with the optical modes of an FP nanocavity, the system entered the regime of **modal strong coupling**. This hybridization not only enhanced light absorption but also fundamentally altered the carrier dynamics, leading to a substantial increase in light-to-electron conversion efficiency and improved quantum yields in water splitting. This work marked a paradigm shift, indicating that the frontier of plasmonic artificial photosynthesis lies in manipulating light-matter interactions at the quantum level.

1.1.5 Modal strong coupling

In general, when describing the interaction between two physical systems, one most

often encounters the weak coupling regime. In this limit, the properties of the coupled entity can be approximated as a superposition of the individual components, possibly with minor spectral perturbations arising from their mutual interaction. For instance, if molecule A weakly interacts with molecule B, the absorption spectrum of the combined system can be regarded as a linear sum of the spectra of A and B, perhaps with small shifts due to dipole-dipole interactions. Importantly, in weak coupling, the identity of the subsystems remains intact, and the energy exchange between them is unidirectional and irreversible, such as in the case of fluorescence quenching[79] or Förster resonance energy transfer[80].

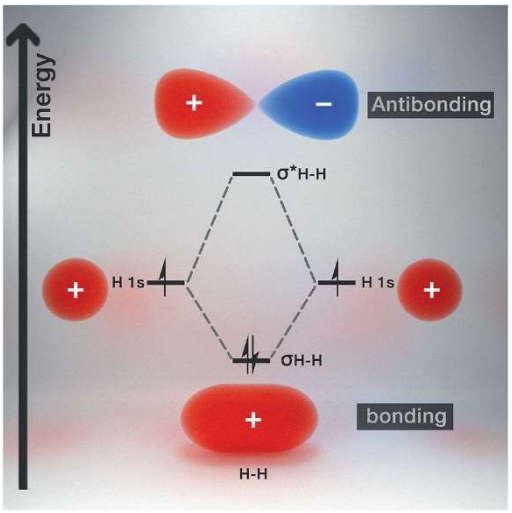

Figure 1.13 Diagram of the molecular orbitals of the hydrogen molecule[85].

By contrast, strong coupling arises when two subsystems with comparable resonance energies interact so intensely that their eigenstates are no longer separable[81-84]. Instead, they hybridize to form new eigenmodes that are coherent superpositions of the original excitations. The most explicit spectroscopic signature of this regime is Rabi splitting or mode splitting, in which the absorption or extinction spectrum of the coupled system reveals two distinct peaks separated by an energy gap proportional to the coupling strength. A useful analogy is the formation of the hydrogen molecule (H_2): when two atomic orbitals with nearly identical energies overlap, they reorganize into a bonding orbital at lower energy and an antibonding orbital at higher energy (**Figure 1.13**)[85]. Similarly, in strong light-matter coupling, one obtains hybrid states usually referred to

as the lower branch and the upper branch. Crucially, in this regime, energy can be exchanged back and forth coherently and reversibly between the subsystems on timescales much faster than their intrinsic dissipation rates, so that the system must be regarded as a collective entity rather than independent components.

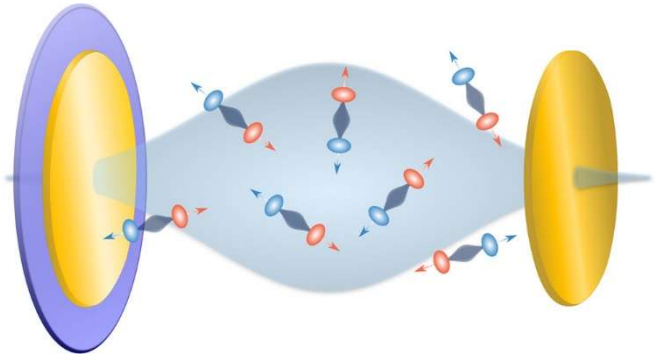

Figure 1.14 Schematic illustration of ensemble strong coupling[90].

The modern field of strong light-matter coupling was pioneered by Thomas Ebbesen and coworkers, whose seminal contributions established the conceptual and experimental foundations. In a series of studies, Ebbesen's group embedded molecular excitonic materials inside high-quality optical cavities[86,87] and demonstrated ensemble strong coupling between cavity photon modes and the electronic excitations of molecules (**Figure 1.14**)[88,90]. A key theoretical result from their work is that the coupling strength can be quantified by the Rabi splitting energy, expressed as:

$$\hbar\Omega_R = 2\sqrt{N}d\sqrt{\frac{\hbar\omega}{2\varepsilon_0 V}} \times \sqrt{n_{ph}+1}$$

where $\hbar\Omega_R$ denotes the Rabi splitting energy characterizing the light-matter coupling strength, N is the number of the molecules in phase in the cavity, d is the transition dipole moment, $\hbar\omega$ is the cavity resonance (or transition) energy, ε_0 is the vacuum permittivity, V is the optical mode volume and n_{ph} is the number of photons present in the cavity[89].

This expression highlights that the collective coupling strength scales with the square root of the number of oscillators ($\sqrt{N}$), reflecting the cooperative enhancement arising from coherent interactions between a molecular ensemble and the confined photon field.

Such scaling provides a clear explanation for why macroscopic molecular systems can exhibit Rabi splitting on the order of several hundred meV, which are readily observable even under ambient, room-temperature conditions.

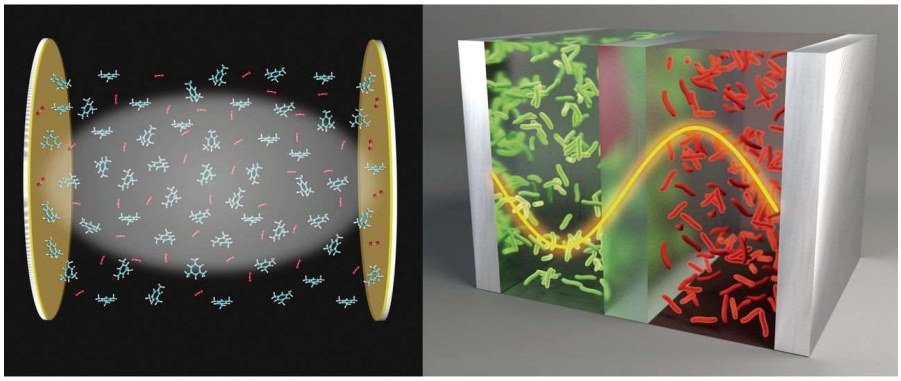

Figure 1.15 Schematic illustration of modified molecular processes under strong coupling[92].

Beyond the spectroscopic manifestations, Ebbesen and collaborators revealed that ensemble strong coupling can profoundly reshape photophysical and chemical landscapes. For example, they showed that molecular emission lifetimes, energy transfer pathways, and even photochemical reaction rates could be modified under strong coupling conditions[90,91]. In particular, the suppression of certain reaction channels was observed when molecular excitons were hybridized with cavity photons, indicating that the potential energy surfaces of the molecules themselves were altered by the light-matter hybridization. These findings, as further elaborated in Ebbesen's comprehensive review, emphasized that strong coupling introduces a new regime of molecular behavior, bridging quantum optics and chemistry (**Figure 1.15**)[92]. These results challenged the traditional separation of photonics and chemistry by demonstrating that electromagnetic vacuum fields, when strongly coupled to matter, can directly influence chemical reactivity. Subsequent works from the Ebbesen group expanded this concept to vibrational strong coupling in the mid-IR, further proving that even ground-state reaction barriers could be tuned by cavity-mediated hybridization[88]. Together, these pioneering studies laid the groundwork for applying strong coupling not only as a tool of quantum optics but also as a novel paradigm in photochemistry and catalysis.

Inspired by these advances, researchers began exploring whether similar principles could be extended beyond exciton-photon systems to other optical modes. In this context, Misawa and collaborators introduced the concept of modal strong coupling, namely, the coherent hybridization between distinct photonic or plasmonic resonances. A representative case is the coupling between LSPR of metal nanoparticles and the FP nanocavity modes. Unlike exciton-cavity systems, where hybridization occurs between matter excitations and confined photons, modal strong coupling involves two electromagnetic resonances of comparable energy that exchange energy coherently. Misawa's group recognized that such hybridization could drastically reshape the absorption spectrum of plasmonic photoanodes and, more importantly, enhance hot-carrier generation and transfer efficiency in photoelectrochemical reactions (**Figure 1.16**)[78,93].

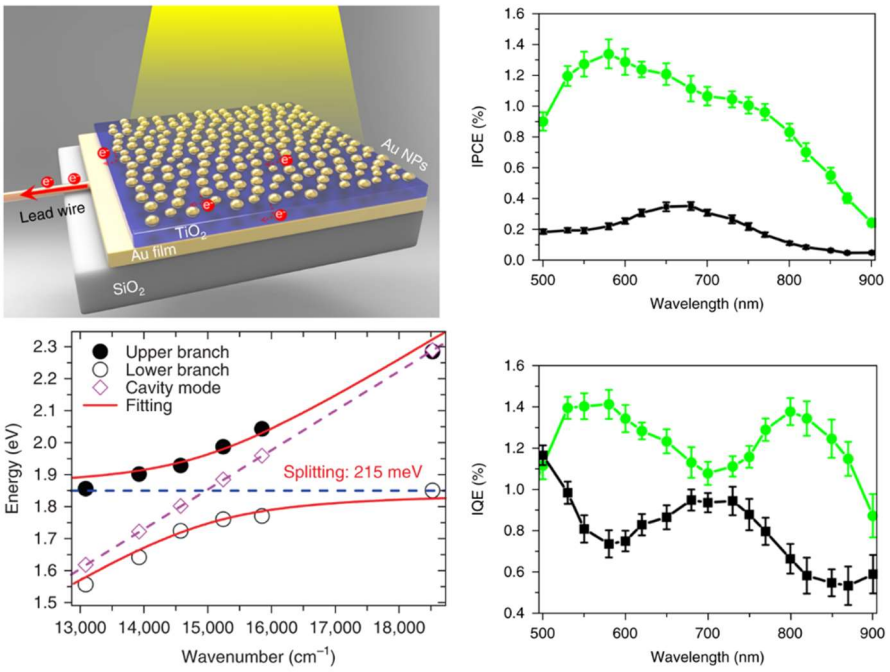

Figure 1.16 Enhancement of water-splitting quantum efficiency under modal strong coupling[78].

Although still in its infancy compared to molecular strong coupling, modal strong coupling has already demonstrated remarkable potential in artificial photosynthesis. Misawa's investigations have addressed fundamental aspects such as the mechanisms in near-field[94], the influence of interfacial dielectric environments[95], the modification

of activation energy barriers[96], and the effect of plasmonic material choice[97]. Moreover, experimental results revealed that the modal strong coupling photoanodes could not only boost photocurrent but also affect product selectivity[98] and interact differently with sacrificial electron donors[99], and even be extended to SERS platforms[100].

Still, these studies highlight only one facet of the potential of modal strong coupling. Nevertheless, the progress already achieved suggests that this strategy represents a promising avenue for overcoming current limitations in artificial photosynthesis, offering new degrees of freedom for manipulating energy transfer, charge separation, and chemical pathways.

1.2 Research motivation and thesis overview

1.2.1 Motivation

In the Misawa laboratory, considerable effort has been directed toward creating artificial photosynthesis systems that function efficiently under visible and NIR illumination, with a particular focus on utilizing modal strong coupling photoanodes. Nevertheless, despite these encouraging achievements, the detailed microscopic mechanisms responsible for such enhancements remain insufficiently clarified. To date, most studies in our group have concentrated on tailoring material architectures and improving device performance, whereas systematic exploration of the fundamental origins of modal strong coupling effects has been relatively scarce.

Motivated by this knowledge gap, I chose to focus my doctoral research on elucidating the mechanistic foundations of modal strong coupling photoanodes. The system developed in our group employs metal nanoparticles to induce LSPR modes, typically prepared through the thermal evaporation of ultrathin metal films followed by annealing. This fabrication route has the advantage of simplicity and minimal damage to underlying semiconductor layers, while also enabling a degree of tunability in particle size and morphology by adjusting film thickness and annealing temperature[101]. Nevertheless, the statistical nature of nanoparticle nucleation results in a broad size distribution and random spatial arrangement. This intrinsic lack of control introduces multiple variables simultaneously, making it challenging to isolate and examine the role

of individual structural parameters in governing strong coupling behavior.

To overcome these limitations, my research adopts a bottom-up, mechanism-driven approach. Specifically, I utilize electron-beam lithography to fabricate well-defined arrays of metallic nanostructures with precisely controlled size, shape, and spatial arrangement. This approach allows systematic tuning of key parameters—such as resonance energy, coupling strength, and mode overlap—with high reproducibility and minimal ambiguity. By incrementally varying one parameter at a time, I aim to deconvolute the contributions of each structural factor to the emergence of modal strong coupling. Through this stepwise methodology, it becomes possible not only to validate theoretical models but also to build an intuitive physical picture of how hybridized polaritonic states contribute to enhanced charge separation and improved reaction quantum yields.

Ultimately, by gaining a mechanistic understanding of modal strong coupling, this research aspires to provide a rational basis for designing next-generation photoanodes with maximized efficiency in solar-to-chemical conversion. Such insights will not only enrich the fundamental field of light-matter interactions but also lay the groundwork for advancing artificial photosynthesis closer to practical implementation.

1.2.2 Overview of thesis

This thesis is devoted to the systematic design, fabrication, and characterization of modal strong coupling systems aimed at advancing artificial photosynthesis. The central objective is to reveal the physical mechanisms by which modal strong coupling governs hot-carrier dynamics, near-field interactions, and ultimately the quantum yield of PEC reactions. To achieve this goal, multiple complementary approaches were employed, including spectral measurements for optical mode analysis, transient absorption spectroscopy for carrier dynamics, photoemission electron microscopy (PEEM) for nanoscale field mapping and dephasing evaluation, and PEC measurements for device-level evaluation. By integrating these techniques, the present study provides a comprehensive understanding of how **quantum coherence** interplay within the modal strong coupling photoanodes.

Chapter 2 presents the fabrication strategy and fundamental optical characterization of modal strong coupling systems consisting of periodic Au nanodisk arrays. Particular attention is paid to controlling the particle number density of the nanodisks, enabling systematic modulation of coupling strength. The experimental results are supported by spectral analysis, from which the Rabi splitting and related coupling parameters are extracted. This chapter establishes the foundational framework for quantifying modal strong coupling in well-defined nanodisks.

Chapter 3 focuses on how the manipulation on particle number density of Au-nanodisks influences hot electron injection and photoinduced charge separation. Through transient absorption spectroscopy, the hot-carrier generation and transfer processes are directly monitored, while PEEM is used to resolve near-field properties and dephasing dynamics at the nanoscale. In parallel, PEC measurements are carried out to link these microscopic processes with macroscopic photon-to-current conversion efficiency. Together, these investigations elucidate the role of quantum coherence in enhancing charge-transfer pathways under modal strong coupling conditions.

Chapter 4 extends the study by introducing mixed nanostructure arrays, where nanotriangles are incorporated into the periodic nanodisks arrays. This structural perturbation provides a means of tuning dephasing properties. By systematically varying the proportion of nanotriangles, a branch-dependent asymmetry in hot electron injection efficiency is observed. This chapter highlights how structural heterogeneity can be deliberately engineered to manipulate the hot carrier dynamics.

Chapter 5 deepens the mechanistic understanding by focusing on the near-field properties and dephasing behavior of the mixed nanostructures. By correlating the near-field distribution, dephasing dynamics, and hot electron injection efficiency, this chapter elucidates how quantum coherence governs hot-carrier transfer processes. The results reveal that quantum coherence play a decisive role in modulating carrier dynamics, thereby contributing to the observed asymmetric, branch-dependent hot electron injection efficiency in the modal strong coupling systems.

Finally, **Chapter 6** provides the overall conclusion of the thesis. It synthesizes the findings from the preceding chapters to establish a coherent picture of how modal

strong coupling and quantum coherence can be harnessed in artificial photosynthesis. In addition, this chapter outlines future research perspectives, emphasizing both fundamental and applied directions.

In summary, the present thesis offers not only a detailed mechanistic insight into modal strong coupling in plasmonic photoanodes, but also provides experimental evidence of the pivotal role of quantum coherence in driving efficiency improvements. By bridging nanoscale optical phenomena with macroscopic PEC functionality, this work lays the groundwork for rationally engineering next-generation artificial photosynthesis systems.

1.3 Reference

1 International Energy, A. Electricity generation mix for selected regions, 2024. (2025).

2 Wang, Q. & Domen, K. Particulate Photocatalysts for Light-Driven Water Splitting: Mechanisms, Challenges, and Design Strategies. *Chemical Reviews* **120**, 919-985, doi:10.1021/acs.chemrev.9b00201 (2020).

3 Thakkar, V., Parmar, H. & Nayak, J. GHG Tank : for Heat Storage and Utilization. *International Journal of Engineering Research And Technology* **3**, 1131-1138 (2014).

4 Fujishima, A. & Honda, K. Electrochemical Photolysis of Water at a Semiconductor Electrode. *Nature* **238**, 37-38, doi:10.1038/238037a0 (1972).

5 O'Regan, B. & Grätzel, M. A low-cost, high-efficiency solar cell based on dye-sensitized colloidal TiO_2 films. *Nature* **353**, 737-740, doi:10.1038/353737a0 (1991).

6 Mehrabi, S., Rezaei, M. H. & Zarifkar, A. Ultra-broadband solar absorber based on multi-layer TiN/TiO_2 structure with near-unity absorption. *Journal of the Optical Society of America B* **36**, 2602-2609, doi:10.1364/JOSAB.36.002602 (2019).

7 Shockley, W. & Queisser, H. J. Detailed Balance Limit of Efficiency of p-n Junction Solar Cells. *Journal of Applied Physics* **32**, 510-519,

doi:10.1063/1.1736034 (1961).

8 Sun, F. in *Synthesis and Device Applications of Graphene Derivatives and Quantum Dots* 1-4, Springer Nature Switzerland (2024).

9 Chen, T. *et al.* Applications of Lithium-Ion Batteries in Grid-Scale Energy Storage Systems. *Transactions of Tianjin University* **26**, 208-217, doi:10.1007/s12209-020-00236-w (2020).

10 Maeda, K. & Domen, K. Photocatalytic Water Splitting: Recent Progress and Future Challenges. *The journal of physical chemistry letters* **1**, 2655-2661, doi:10.1021/jz1007966 (2010).

11 Hill, R. Oxygen Evolved by Isolated Chloroplasts. *Nature* **139**, 881-882, doi:10.1038/139881a0 (1937).

12 Schrauzer, G. N. & Guth, T. D. Photolysis of Water and Photoreduction of Nitrogen on Titanium Dioxide. *Journal of the American Chemical Society* **99**, 7189-7193, doi:10.1021/ja00464a015 (1977).

13 Halmann, M. Photoelectrochemical reduction of aqueous carbon dioxide on p-type gallium phosphide in liquid junction solar cells. *Nature* **275**, 115-116, doi:10.1038/275115a0 (1978).

14 Prier, C. K., Rankic, D. A. & MacMillan, D. W. C. Visible Light Photoredox Catalysis with Transition Metal Complexes: Applications in Organic Synthesis. *Chemical Reviews* **113**, 5322-5363, doi:10.1021/cr300503r (2013).

15 Kärkäs, M. D., Verho, O., Johnston, E. V. & Åkermark, B. Artificial Photosynthesis: Molecular Systems for Catalytic Water Oxidation. *Chemical Reviews* **114**, 11863-12001, doi:10.1021/cr400572f (2014).

16 Klein, M., Pankiewicz, R., Zalas, M. & Stampor, W. Magnetic field effects in dye-sensitized solar cells controlled by different cell architecture. *Scientific Reports* **6**, 30077, doi:10.1038/srep30077 (2016).

17 Asahi, R., Morikawa, T., Ohwaki, T., Aoki, K. & Taga, Y. Visible-Light Photocatalysis in Nitrogen-Doped Titanium Oxides. *Science* **293**, 269-271, doi:10.1126/science.1061051 (2001).

18 Irie, H., Watanabe, Y. & Hashimoto, K. Carbon-doped Anatase TiO_2 Powders

as a Visible-light Sensitive Photocatalyst. *Chemistry Letters* **32**, 772-773, doi:10.1246/cl.2003.772 (2003).

19 Ohno, T., Mitsui, T. & Matsumura, M. Photocatalytic Activity of S-doped TiO_2 Photocatalyst under Visible Light. *Chemistry Letters* **32**, 364-365, doi:10.1246/cl.2003.364 (2003).

20 Chen, X. & Burda, C. The Electronic Origin of the Visible-Light Absorption Properties of C-, N- and S-Doped TiO_2 Nanomaterials. *Journal of the American Chemical Society* **130**, 5018-5019, doi:10.1021/ja711023z (2008).

21 Wang, L., Xu, X., Cheng, Q., Dou, S. X. & Du, Y. Near-Infrared-Driven Photocatalysts: Design, Construction, and Applications. *Small* **17**, 1904107, doi:10.1002/smll.201904107 (2021).

22 Inoue, H. *et al.* The Water Oxidation Bottleneck in Artificial Photosynthesis: How Can We Get Through It? An Alternative Route Involving a Two-Electron Process. *ChemSusChem* **4**, 173-179, doi:10.1002/cssc.201000385 (2011).

23 Tian, L., Guan, X., Zong, S., Dai, A. & Qu, J. Cocatalysts for Photocatalytic Overall Water Splitting: A Mini Review. *Catalysts* **13**, 355, doi:10.3390/catal13020355 (2023).

24 Lv, S., Du, Y., Wu, F., Cai, Y. & Zhou, T. Review on LSPR assisted photocatalysis: effects of physical fields and opportunities in multifield decoupling. *Nanoscale Advances* **4**, 2608-2631, doi:10.1039/D2NA00140C (2022).

25 Luo, J. *Formation of Stöber silica supported gold nanoparticles : mechanism and application Formation de nanoparticules d'or supportées sur silice Stöber : mécanismes et applications*, Université de Strasbourg, (2013).

26 Szunerits, S. & Boukherroub, R. Sensing using localised surface plasmon resonance sensors. *Chemical Communications* **48**, 8999-9010, doi:10.1039/C2CC33266C (2012).

27 Mayer, K. M. & Hafner, J. H. Localized Surface Plasmon Resonance Sensors. *Chemical Reviews* **111**, 3828-3857, doi:10.1021/cr100313v (2011).

28 Suh, J. Y. *et al.* Extraordinary Nonlinear Absorption in 3D Bowtie

Nanoantennas. *Nano Letters* **12**, 269-274, doi:10.1021/nl2034915 (2012).

29 Moskovits, M. Surface-enhanced spectroscopy. *Reviews of Modern Physics* **57**, 783-826, doi:10.1103/RevModPhys.57.783 (1985).

30 Nie, S. & Emory, S. R. Probing Single Molecules and Single Nanoparticles by Surface-Enhanced Raman Scattering. *Science* **275**, 1102-1106, doi:10.1126/science.275.5303.1102 (1997).

31 Osberg, K. D. *et al.* Dispersible Gold Nanorod Dimers with Sub-5 nm Gaps as Local Amplifiers for Surface-Enhanced Raman Scattering. *Nano Letters* **12**, 3828-3832, doi:10.1021/nl301793k (2012).

32 Lin, J.-S. *et al.* Advanced plasmonic technologies for multi-scale biomedical imaging. *Chemical Society Reviews* **51**, 9445-9468, doi:10.1039/D2CS00525E (2022).

33 Raphael, M. P. *et al.* A New Methodology for Quantitative LSPR Biosensing and Imaging. *Analytical Chemistry* **84**, 1367-1373, doi:10.1021/ac2023266 (2012).

34 Zhang, L. *et al.* Development of a Surface Plasmon Resonance and Fluorescence Imaging System for Biochemical Sensing. *Micromachines* **10**, 442, doi:10.3390/mi10070442 (2019).

35 Gomes Silva, C., Juárez, R., Marino, T., Molinari, R. & García, H. Influence of Excitation Wavelength (UV or Visible Light) on the Photocatalytic Activity of Titania Containing Gold Nanoparticles for the Generation of Hydrogen or Oxygen from Water. *Journal of the American Chemical Society* **133**, 595-602, doi:10.1021/ja1086358 (2011).

36 Chen, J.-J., Wu, J. C. S., Wu, P. C. & Tsai, D. P. Improved Photocatalytic Activity of Shell-Isolated Plasmonic Photocatalyst Au@SiO_2/TiO_2 by Promoted LSPR. *The Journal of Physical Chemistry C* **116**, 26535-26542, doi:10.1021/jp309901y (2012).

37 Atwater, H. A. & Polman, A. Plasmonics for improved photovoltaic devices. *Nature Materials* **9**, 205-213, doi:10.1038/nmat2629 (2010).

38 Awazu, K. *et al.* A Plasmonic Photocatalyst Consisting of Silver Nanoparticles

Embedded in Titanium Dioxide. *Journal of the American Chemical Society* **130**, 1676-1680, doi:10.1021/ja076503n (2008).

39 Ueno, K., Oshikiri, T., Shi, X., Zhong, Y. & Misawa, H. Plasmon-induced artificial photosynthesis. *Interface Focus* **5**, 20140082, doi:10.1098/rsfs.2014.0082 (2015).

40 Ingram, D. B. & Linic, S. Water Splitting on Composite Plasmonic-Metal/Semiconductor Photoelectrodes: Evidence for Selective Plasmon-Induced Formation of Charge Carriers near the Semiconductor Surface. *Journal of the American Chemical Society* **133**, 5202-5205, doi:10.1021/ja200086g (2011).

41 Brown, M. D. *et al.* Plasmonic Dye-Sensitized Solar Cells Using Core−Shell Metal−Insulator Nanoparticles. *Nano Letters* **11**, 438-445, doi:10.1021/nl1031106 (2011).

42 Chen, H. *et al.* Computational Modeling of Plasmon-Enhanced Light Absorption in a Multicomponent Dye Sensitized Solar Cell. *The Journal of Physical Chemistry C* **116**, 10215-10221, doi:10.1021/jp301950q (2012).

43 Liu, Z., Hou, W., Pavaskar, P., Aykol, M. & Cronin, S. B. Plasmon Resonant Enhancement of Photocatalytic Water Splitting Under Visible Illumination. *Nano Letters* **11**, 1111-1116, doi:10.1021/nl104005n (2011).

44 Zhang, X., Chen, Y. L., Liu, R. S. & Tsai, D. P. Plasmonic photocatalysis. *Reports on progress in physics. Physical Society (Great Britain)* **76**, 046401, doi:10.1088/0034-4885/76/4/046401 (2013).

45 Katyal, J. & Soni, R. Size- and shape-dependent plasmonic properties of aluminum nanoparticles for nanosensing applications. *Journal of Modern Optics* **60**, doi:10.1080/09500340.2013.856483 (2013).

46 Homola, J. Surface Plasmon Resonance Sensors for Detection of Chemical and Biological Species. *Chemical Reviews* **108**, 462-493, doi:10.1021/cr068107d (2008).

47 Mukherjee, S. *et al.* Hot Electrons Do the Impossible: Plasmon-Induced Dissociation of H_2 on Au. *Nano Letters* **13**, 240-247, doi:10.1021/nl303940z

(2013).

48 Mubeen, S., Hernandez-Sosa, G., Moses, D., Lee, J. & Moskovits, M. Plasmonic Photosensitization of a Wide Band Gap Semiconductor: Converting Plasmons to Charge Carriers. *Nano Letters* **11**, 5548-5552, doi:10.1021/nl203457v (2011).

49 Brongersma, M. L., Halas, N. J. & Nordlander, P. Plasmon-induced hot carrier science and technology. *Nature Nanotechnology* **10**, 25-34, doi:10.1038/nnano.2014.311 (2015).

50 Ermushev, A., McHedlishvili, B., Oleinikov, V. & Petukhov, A. LASER APPLICATIONS AND OTHER TOPICS IN QUANTUM ELECTRONICS: Surface enhancement of local optical fields and the lightning-rod effect. *Quantum Electronics - QUANTUM ELECTRON* **23**, 435-440, doi:10.1070/QE1993v023n05ABEH003090 (1993).

51 Campion, A. & Kambhampati, P. Surface-enhanced Raman scattering. *Chemical Society Reviews* **27**, 241-250, doi:10.1039/A827241Z (1998).

52 Haynes, C. L., McFarland, A. D. & Van Duyne, R. P. Surface-Enhanced Raman Spectroscopy. *Analytical Chemistry* **77**, 338 A-346 A, doi:10.1021/ac053456d (2005).

53 Sharma, B., Frontiera, R. R., Henry, A.-I., Ringe, E. & Van Duyne, R. P. SERS: Materials, applications, and the future. *Materials Today* **15**, 16-25, doi:10.1016/S1369-7021(12)70017-2 (2012).

54 Aroca, R. F., Ross, D. J. & Domingo, C. Surface-Enhanced Infrared Spectroscopy. *Applied Spectroscopy* **58**, 324A-338A, doi:10.1366/0003702042475420 (2004).

55 Osawa, M. *in Near-Field Optics and Surface Plasmon Polaritons* (ed Satoshi Kawata) 163-187, Springer Berlin Heidelberg (2001).

56 Barbillon, G. Latest Advances in Metasurfaces for SERS and SEIRA Sensors as Well as Photocatalysis. *International Journal of Molecular Sciences* **23**, 10592, doi:10.3390/books978-3-0365-8324-2 (2022).

57 Knight, M. W. *et al.* Aluminum for Plasmonics. *ACS Nano* **8**, 834-840,

doi:10.1021/nn405495q (2014).

58 Bansal, A., Sekhon, J. S. & Verma, S. S. Scattering Efficiency and LSPR Tunability of Bimetallic Ag, Au, and Cu Nanoparticles. *Plasmonics* **9**, 143-150, doi:10.1007/s11468-013-9607-x (2014).

59 Katsoukis, G. & Frei, H. Ultrathin oxide layers for nanoscale integration of molecular light absorbers, catalysts, and complete artificial photosystems. *The Journal of chemical physics* **150**, 041501, doi:10.1063/1.5052453 (2019).

60 Li, S., Xu, W., Meng, L., Tian, W. & Li, L. Recent Progress on Semiconductor Heterojunction-Based Photoanodes for Photoelectrochemical Water Splitting. *Small Science* **2**, 2100112, doi:10.1002/smsc.202100112 (2022).

61 Taylor, A. B. & Zijlstra, P. Single-Molecule Plasmon Sensing: Current Status and Future Prospects. *ACS Sensors* **2**, 1103-1122, doi:10.1021/acssensors.7b00382 (2017).

62 Huang, T., Nallathamby, P. D. & Xu, X.-H. N. Photostable Single-Molecule Nanoparticle Optical Biosensors for Real-Time Sensing of Single Cytokine Molecules and Their Binding Reactions. *Journal of the American Chemical Society* **130**, 17095-17105, doi:10.1021/ja8068853 (2008).

63 Haes, A. J. & Van Duyne, R. P. A Nanoscale Optical Biosensor: Sensitivity and Selectivity of an Approach Based on the Localized Surface Plasmon Resonance Spectroscopy of Triangular Silver Nanoparticles. *Journal of the American Chemical Society* **124**, 10596-10604, doi:10.1021/ja020393x (2002).

64 Xie, L. *et al.* State of the art in flexible SERS sensors toward label-free and onsite detection: from design to applications. *Nano Research* **15**, doi:10.1007/s12274-021-4017-4 (2022).

65 O'Neal, D. P., Hirsch, L. R., Halas, N. J., Payne, J. D. & West, J. L. Photo-thermal tumor ablation in mice using near infrared-absorbing nanoparticles. *Cancer letters* **209**, 171-176, doi:10.1016/j.canlet.2004.02.004 (2004).

66 Kong, X. *et al.* Sandwich Layer-Modified Ω-Shaped Fiber-Optic LSPR Enables the Development of an Aptasensor for a Cytosensing–Photothermal Therapy Circuit. *ACS Sensors* **9**, 4637-4645, doi:10.1021/acssensors.4c00841 (2024).

67 Ding, X. *et al.* Surface Plasmon Resonance Enhanced Light Absorption and Photothermal Therapy in the Second Near-Infrared Window. *Journal of the American Chemical Society* **136**, 15684-15693, doi:10.1021/ja508641z (2014).

68 Zhou, L., Huang, Q. & Xia, Y. Plasmon-Induced Hot Electrons in Nanostructured Materials: Generation, Collection, and Application to Photochemistry. *Chemical Reviews* **124**, 8597-8619, doi:10.1021/acs.chemrev.4c00165 (2024).

69 Derkacs, D., Lim, S. H., Matheu, P., Mar, W. & Yu, E. T. Improved performance of amorphous silicon solar cells via scattering from surface plasmon polaritons in nearby metallic nanoparticles. *Applied Physics Letters* **89**, doi:10.1063/1.2336629 (2006).

70 Morfa, A. J., Rowlen, K. L., Reilly, T. H., III, Romero, M. J. & van de Lagemaat, J. Plasmon-enhanced solar energy conversion in organic bulk heterojunction photovoltaics. *Applied Physics Letters* **92**, doi:10.1063/1.2823578 (2008).

71 Tvingstedt, K., Persson, N.-K., Inganäs, O., Rahachou, A. & Zozoulenko, I. V. Surface plasmon increase absorption in polymer photovoltaic cells. *Applied Physics Letters* **91**, doi:10.1063/1.2782910 (2007).

72 Kamat, P. V., Tvrdy, K., Baker, D. R. & Radich, E. J. Beyond Photovoltaics: Semiconductor Nanoarchitectures for Liquid-Junction Solar Cells. *Chemical Reviews* **110**, 6664-6688, doi:10.1021/cr100243p (2010).

73 Ueno, K., Oshikiri, T. & Misawa, H. Plasmon-Induced Water Splitting Using Metallic-Nanoparticle-Loaded Photocatalysts and Photoelectrodes. *ChemPhysChem* **17**, 199-215, doi:10.1002/cphc.201500761 (2016).

74 Ueno, K. & Misawa, H. Plasmon-enhanced photocurrent generation and water oxidation from visible to near-infrared wavelengths. *NPG Asia Materials* **5**, e61-e61, doi:10.1038/am.2013.42 (2013).

75 Oshikiri, T., Ueno, K. & Misawa, H. Plasmon-induced ammonia synthesis through nitrogen photofixation with visible light irradiation. *Angewandte Chemie International edition in English* **53**, 9802-9805, doi:10.1002/anie.201404748 (2014).

76 Nishijima, Y. *et al.* Near-Infrared Plasmon-Assisted Water Oxidation. *The journal of physical chemistry letters* **3**, 1248-1252, doi:10.1021/jz3003316 (2012).

77 Shi, X., Ueno, K., Takabayashi, N. & Misawa, H. Plasmon-Enhanced Photocurrent Generation and Water Oxidation with a Gold Nanoisland-Loaded Titanium Dioxide Photoelectrode. *The Journal of Physical Chemistry C* **117**, 2494-2499, doi:10.1021/jp3064036 (2013).

78 Shi, X. *et al.* Enhanced water splitting under modal strong coupling conditions. *Nature Nanotechnology* **13**, 953-958, doi:10.1038/s41565-018-0208-x (2018).

79 Eftink, M. R. in *Topics in Fluorescence Spectroscopy: Principles* (ed Joseph R. Lakowicz) 53-126, Springer US (2002).

80 Clegg, R. M. in *Laboratory Techniques in Biochemistry and Molecular Biology* Vol. 33, 1-57 Elsevier (2009).

81 Novotny, L. Strong coupling, energy splitting, and level crossings: A classical perspective. *American Journal of Physics* **78**, 1199-1202, doi:10.1119/1.3471177 (2010).

82 Dovzhenko, D. S., Ryabchuk, S. V., Rakovich, Y. P. & Nabiev, I. R. Light–matter interaction in the strong coupling regime: configurations, conditions, and applications. *Nanoscale* **10**, 3589-3605, doi:10.1039/C7NR06917K (2018).

83 Reithmaier, J. P. *et al.* Strong coupling in a single quantum dot–semiconductor microcavity system. *Nature* **432**, 197-200, doi:10.1038/nature02969 (2004).

84 Chikkaraddy, R. *et al.* Single-molecule strong coupling at room temperature in plasmonic nanocavities. *Nature* **535**, 127-130, doi:10.1038/nature17974 (2016).

85 Abdelhamid, M., O'Mullane, A. & Snook, G. ChemInform Abstract: Storing Energy in Plastics: A Review on Conducting Polymers & Their Role in Electrochemical Energy Storage. *RSC Advances* **46**, doi:10.1039/C4RA15947K (2015).

86 Favero, I. & Karrai, K. Optomechanics of deformable optical cavities. *Nature Photonics* **3**, 201-205, doi:10.1038/nphoton.2009.42 (2009).

87 Lotsch, H. K. V. *The Scalar Theory for Optical Resonators and Beam*

Waveguides. I. Development of General Theory. Pergamon Press (1964).

88 Thomas, A. *et al.* Ground-State Chemical Reactivity under Vibrational Coupling to the Vacuum Electromagnetic Field. *Angewandte Chemie International Edition* **55**, 11462-11466, doi:10.1002/anie.201605504 (2016).

89 Hutchison, J. A., Schwartz, T., Genet, C., Devaux, E. & Ebbesen, T. W. Modifying Chemical Landscapes by Coupling to Vacuum Fields. *Angewandte Chemie International Edition* **51**, 1592-1596, doi:10.1002/anie.201107033 (2012).

90 Ebbesen, T. W. Hybrid Light–Matter States in a Molecular and Material Science Perspective. *Accounts of Chemical Research* **49**, 2403-2412, doi:10.1021/acs.accounts.6b00295 (2016).

91 Thomas, A. *et al.* Tilting a ground-state reactivity landscape by vibrational strong coupling. *Science* **363**, 615-619, doi:10.1126/science.aau7742 (2019).

92 Garcia-Vidal, F. J., Ciuti, C. & Ebbesen, T. W. Manipulating matter by strong coupling to vacuum fields. *Science* **373**, eabd0336, doi:10.1126/science.abd0336 (2021).

93 Wang, Y., Shi, X., Oshikiri, T. & Misawa, H. Improved water splitting efficiency of Au-NP-loaded Ga_2O_3 thin films in the visible region under strong coupling conditions. *Nanoscale Advances* **5**, 119-123, doi:10.1039/D2NA00768A (2023).

94 Cao, Y. *et al.* Near-field engineering for boosting the photoelectrochemical activity to a modal strong coupling structure. *Chemical Communications* **57**, 524-527, doi:10.1039/D0CC07335K (2021).

95 Cao, E. *et al.* Improving Charge Transfer under Strong Coupling Conditions via Interfacial Modulation. *ACS Photonics* **11**, 1205-1212, doi:10.1021/acsphotonics.3c01733 (2024).

96 Cao, E. *et al.* Activation Energy in the Electron Transfer Process and Water Oxidation Intermediate Generation under Plasmon–Nanocavity Strong Coupling. *The Journal of Physical Chemistry C* **129**, 1590-1597, doi:10.1021/acs.jpcc.4c07398 (2025).

97 Suganami, Y., Oshikiri, T., Shi, X. & Misawa, H. Water Oxidation under Modal

Ultrastrong Coupling Conditions Using Gold/Silver Alloy Nanoparticles and Fabry–Pérot Nanocavities. *Angewandte Chemie International Edition* **60**, 18438-18442, doi:10.1002/anie.202103445 (2021).

98 Oshikiri, T., Shi, X. & Misawa, H. Enhancement of Selective Fixation of Dinitrogen to Ammonia under Modal Strong Coupling Conditions. *European Journal of Inorganic Chemistry* **2020**, 1396-1401, doi:10.1002/ejic.201901260 (2020).

99 Cao, Y. *et al.* Efficient Hot-Electron Transfer under Modal Strong Coupling Conditions with Sacrificial Electron Donors. *ChemNanoMat* **5**, 1008-1014, doi:10.1002/cnma.201900178 (2019).

100 Zang, X. *et al.* Investigation of Enhanced Water Oxidation under Plasmon–Nanocavity Strong Coupling Using In Situ Electrochemical Surface-Enhanced Raman Spectroscopy. *The Journal of Physical Chemistry C* **127**, 15087-15095, doi:10.1021/acs.jpcc.3c03625 (2023).

101 Gaspar, D. *et al.* Influence of the layer thickness in plasmonic gold nanoparticles produced by thermal evaporation. *Scientific Reports* **3**, 1469, doi:10.1038/srep01469 (2013).

Chapter 2

Fabrication and the optical characterization of the Au-nanodisk array/TiO_2/Au mirror modal strong coupling system

2.1 Introduction

2.1.1 TiO_2 semiconductor and its fabrication

In the context of achieving efficient artificial photosynthesis, the selection of an appropriate semiconductor material for photoelectrodes is of paramount importance. A semiconductor with a sufficiently wide bandgap is required to provide both strong oxidative power and chemical stability under illumination. Among various candidates, Si, InP, and GaSe have been widely explored owing to their favorable band structures and excellent charge transport properties[1-4]. However, these materials suffer from severe photocorrosion when exposed to aqueous electrolytes, which limits their long-term applicability in PEC systems[5]. In contrast, metal oxide semiconductors exhibit excellent chemical robustness and photostability, making them particularly attractive for durable PEC operation[6].

Titanium dioxide (TiO_2) stands out among these oxides as one of the most versatile and widely studied photocatalytic materials. It combines high photoactivity, low cost, environmental benignity, and exceptional long-term stability under a wide range of operating conditions. TiO_2 exists in three primary crystalline polymorphs—rutile, anatase, and brookite—each exhibiting distinct optical and electronic characteristics (**Figure 2.1**)[7-12]. Among them, rutile is the most thermodynamically stable phase, especially for large TiO_2 particles. Its (110) and (100) crystallographic facets possess relatively low surface energy and high thermal stability, making rutile TiO_2 a suitable choice for high-temperature and large-scale applications[13]. In contrast, the anatase phase generally exhibits superior photocatalytic activity compared to rutile, primarily due to its wider bandgap (~3.2 eV), higher surface area, and more favorable charge transport properties. The low-energy (101) surface, which dominates in anatase nanocrystals, offers high electron mobility and reduced surface recombination, while

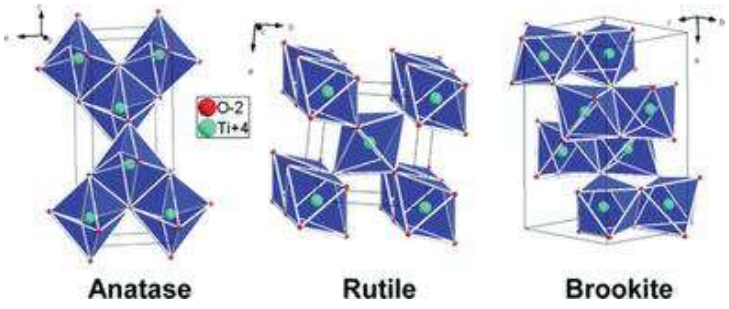

Figure 2.1 Crystal structures of TiO_2 in the anatase, rutile, and brookite phases[7].

the (001) surface possesses strong oxidation potential, facilitating efficient hole-driven redox reactions[14]. Moreover, anatase TiO_2 exhibits a longer carrier lifetime and higher conduction band edge relative to rutile, enabling more efficient charge separation and stronger driving force for reduction reactions—key attributes for photoanode design in water splitting[15]. Although brookite has historically been less investigated due to synthesis challenges and structural complexity, recent studies have revealed its promising photocatalytic properties and unique band alignment, sparking renewed interest in its potential PEC applications[16,17].

The fabrication method of TiO_2 plays a crucial role in determining its morphology, crystallinity, and interfacial quality—all of which directly influence its PEC performance. For bulk or powdered TiO_2, techniques such as solid-state reactions[18], sol-gel synthesis[19,20], and various hydrothermal or solvothermal processes[21,22] are commonly used. These approaches offer versatility in controlling crystal phase and particle size but provide limited control over film thickness and surface uniformity. For thin-film applications, methods including sputtering, chemical vapor deposition (CVD)[23], sol-gel spin coating[24], pulsed laser deposition (PLD)[25], and atomic layer deposition (ALD)[26] have been developed. Among these, ALD has emerged as one of the most powerful and precise methods for preparing high-quality TiO_2 thin films. ALD operates through sequential, self-limiting surface reactions between gaseous precursors—typically titanium tetrachloride ($TiCl_4$) or titanium isopropoxide (TTIP)—and oxidants such as H_2O or O_3[27]. Each reaction cycle deposits a sub-monolayer of material, enabling atomic-scale control over film thickness, stoichiometry, and

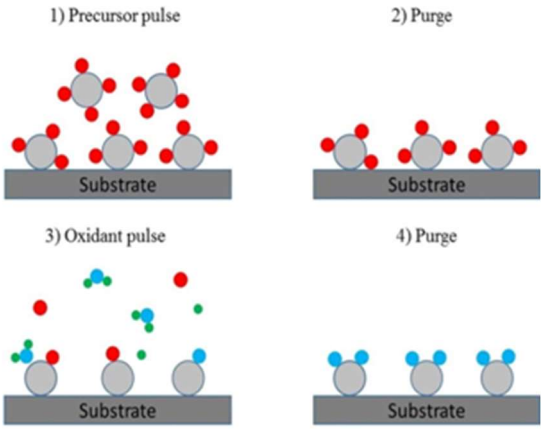

Figure 2.2 Schematic illustration of the ALD processes[28].

uniformity (**Figure 2.2**)[28]. This layer-by-layer process produces films with exceptional conformality, even on substrates with complex geometries or high aspect ratios[29,30]. The resulting TiO_2 films exhibit excellent optical transparency, smooth surface morphology, and highly controlled thickness, all of which are crucial for optical interference management in nanophotonic architectures[31,32]. Furthermore, the crystallinity of ALD-grown TiO_2 can be tailored through deposition temperature: amorphous or partially crystalline anatase films are typically obtained at 150–300 °C, and post-deposition annealing can transform them into fully crystalline anatase without compromising interfacial quality.

These advantages make ALD-grown TiO_2 particularly suitable for plasmonic-photonic hybrid systems, where the semiconductor layer not only serves as a charge transport medium but also as a part of the optical cavity that supports resonant coupling phenomena. The ability to precisely tune film thickness and uniformity enables fine control over the optical path length, FP resonance condition, and modal overlap between LSPRs and cavity modes. Consequently, ALD TiO_2 plays a key role in establishing well-defined and reproducible modal strong coupling systems, serving as the dielectric foundation for studying light-matter interactions and their impact on PEC processes.

2.1.2 Fabrication of Au nanostructures

On the other hand, noble metal nanoparticles or nanostructures are indispensable

components for inducing LSPR and thereby harnessing visible-to-NIR light in artificial photosynthesis systems. Among various plasmonic materials, Au, Ag, and Cu are the most extensively utilized due to their high free-electron density and well-defined plasmonic response in the visible spectral region. Ag exhibits the strongest LSPR intensity and the sharpest resonance linewidth because of its low intrinsic damping[33]; however, its chemical instability and susceptibility to oxidation under ambient or aqueous conditions limit its use in long-term PEC operation[34]. Cu, though more earth-abundant and cost-effective, suffers from rapid oxidation and weak plasmonic performance due to its interband transitions overlapping with the visible range[35,36]. In contrast, Au offers an ideal balance between plasmonic performance and chemical durability—it maintains strong LSPR activity while exhibiting exceptional stability against photocorrosion and oxidation[37,38], making it the most reliable choice for integration with metal oxide semiconductors such as TiO_2.

The fabrication of plasmonic metal nanostructures has been achieved through a wide range of techniques, each offering different levels of structural control, scalability, and precision. Common approaches include colloidal synthesis[39,40], thermal dewetting[41,42], nanosphere lithography (NSL)[43], and electron-beam lithography (EBL)[44].

Colloidal synthesis provides a facile and scalable means to produce metal nanoparticles dispersed in solution, typically by chemical reduction of metal precursors using reducing agents such as sodium citrate or ascorbic acid. The particle size and morphology can be tuned to some extent by varying the precursor concentration, temperature, and capping agents[45]; however, even under optimized conditions, size dispersion is inevitable, leading to inhomogeneous LSPR linewidths. Thermal dewetting of thin metal films represents another simple route for forming nanoparticles directly on solid substrates. Upon annealing at elevated temperatures, a continuous metal film breaks up into discrete islands through surface diffusion and minimization of interfacial energy[46]. While this technique enables direct nanoparticle formation on desired substrates without chemical contamination, the particle size distribution typically follows a Gaussian profile, and the spatial arrangement is random. As a result, it is difficult to achieve precise control over LSPR coupling or periodicity, which are

critical parameters for optical mode engineering and modal strong coupling studies.

To overcome these limitations, lithographic techniques such as NSL and EBL are employed when highly ordered, reproducible, and well-defined nanostructures are required.

Nanosphere lithography (NSL) uses a self-assembled monolayer of polystyrene or silica nanospheres as a physical mask during metal deposition. After deposition, removal of the spheres leaves behind arrays of nanodisks, nanoholes, or other shapes depending on the geometry of the mask. This approach is particularly attractive due to its simplicity and scalability over large areas[47]. However, the achievable geometries are restricted by the packing symmetry and size of the nanospheres, making it difficult to precisely tune parameters such as thickness or interparticle spacing. Electron-beam lithography (EBL), in contrast, offers ultimate precision in fabricating plasmonic nanostructures. It allows the direct writing of nanoscale patterns with programmable geometries—including nanodisks, nanorods, nanoblocks, and nanotriangles—on a resist-coated substrate. The shape, size, and periodicity of the nanostructures can be independently and precisely controlled, enabling systematic investigations of LSPR wavelength dependence and near-field coupling effects[48,49]. Additionally, the thickness of the nanostructures can be increased by coating a thicker photoresist or depositing additional metal layers. Although EBL is relatively time-consuming and may induce slight substrate charging or radiation damage, its flexibility and reproducibility make it the preferred choice for constructing well-defined model systems in optical and PEC research.

The EBL fabrication process typically consists of several critical steps to ensure high structural fidelity and interfacial cleanliness. The substrate—commonly quartz, SiO_2/Si, or TiO_2-coated wafers—must first be thoroughly cleaned using sequential ultrasonic baths in acetone, isopropanol, and deionized water, followed by plasma treatment to enhance surface hydrophilicity and photoresist adhesion. A thin layer of photoresist is then spin-coated onto the substrate and baked to remove residual solvents and solidify the film. The substrate is subsequently loaded into the EBL system, where a focused electron beam scans across the surface according to a predefined pattern. Depending on

the type of resist, the exposure behavior differs. In positive resists, the electron-exposed regions undergo chain scission and become soluble in the developer, whereas in negative resists, the irradiated regions undergo cross-linking and remain after development[50]. After exposure, the substrate is immersed in a suitable developer solution to remove either the exposed or unexposed regions, revealing a nanoscale template pattern.

Following pattern development, metal deposition is performed using thermal evaporation, electron-beam evaporation, or sputtering. Gold is most commonly deposited due to its inertness and well-established adhesion behavior on oxide substrates (often improved by a thin Ti or Cr adhesion layer). Finally, the lift-off process is conducted by immersing the substrate in a solvent which dissolves the remaining resist and removes unwanted metal, leaving behind the well-defined nanostructures. The resulting EBL-fabricated nanostructures exhibit high reproducibility and well-controlled geometrical parameters, allowing systematic tuning of the LSPR wavelength, field confinement, and modal strong coupling behavior. Such precise nanostructures are essential not only for studying LSPR-semiconductor charge transfer dynamics but also for exploring modal strong coupling phenomena in hybrid photonic-plasmonic systems, as will be described in the following sections.

As a preliminary and systematic investigation of the modal strong coupling mechanism, I designed the simplest possible nanostructure—the Au-nanodisks (Au-NDs) array—as the model system. The Au-NDs structure possesses the highest degree of geometric symmetry, which minimizes extraneous variables and allows clear control of the coupling parameters simply by tuning the disk diameter and array periodicity. Furthermore, to reduce unnecessary variations arising from anisotropic near-field interactions, Au-NDs were arranged in a hexagonal lattice rather than a square lattice. In a hexagonal configuration, each Au-ND maintains an equal distance from all nearest neighbors, thereby suppressing discrepancies between diagonal and adjacent coupling modes. This design ensures a more uniform and interpretable optical response, making it ideal for identifying the fundamental characteristics of modal strong coupling.

2.2 Experimental details

2.2.1 Sample fabrication

Silica quartz glass (SiO_2) substrates with dimensions of 10 × 10 × 1.0 mm^3 were employed as the supporting base for constructing the modal strong coupling systems. Prior to any deposition process, the substrates were pre-cleaned to remove surface contaminants and dust particles. The cleaning procedure began with manually wiping the substrate surface using cleanroom-grade wipers (BEMCOT) moistened with acetone to eliminate large particulates. The substrates were subsequently sonicated for 5 minutes each in acetone, methanol, and ultrapure water baths to remove organic residues, followed by drying with a high-purity nitrogen gas stream.

To form the reflective base layer, a 2-nm titanium (Ti) adhesion layer, a ~100-nm Au film, and an additional 2-nm Ti adhesion layer were sequentially deposited onto the cleaned substrates using Helicon sputtering (MPS-4000C1/HC1). This Ti/Au/Ti multilayer served as the bottom Au mirror, essential for forming the FP nanocavity and supporting the modal strong coupling with the upper nanostructures. Subsequently, a TiO_2 thin film of controlled thickness was deposited on the Au-mirror substrates using a commercial ALD reactor (PICOSUN R-200 Advanced) operated at 300 °C. During the ALD process, $TiCl_4$ and deionized water were alternately pulsed as precursors. Each ALD cycle consisted of a $TiCl_4$ pulse, a nitrogen purge, an H_2O pulse, and another purge, enabling precise layer-by-layer growth. The TiO_2 film thickness was accurately tuned by adjusting the total number of deposition cycles. ALD-grown TiO_2 films fabricated under these conditions typically exhibit smooth morphology, high optical transparency, and crystalline anatase structure due to the elevated deposition temperature.

Before proceeding to EBL, the TiO_2 surface was treated using ozone plasma exposure under UV irradiation for 10 minutes to enhance its surface hydrophilicity and resist adhesion. A diluted copolymer electron-beam resist (ZEP-520A, Zeon Chemicals; diluted in anisole at a 1:1 ratio) was then spin-coated on the TiO_2 surface at 1000 rpm for 10 s and 4000 rpm for 60 s to obtain a uniform resist layer of approximately 130 nm thickness. The coated samples were baked on a hot plate at 180 °C for 2 minutes to

remove residual solvents and solidify the resist film. Nanostructure patterning was conducted using an electron-beam lithography system (ELS-F130, Elionix) operating at 130 kV acceleration voltage with a beam current of 300 pA. Pre-designed patterns created in CAD format were used to define periodic circular regions corresponding to the Au-NDs. During EBL exposure, the polymer chains of the positive-type ZEP resist were decomposed at the irradiated regions, enabling selective removal in the subsequent development process. The exposed samples were developed in ZED-N50 developer for 1 minute, and then dried by a high-purity nitrogen gas stream.

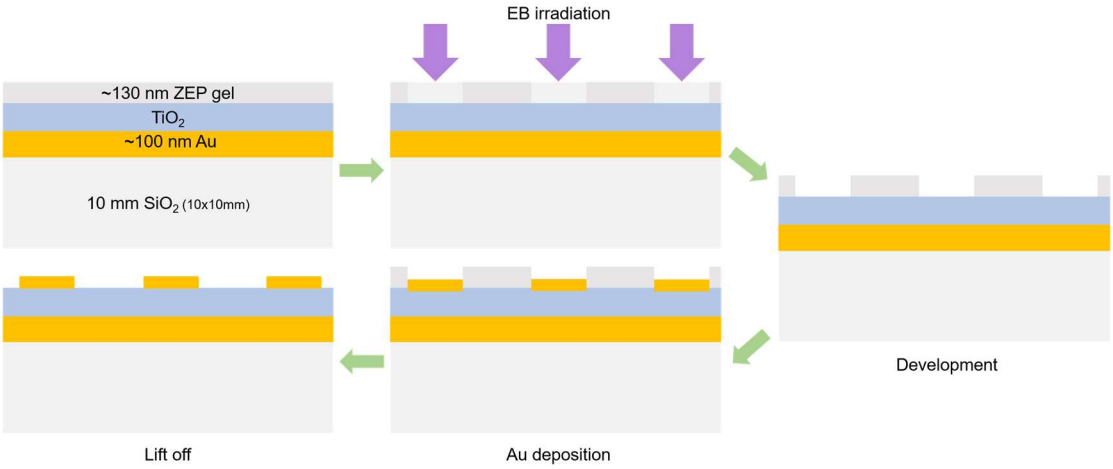

Figure 2.3 Schematic illustration of the EBL processes.

Following development, a 2-nm Ti adhesion layer and a 30-nm Au layer were sequentially deposited by helicon sputtering to form the nanostructures. The lift-off process was then carried out by immersing the samples in dimethylacetamide (DMAC) at 80 °C under ultrasonication twice to dissolve the remaining photoresist and remove the excess metal layers. Subsequently, the samples were further cleaned by sequential ultrasonication in acetone and ultrapure water to ensure complete removal of organic residues and achieve a pristine nanostructured surface. After lift-off, periodic Au-NDs were obtained, uniformly distributed on the TiO_2 surface. The overall process of EBL is schematically illustrated in **Figure 2.3**. For comparison, conventional LSPR structures without strong coupling were also fabricated following the same procedure, except that the bottom Au mirror was omitted. In this case, only a Ti adhesion layer was

deposited directly on the substrate before TiO_2 growth. This difference allowed a direct comparison between uncoupled LSPR systems and the modal strong coupling systems under identical structural and measurement conditions. Hereafter, the modal strong coupling structure composed of the Au-NDs array, TiO_2 layer, and Au bottom mirror is referred to as **ATA**, while the uncoupled LSPR structure consisting of only the Au-NDs array and TiO_2 layer is referred to as **AT**.

2.2.2 Optical properties and morphology characterization

The optical properties of the fabricated structures were characterized using a photonic multichannel analyzer (PMA C7473, Hamamatsu Photonics), which operates over a wavelength range of 400-955 nm. This instrument enabled high-resolution spectral acquisition of both transmittance and reflectance spectra. For the AT structures, the transmittance (T) spectra were recorded by taking the bare substrate region without nanostructures as a reference, while the reflectance (R) spectra were obtained using a silver mirror as the reference standard. In contrast, for ATA—where an opaque Au mirror was incorporated beneath the TiO_2 film—only the reflectance spectra were measured, since light transmission through the substrate is completely suppressed by the metal layer.

Based on these measurements, the absorption (A) spectra were calculated using the standard relations:

For AT: $A = 1 - T - R$

For ATA: $A = 1 - R$ (due to zero transmittance).

Similarly, the extinction (E) spectra were derived as:

$E = -\log_{10}(T)$ for AT, and

$E = -\log_{10}(R)$ for ATA.

These spectral analyses provide crucial insights into the light-matter interaction mechanisms, including the resonance behavior, coupling strength, and potential spectral splitting arising from hybridized modes between LSPR and FP cavity.

The surface morphology and structural details of the samples were characterized using a field-emission scanning electron microscope (FE-SEM, SU8230, Hitachi). For the AT

samples, a conductive E-spacer coating was applied prior to measurement to suppress surface charge accumulation and ensure image clarity, since their surfaces are relatively insulating. In contrast, ATA—owing to the presence of a thick TiO_2 film and the underlying Au mirror—exhibited sufficient intrinsic conductivity, eliminating the need for additional coating.

SEM images were acquired at an accelerating voltage of 5 kV, under multiple fields of view (FOVs) to ensure statistical accuracy. Each image was captured with an exposure time of approximately 20 seconds. For detailed structural observation, the sample stage was tilted at appropriate angles to obtain both oblique top-view and cross-sectional images. The obtained micrographs were subsequently analyzed using the SEM accessory software to quantitatively evaluate parameters such as the nanostructure diameter, interparticle gap, periodicity, and TiO_2 film thickness. These morphological analyses were critical for correlating structural precision with optical response, particularly in evaluating how variations in geometry influence plasmonic and cavity coupling behavior.

2.2.3 Numerical simulations

Numerical simulations based on the finite-difference time-domain (FDTD) method (Lumerical, Inc.) were performed to analyze the optical properties of the fabricated structures and to provide direct comparison with experimental results. The simulated geometries were constructed according to the experimentally designed parameters, where only a single unit cell was modeled under periodic boundary conditions to represent the extended nanostructure array. In the simulation, TiO_2 was modeled as a dielectric medium with a constant refractive index of $n = 2.4$, consistent with the experimentally deposited anatase-like TiO_2 thin film. The optical constants of Au were taken from the widely used dataset of Johnson and Christy, ensuring accurate representation of the metal's dispersion behavior across the visible to NIR region. The system was excited by a normally incident plane wave, with controllable polarization. Since the designed Au-NDs arrays possess a high degree of rotational symmetry, circularly polarized light was employed in most simulations to effectively reproduce

the optical response obtained experimentally under unpolarized illumination using the PMA system. The computational grid employed a uniform mesh size of 1 nm in all three spatial dimensions, providing a balance between numerical accuracy and computational efficiency. Power monitors were placed above and below the structure to calculate reflectance (R) and transmittance (T), from which absorption spectra were obtained. In the case of ATA, where the bottom Au mirror blocks transmission, only reflectance was computed, and the absorption was calculated following the same equations as those in the PMA section.

Additionally, wavelength-resolved near-field enhancement spectra were calculated by extracting the local electric-field intensity (|E|) at representative probe positions (and, where appropriate, summed up over defined surface regions) as a function of wavelength. These near-field spectra provide a direct measure of the spectral positions and relative magnitudes of localized field enhancement associated with both the LSPR and FP modes. By correlating the calculated near-field enhancement peaks with the experimental far-field reflectance/absorption spectra, we were able to assign spectral features to specific resonant modes and quantitatively evaluate modal hybridization and coupling strength. Moreover, the wavelength-dependent enhancement factors derived from these spectra were used to estimate the optical field concentration relevant to hot-carrier generation, thereby enabling a direct comparison between optical enhancement and measured hot-electron injection efficiencies

2.3 Results and discussions

2.3.1 Surface morphology of the Au-NDs

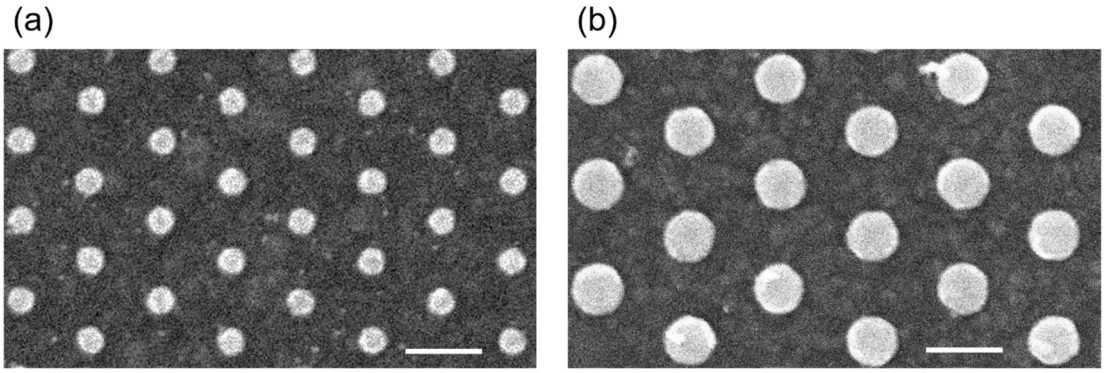

Figure 2.4 SEM images of (a) Au-NDs with diameter of 80 nm and period of 280 nm, and (b) Au-NDs with diameter of 130 nm and period of 260 nm. Scale bars represent 200 nm.

A series of Au-NDs arrays were fabricated for the AT structures to investigate the influence of geometrical parameters on their LSPR characteristics. The designed diameters of the Au-NDs ranged from 60 to 130 nm, while the interparticle gap was varied from 1 to 3 times the corresponding disk diameter to systematically tune the interparticle interaction between adjacent Au-NDs. **Figure 2.4** presents representative SEM images of several AT samples with different Au-ND geometries. The fabricated structures exhibit well-defined disk shapes with smooth edges and uniform periodicity, closely matching the designed parameters. The consistency in size, period, and morphology demonstrates the high fidelity and reproducibility of the nanofabrication process, confirming the successful realization of the intended Au-ND arrays.

2.3.2 Optical properties of AT

Figure 2.5 and **Figure 2.6** presents the extinction spectra of AT structures consisting of Au-NDs with systematically varied geometrical parameters. In the first series, the period-to-diameter ratio was fixed while the disk diameter was altered from 70 to 130 nm (**Figure 2.5**). As shown in the spectra, each AT structure exhibits a distinct LSPR peak, which gradually shifts toward longer wavelengths as the Au-ND diameter increases. This tendency is consistent with the well-established size dependence of LSPR: smaller metallic nanoparticles exhibit stronger spatial confinement of free

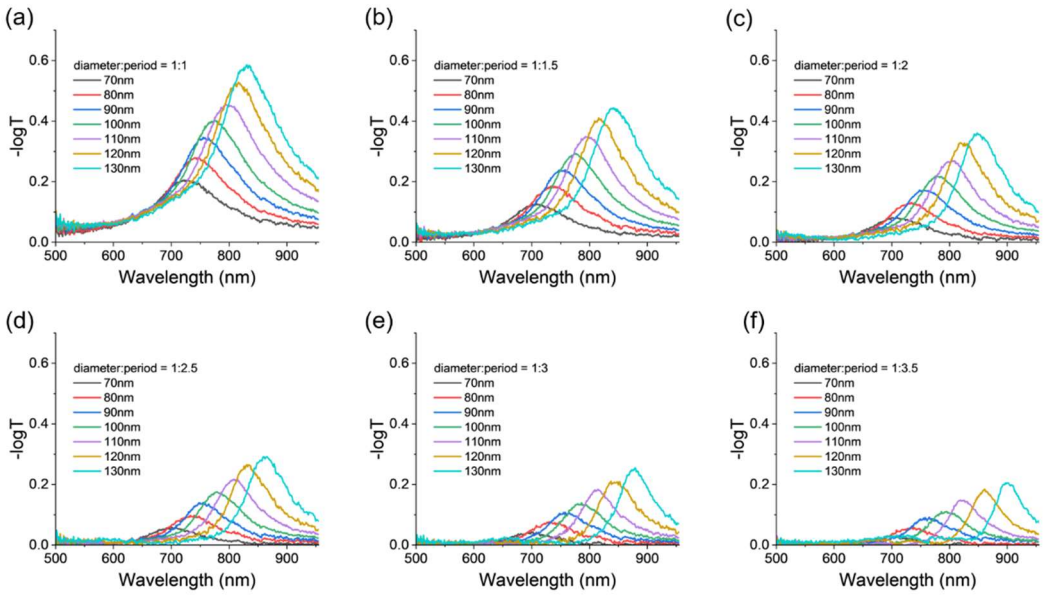

Figure 2.5 Extinction spectra of Au-NDs arrays in the AT structure, measured for various diameters under different diameter-to-period ratios: (a) 1:1, (b) 1:1.5, (c) 1:2, (d) 1:2.5, (e) 1:3, and (f) 1:3.5.

electrons, resulting in a higher resonance energy (shorter wavelength). Such behavior agrees with classical electrodynamic theory and previous reports on size-dependent plasmonic resonance in Au nanostructures.

On the other hand, when analyzing the spectra by keeping the disk diameter constant while tuning the array period, the corresponding extinction spectra, shown in **Figure 2.6**, reveal that the period dependence of the LSPR wavelength is not universal but instead depends strongly on the size of the Au-NDs. To quantitatively summarize these observations, the extracted LSPR wavelengths were plotted as a function of both Au-NDs diameter and array period, as shown in Figure 2.7. Interestingly, for larger Au-NDs (diameter > 80 nm), the LSPR wavelength exhibits a negative correlation with the array period, while for smaller Au-NDs (diameter < 80 nm), a positive correlation is observed. This contrasting behavior can be attributed to the interplay between far-field scattering and near-field coupling effects within the Au-NDs arrays. In large Au-NDs, scattering is dominant and can strongly interact with diffractive modes of the periodic array. As the array period increases, the Rayleigh anomaly shifts toward longer wavelengths, leading to the emergence of lattice plasmon resonances and a

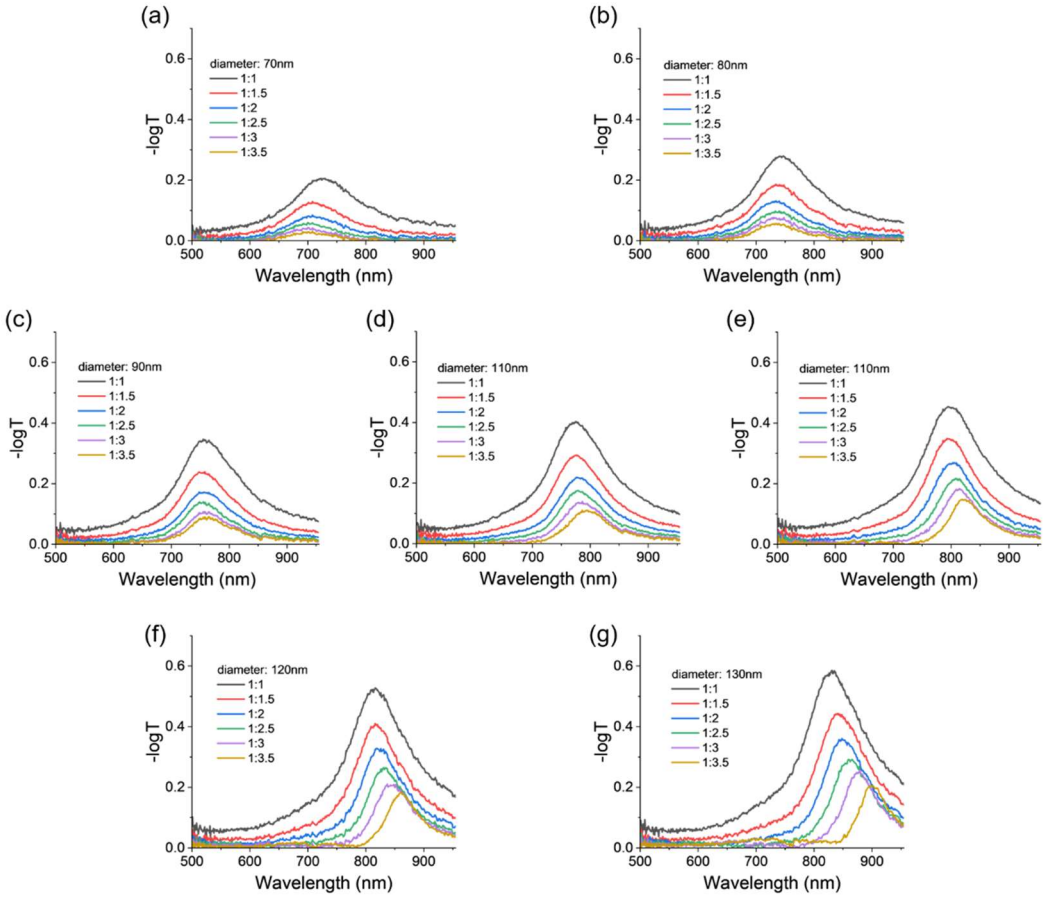

Figure 2.6 Extinction spectra of Au-NDs arrays in the AT structure, measured for various diameter-to-period ratios under diameters: (a) 70 nm, (b) 80 nm, (c) 90 nm, (d) 100 nm, (e) 110 nm, (f) 120nm, and (g) 130 nm.

corresponding redshift of the LSPR peak[51-53]. In contrast, smaller Au-NDs exhibit much weaker scattering and are primarily absorption-dominated. In this regime, the plasmonic resonance is mainly determined by near-field dipole-dipole interactions between adjacent Au-NDs. Reducing the interparticle distance enhances the near-field coupling, which leads to a higher restoring force for the collective electron oscillation and thus a blue shift of the LSPR wavelength[54-56].

Notably, when the Au-NDs diameter is around 80 nm, the LSPR wavelength becomes nearly insensitive to the variation in array period. This indicates a balance between the opposing effects of far-field scattering (favoring a redshift) and near-field coupling (favoring a blueshift). This equilibrium condition is of particular importance for further structural design, as it allows the array period to be adjusted for cavity matching or fabrication convenience without perturbing the intrinsic LSPR energy. Owing to this

unique property, the Au-ND arrays with a diameter of 80 nm were selected as the standard configuration for the subsequent construction of the ATA structures, which are employed to investigate the modal strong coupling behavior between the LSPR and FP nanocavity modes.

2.3.3 Optical properties of FP nanocavity

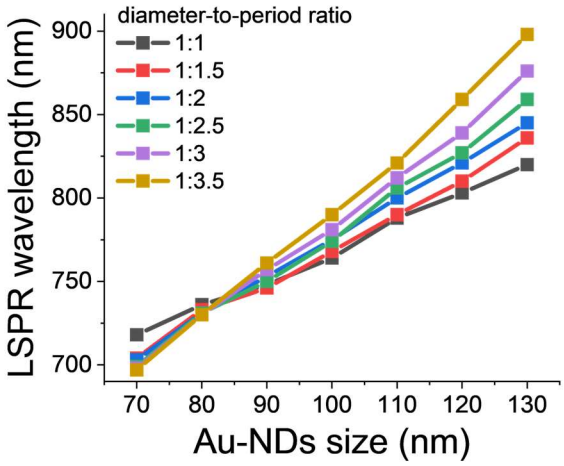

Figure 2.7 Dependence of the LSPR wavelength on the Au-NDs size and the diameter-to-period ratio in the AT structure.

Another key optical component in the ATA modal strong coupling system is the FP nanocavity, whose resonant characteristics must be carefully investigated to enable efficient coupling with the LSPR mode. The FP resonance arises from the constructive interference of multiple reflections within the dielectric cavity layer sandwiched between two metallic mirrors. The resonance wavelengths of such cavity modes are highly sensitive to the optical cavity length and can be described by the classical resonance condition:

$$\lambda_{cavity} = \frac{2nL}{m}$$

where λ_{cavity} is the resonance wavelength of the FP nanocavity, n is the refractive index of the dielectric medium, L is the effective cavity thickness, and m is the integer order of the resonant mode[57]. This equation implies that the resonance energy

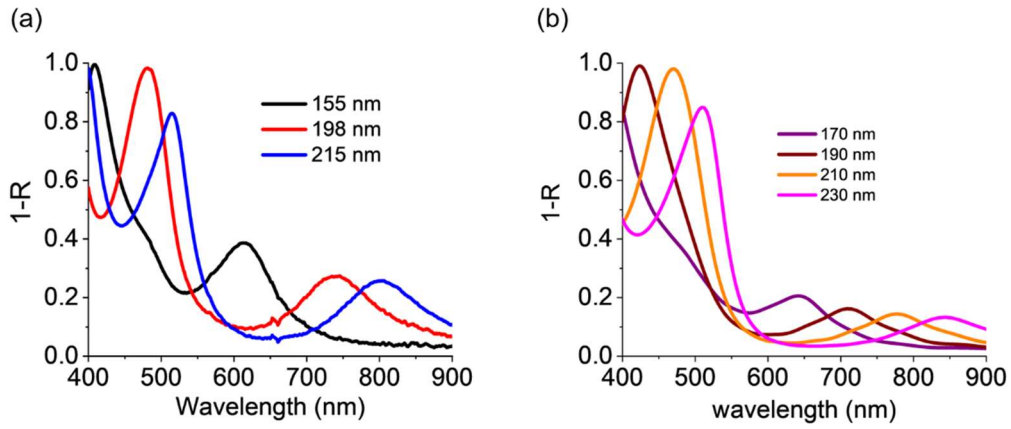

Figure 2.8 (a) Experimental and (b) simulated spectra of FP nanocavities with varying TiO_2 layer thicknesses.

(or wavelength) can be systematically tuned by adjusting the TiO_2 layer thickness, allowing direct control over the spectral position of the cavity mode.

Figure 2.8(a) displays the experimental reflectance spectra of FP nanocavities with various TiO_2 thicknesses. As expected, the resonance peaks redshift progressively as the cavity thickness increases, confirming the dependence predicted by the above relation. To further validate these results, FDTD simulations were carried out using identical geometrical parameters, and the simulated spectra are shown in **Figure 2.8**(b). The simulated resonances exhibit excellent agreement with the experimental data, both in terms of spectral position and overall trend, indicating that the fabricated cavities possess well-controlled thickness and uniform optical quality. To achieve modal strong coupling between the LSPR and the FP nanocavity modes, the resonance energies of the two optical components must be spectrally matched. Based on the LSPR wavelength of the 80-nm Au-NDs identified in the previous section, an FP nanocavity with a thickness of approximately 198 nm was selected, where the cavity resonance coincides with the LSPR mode. This configuration provides the optimal condition for hybridization between the plasmonic and photonic modes, leading to the emergence of distinct upper and lower branches in the ATA structure, as will be discussed in the following section.

2.3.4 Optical properties of ATA

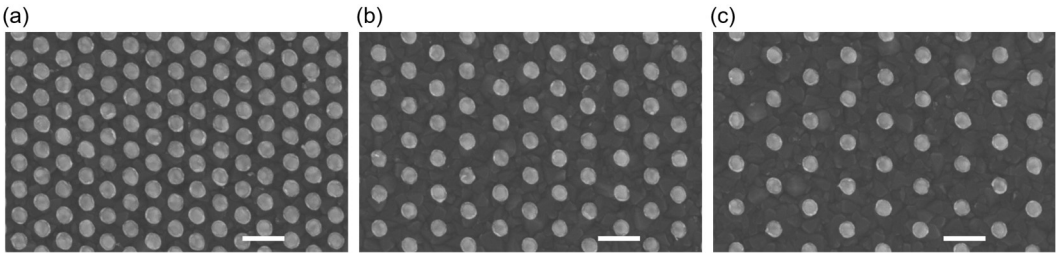

Figure 2.9 SEM images of ATA structures with PNDs of (a) 80, (b) 59, and (c) 29. Scale bars represent 200 nm.

Using the 80-nm Au-NDs and the 198-nm TiO_2 FP nanocavity described above, a series of ATA structures with varying structural periods were fabricated to systematically investigate the dependence of modal strong coupling on Au-NDs density. To quantitatively describe the density of Au-NDs, we introduce the particle number density (PND), defined as the number of Au-NDs per unit area (1 μm^2). Since the Au-NDs diameter was fixed at 80 nm, increasing the structural period (i.e., enlarging the interparticle distance) results in a decrease in PND, as the SEM images in **Figure 2.9**. **Figure 2.10**(a) presents the absorption spectra of ATA structures with different PND values. In all spectra, two distinct resonance peaks corresponding to the upper and lower branches can be clearly observed, and the degree of energy splitting varies systematically with PND. These energy splittings are attributed to the formation of hybrid states resulting from the modal strong coupling between the LSPR of the Au-NDs and the FP nanocavity mode. In addition, the corresponding near-field spectra were obtained through FDTD simulations, as shown in **Figure 2.10**(b). The simulated near-field spectra also exhibit pronounced energy splitting, consistent with the experimental observations. Notably, the near-field intensities at the upper branch are relatively weaker than those at the lower branch, which can be attributed to absorption losses in the Ti adhesion layer, leading to asymmetric field confinement within the cavity.

To quantitatively analyze the coupling behavior, the integrated areas of the split peaks in both the absorption and near-field spectra were evaluated, as summarized in **Figures**

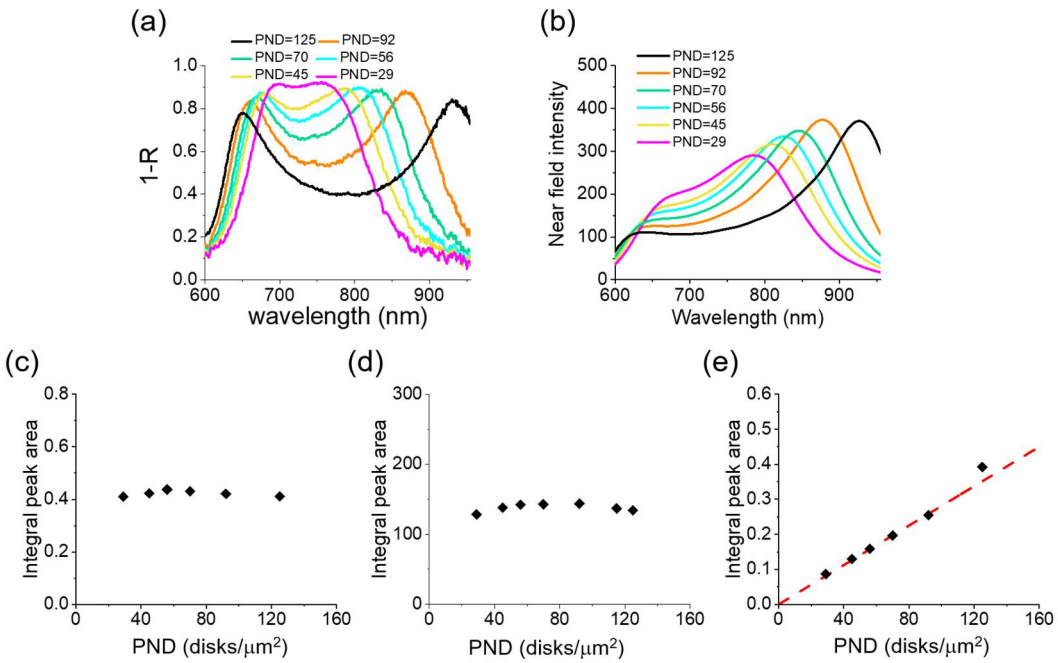

Figure 2.10 (a) Experimental absorption and (b) simulated near-field spectra of ATA structures with varying PNDs. Integrated peak areas of (c) absorption and (d) near-field spectra for ATA, and (e) integrated peak area of absorption for AT.

2.10(c) and (d). Interestingly, both the total absorption and near-field intensities of ATA structures exhibit a saturation behavior, becoming nearly constant when PND increases. In contrast, the AT structures without the FP nanocavity show a monotonically increasing absorption intensity proportional to PND (**Figure 2.10**(e)), following the Lambert-Beer law[58]. This difference indicates that a unique interaction occurs exclusively within the modal strong coupling ATA structures.

Next, to confirm that the observed spectral features indeed arise from the modal strong coupling regime, the energy splittings were quantitatively analyzed. To extract the splitting energy, ATA samples with various PND values were fabricated on FP nanocavities with a range of thicknesses. By plotting the resonance energies of the upper and lower branches as a function of the FP nanocavity resonance wavenumber, dispersion relations were obtained for each PND (**Figure 2.11**). The dispersion curves exhibit the characteristic anticrossing behavior, where the two uncoupled modes (LSPR and FP) repel each other near the tuning point, confirming the presence of mode hybridization. The degree of this anticrossing is directly related to the coupling strength

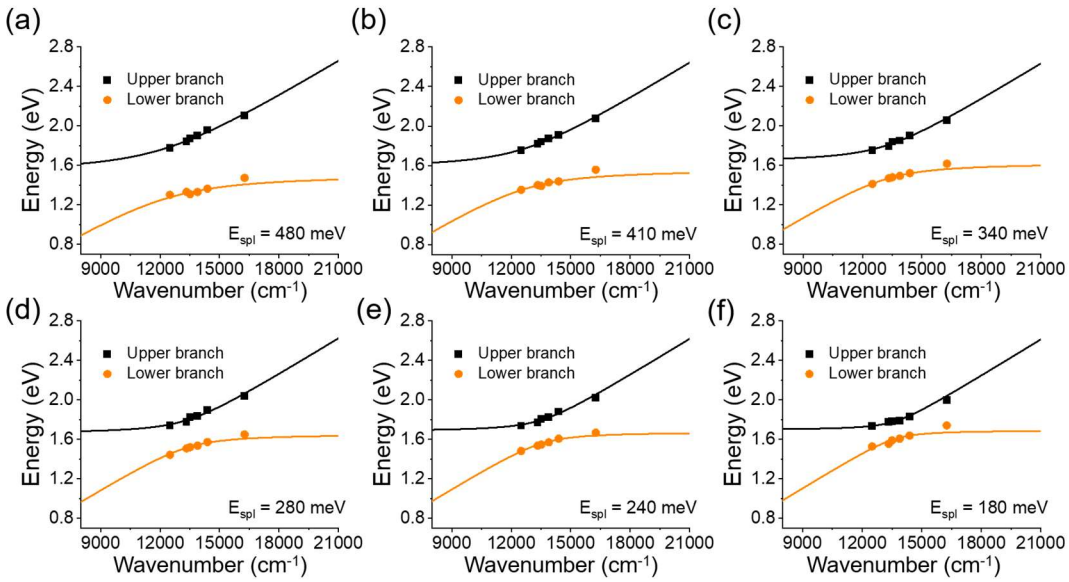

Figure 2.11 Dispersion curves of ATA structures with PNDs of (a) 115, (b) 92, (c) 70, (d) 56, (e) 45, and (f) 29.

between the two modes.

The experimental dispersion data were fitted using the coupled harmonic oscillator model, expressed as:

$$E_{UB,LB} = \frac{E_{LSPR} + E_{FP}}{2} \pm \frac{1}{2}\sqrt{(E_{LSPR} - E_{FP})^2 + {E_{spl}}^2}$$

where E_{UB} and E_{LB} are the energies of the upper and lower branches, E_{LSPR} and E_{FP} are the uncoupled resonance energies of the LSPR and FP nanocavity modes, respectively, and E_{spl} represents the Rabi splitting energy, quantifying the coupling strength between the two modes[59]. To determine whether the ATA structures operate within the strong coupling regime, the following criterion was used:

$$E_{spl} > \sqrt{\frac{{\gamma_{UB}}^2 + {\gamma_{LB}}^2}{2}} = \sqrt{\frac{{\gamma_{LSPR}}^2 + {\gamma_{FP}}^2}{2}}$$

where γ_{UB} and γ_{LB} are the linewidths (full width at half maximum, FWHM) of the upper and lower branches, and γ_{LSPR} and γ_{FP} are the linewidths of the individual uncoupled LSPR and FP nanocavity modes, respectively. From the measured spectra, γ_{UB} and γ_{LB} were estimated to be approximately 150 meV and 110 meV, yielding an energy threshold of roughly 130 meV for the onset of strong coupling. The extracted Rabi splitting energy E_{spl} for the ATA structure with PND = 29 was found to be ~180

meV, which clearly exceeds this threshold. Therefore, ATA structures with PND ≥ 29 can be conclusively identified as operating in the modal strong coupling regime.

2.3.5 Analysis of splitting energy

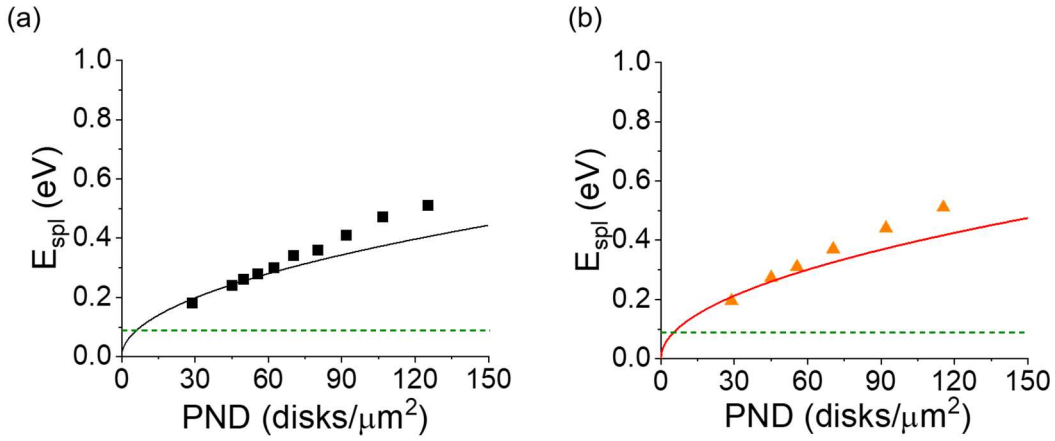

Figure 2.12 Relationship between splitting energy and PND obtained from (a) experiment and (b) simulation. The solid curves represent square-root fitting results, and the green dashed line indicates the simulated splitting energy of a single Au-ND.

As shown in the dispersion results, the coupling strength between the LSPR and FP nanocavity modes exhibits a clear dependence on PND. **Figure 2.12**(a) presents the experimentally extracted splitting energies as a function of PND. It can be seen that the splitting energy increases with PND, indicating that denser Au-NDs arrays facilitate stronger collective coupling. However, the relationship does not follow a simple linear trend, suggesting a more complex dependence of coupling strength on structural density and mode overlap.

To further verify this tendency, FDTD simulations were performed for ATA structures with varying PND values, and the resulting splitting energies are plotted in **Figure 2.12**(b). Although the simulated splitting energies are generally higher than the experimental ones—likely due to the idealized geometry, perfectly smooth interfaces, and absence of fabrication imperfections—the simulated data exhibit the same positive correlation between splitting energy and PND. The quantitative discrepancy between experiment and simulation is reasonable, as real samples typically contain surface roughness, size variations, and interfacial defects that can reduce the effective coupling strength. For small PND structures, Au-NDs interact more weakly with each other,

allowing their coupling behavior to be approximated by the ensemble strong coupling model, in which the Rabi splitting energy scales with the square root of the number of coupled oscillators[60]. Following this analogy, the experimental and simulated results were fitted using a square-root dependence:

$$E_{spl} = A \times \sqrt{PND}$$

where A represents the proportionality constant. The fitting yielded A = 0.03622 for the experimental data and A = 0.03877 for the simulated data.

To further understand this relation, the splitting energy of a single Au-ND was estimated using FDTD simulations of an isolated Au-ND on the TiO_2/Au mirror FP nanocavity. The resulting absorption spectrum (**Figure 2.13**) revealed a splitting energy of approximately 89 meV. When this value is compared to the PND-splitting energy curves (indicated by green dashed lines in **Figure 2.12**), it corresponds to an effective PND of ~5.8 in the experimental data and ~5.2 in the simulated data. This comparison suggests that even an individual Au-ND can exhibit a certain degree of coupling with the FP nanocavity mode, confirming that the modal strong coupling in ATA structures does not purely originate from ensemble collective effects. Furthermore, both the experimental and simulated data exhibit positive deviations from the square-root fitting curve at higher PND values, implying an additional enhancement mechanism beyond the ensemble coupling model. The size-scaling effect of the isolated Au-NDs, the

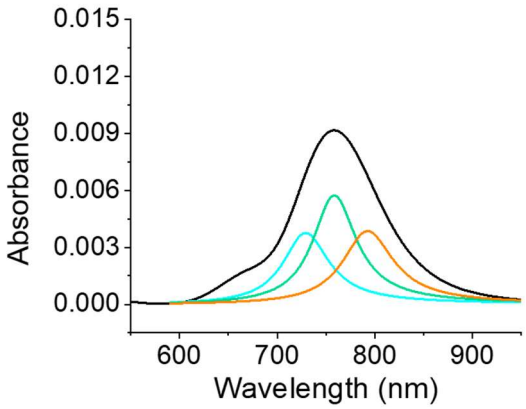

Figure 2.13 Simulated absorption spectrum of an isolated Au-ND on the FP nanocavity. The absorption peak was fitted using a three-component Lorentzian fitting.

deviation of the splitting energy from the square-root relation, and the saturation behaviors of the absorption and near-field responses with increasing PND in the modal strong coupling ATA structures will be systematically discussed in **Chapter 3**.

2.4 Conclusions

In this chapter, modal strong coupling systems were successfully established by integrating the LSPR of Au-NDs with a FP nanocavity possessing a comparable resonance energy. The resulting ATA structures, exhibited distinct energy splitting features in both far-field absorption and near-field spectra, clearly evidencing the formation of hybrid modes. Moreover, analysis of the integrated spectral areas revealed a saturation behavior with increasing PND, which was not observed in the uncoupled AT and other conventional LSPR systems.

The coupling strength of the ATA structures, quantified by the energy splitting derived from dispersion curves, satisfies the criterion of the strong coupling condition. Furthermore, the splitting energy exhibits a square-root dependence on PND in the low-density region, consistent with the theoretical relation for ensemble strong coupling systems. Interestingly, at higher PND values, the splitting energies deviate positively from the square-root trend, suggesting the emergence of additional coupling effects or mode hybridization beyond the standard ensemble regime. Finally, simulations revealed that a single Au-ND coupled with the FP nanocavity produces a splitting energy comparable to that of an Au-NDs array with PNDs in the range of 2.4-5.2. These distinctive behaviors of ATA structures will be systematically explored and mechanistically analyzed in **Chapter 3** to further elucidate the underlying physical origins of modal strong coupling.

2.5 References

1 Wang, S. *et al.* Advancing Silicon-Based Photoelectrodes toward Practical Artificial Photosynthesis. *Accounts of Materials Research* **5**, 809-821, doi:10.1021/accountsmr.4c00022 (2024).

2 Lee, M. H. *et al.* p-Type InP Nanopillar Photocathodes for Efficient Solar-Driven Hydrogen Production. *Angewandte Chemie International Edition* **51**,

10760-10764, doi:10.1002/anie.201203174 (2012).

3 Zappia, M. I. *et al.* Solution-Processed GaSe Nanoflake-Based Films for Photoelectrochemical Water Splitting and Photoelectrochemical-Type Photodetectors. *Advanced Functional Materials* **30**, 1909572, doi:10.1002/adfm.201909572 (2020).

4 Hoffmann, M. R., Martin, S. T., Choi, W. & Bahnemann, D. W. Environmental Applications of Semiconductor Photocatalysis. *Chemical Reviews* **95**, 69-96, doi:10.1021/cr00033a004 (1995).

5 Chen, S. *et al.* Semiconductor-based photocatalysts for photocatalytic and photoelectrochemical water splitting: will we stop with photocorrosion? *Journal of Materials Chemistry A* **8**, 2286-2322, doi:10.1039/C9TA12799B (2020).

6 Hannula, M. *et al.* Improved Stability of Atomic Layer Deposited Amorphous TiO2 Photoelectrode Coatings by Thermally Induced Oxygen Defects. *Chemistry of Materials* **30**, 1199-1208, doi:10.1021/acs.chemmater.7b02938 (2018).

7 Shalan, A. E., Elseman, A. M. & Rashad, M. M. in *Titanium Dioxide - Material for a Sustainable Environment* (ed Dongfang Yang), IntechOpen (2018).

8 Chen, X. & Mao, S. S. Titanium Dioxide Nanomaterials: Synthesis, Properties, Modifications, and Applications. *Chemical Reviews* **107**, 2891-2959, doi:10.1021/cr0500535 (2007).

9 Linsebigler, A. L., Lu, G. & Yates, J. T., Jr. Photocatalysis on TiO_2 Surfaces: Principles, Mechanisms, and Selected Results. *Chemical Reviews* **95**, 735-758, doi:10.1021/cr00035a013 (1995).

10 Roy, N., Sohn, Y. & Pradhan, D. Synergy of Low-Energy {101} and High-Energy {001} TiO_2 Crystal Facets for Enhanced Photocatalysis. *ACS Nano* **7**, 2532-2540, doi:10.1021/nn305877v (2013).

11 Bian, Z., Tachikawa, T. & Majima, T. Superstructure of TiO_2 Crystalline Nanoparticles Yields Effective Conduction Pathways for Photogenerated Charges. *The journal of physical chemistry letters* **3**, 1422-1427,

doi:10.1021/jz3005128 (2012).

12 Tsai, S.-J. & Cheng, S. Effect of TiO_2 crystalline structure in photocatalytic degradation of phenolic contaminants. *Catalysis Today* **33**, 227-237, doi:10.1016/S0920-5861(96)00152-6 (1997).

13 Diebold, U. The surface science of titanium dioxide. *Surface Science Reports* **48**, 53-229, doi:10.1016/S0167-5729(02)00100-0 (2003).

14 Yang, H. G. *et al.* Anatase TiO_2 single crystals with a large percentage of reactive facets. *Nature* **453**, 638-641, doi:10.1038/nature06964 (2008).

15 Fujishima, A., Rao, T. N. & Tryk, D. A. Titanium dioxide photocatalysis. *Journal of Photochemistry and Photobiology C: Photochemistry Reviews* **1**, 1-21, doi:10.1016/S1389-5567(00)00002-2 (2000).

16 Moret, M. P., Zallen, R., Vijay, D. P. & Desu, S. B. Brookite-rich titania films made by pulsed laser deposition. *Thin Solid Films* **366**, 8-10, doi:10.1016/S0040-6090(00)00862-2 (2000).

17 Pottier, A., Chanéac, C., Tronc, E., Mazerolles, L. & Jolivet, J.-P. Synthesis of brookite TiO nanoparticles by thermolysis of TiCl in strongly acidic aqueous media. *Journal of Materials Chemistry* **11**, 1116-1121, doi:10.1039/B100435M (2001).

18 Dodd, A., McKinley, A., Tsuzuki, T. & Saunders, M. Optical and photocatalytic properties of nanocrystalline TiO_2 synthesised by solid-state chemical reaction. *Journal of Physics and Chemistry of Solids* **68**, 2341-2348, doi:10.1016/j.jpcs.2007.07.008 (2007).

19 Selvaraj, U., Prasadarao, A. V., Komarneni, S. & Roy, R. Sol–Gel Fabrication of Epitaxial and Oriented TiO_2 Thin Films. *Journal of the American Ceramic Society* **75**, 1167-1170, doi:10.1111/j.1151-2916.1992.tb05554.x (1992).

20 Macwan, D. P., Dave, P. N. & Chaturvedi, S. A review on nano-TiO_2 sol–gel type syntheses and its applications. *Journal of Materials Science* **46**, 3669-3686, doi:10.1007/s10853-011-5378-y (2011).

21 Samal, S., Kim, D.-W., Kim, K.-S. & Park, D.-W. Direct synthesis of TiO_2 nanoparticles by using the solid-state precursor TiH_2 powder in a thermal

plasma reactor. *Chemical Engineering Research and Design* **90**, 1074-1081, doi:10.1016/j.cherd.2011.10.020 (2012).

22 Zhao, X., Liu, M. & Zhu, Y. Fabrication of porous TiO_2 film via hydrothermal method and its photocatalytic performances. *Thin Solid Films* **515**, 7127-7134, doi:10.1016/j.tsf.2007.03.025 (2007).

23 Byun, D., Jin, Y., Kim, B., Kee Lee, J. & Park, D. Photocatalytic TiO_2 deposition by chemical vapor deposition. *Journal of Hazardous Materials* **73**, 199-206, doi:10.1016/S0304-3894(99)00179-X (2000).

24 Priyalakshmi Devi, K., Goswami, P. & Chaturvedi, H. Fabrication of nanocrystalline TiO_2 thin films using Sol-Gel spin coating technology and investigation of its structural, morphology and optical characteristics. *Applied Surface Science* **591**, 153226, doi:10.1016/j.apsusc.2022.153226 (2022).

25 Albu, D. F. *et al.* Thin Film Fabrication by Pulsed Laser Deposition from TiO_2 Targets in O_2, N_2, He, or Ar for Dye-Sensitized Solar Cells. *Coatings* **12**, 293, doi:10.3390/coatings12030293 (2022).

26 Sammelselg, V. *et al.* TiO_2 thin films by atomic layer deposition: a case of uneven growth at low temperature. *Applied Surface Science* **134**, 78-86, doi:10.1016/S0169-4332(98)00224-4 (1998).

27 Hiller, D. *et al.* Comparison of three titanium-precursors for atomic-layer-deposited TiO_2 for passivating contacts on silicon. *Journal of Vacuum Science & Technology A* **42**, 032406, doi:10.1116/6.0003309 (2024).

28 Karabulut, A., Orak, İ. & Türüt, A. The photovoltaic impact of atomic layer deposited TiO_2 interfacial layer on Si-based photodiodes. *Solid-State Electronics* **144**, 39-48, doi:10.1016/j.sse.2018.02.016 (2018).

29 Shkondin, E. *et al.* Fabrication of high aspect ratio TiO_2 and Al_2O_3 nanogratings by atomic layer deposition. *Journal of Vacuum Science & Technology A* **34**, 031605, doi:10.1116/1.4947586 (2016).

30 Wang, C.-C., Kei, C.-C. & Perng, T.-P. Fabrication of TiO_2 nanotubes by atomic layer deposition and their photocatalytic and photoelectrochemical applications. *Nanotechnology* **22**, 365702, doi:10.1088/0957-4484/22/36/365702 (2011).

31 Mitchell, D. R. G., Attard, D. J. & Triani, G. Transmission electron microscopy studies of atomic layer deposition TiO_2 films grown on silicon. *Thin Solid Films* **441**, 85-95, doi:10.1016/S0040-6090(03)00877-0 (2003).

32 Aarik, J., Aidla, A., Uustare, T. & Sammelselg, V. Morphology and structure of TiO_2 thin films grown by atomic layer deposition. *Journal of Crystal Growth* **148**, 268-275, doi:10.1016/0022-0248(94)00874-4 (1995).

33 Johnson, P. B. & Christy, R. W. Optical Constants of the Noble Metals. *Physical Review B* **6**, 4370-4379, doi:10.1103/PhysRevB.6.4370 (1972).

34 Wang, X., Santschi, C. & Martin, O. J. F. Strong Improvement of Long-Term Chemical and Thermal Stability of Plasmonic Silver Nanoantennas and Films. *Small* **13**, 1700044, doi:10.1002/smll.201700044 (2017).

35 Wang, H., Tam, F., Grady, N. K. & Halas, N. J. Cu Nanoshells: Effects of Interband Transitions on the Nanoparticle Plasmon Resonance. *The Journal of Physical Chemistry B* **109**, 18218-18222, doi:10.1021/jp053863t (2005).

36 Ziemkiewicz, D. & Zielińska-Raczyńska, S. Copper plasmonics with excitons. *Physical Review B* **106**, 205404, doi:10.1103/PhysRevB.106.205404 (2022).

37 Ou, X., Liu, Y., Zhang, M., Hua, L. & Zhan, S. Plasmonic gold nanostructures for biosensing and bioimaging. *Mikrochimica acta* **188**, 304, doi:10.1007/s00604-021-04964-1 (2021).

38 Zhu, H., Yuan, X., Yao, Q. & Xie, J. Shining photocatalysis by gold-based nanomaterials. *Nano Energy* **88**, 106306, doi:10.1016/j.nanoen.2021.106306 (2021).

39 Yang, P., Zheng, J., Xu, Y., Zhang, Q. & Jiang, L. Colloidal Synthesis and Applications of Plasmonic Metal Nanoparticles. *Advanced Materials* **28**, 10508-10517, doi:10.1002/adma.201601739 (2016).

40 Grabar, K. C., Freeman, R. G., Hommer, M. B. & Natan, M. J. Preparation and Characterization of Au Colloid Monolayers. *Analytical Chemistry* **67**, 735-743, doi:10.1021/ac00100a008 (1995).

41 Gao, A. *et al.* Controllable Fabrication of Au Nanocups by Confined-Space Thermal Dewetting for OCT Imaging. *Advanced Materials* **29**, 1701070,

doi:10.1002/adma.201701070 (2017).

42 Ruffino, F. & Grimaldi, M. G. Controlled dewetting as fabrication and patterning strategy for metal nanostructures. *physica status solidi (a)* **212**, 1662-1684, doi:10.1002/pssa.201431755 (2015).

43 Tan, B. J. Y. *et al.* Fabrication of Size-Tunable Gold Nanoparticles Array with Nanosphere Lithography, Reactive Ion Etching, and Thermal Annealing. *The Journal of Physical Chemistry B* **109**, 11100-11109, doi:10.1021/jp045172n (2005).

44 Tseng, A. A., Kuan, C., Chen, C. D. & Ma, K. J. Electron beam lithography in nanoscale fabrication: recent development. *IEEE Transactions on Electronics Packaging Manufacturing* **26**, 141-149, doi:10.1109/TEPM.2003.817714 (2003).

45 Sau, T. K. & Rogach, A. L. Nonspherical Noble Metal Nanoparticles: Colloid-Chemical Synthesis and Morphology Control. *Advanced Materials* **22**, 1781-1804, doi:10.1002/adma.200901271 (2010).

46 Wang, D., Ji, R. & Schaaf, P. Formation of precise 2D Au particle arrays via thermally induced dewetting on pre-patterned substrates. *Beilstein Journal of Nanotechnology* **2**, 318-326, doi:10.3762/bjnano.2.37 (2011).

47 Haynes, C. L., McFarland, A. D., Smith, M. T., Hulteen, J. C. & Van Duyne, R. P. Angle-Resolved Nanosphere Lithography: Manipulation of Nanoparticle Size, Shape, and Interparticle Spacing. *The Journal of Physical Chemistry B* **106**, 1898-1902, doi:10.1021/jp013570+ (2002).

48 Yue, W. *et al.* Electron-beam lithography of gold nanostructures for surface-enhanced Raman scattering. *Journal of Micromechanics and Microengineering* **22**, 125007, doi:10.1088/0960-1317/22/12/125007 (2012).

49 Trasobares, J. *et al.* High speed e-beam lithography for gold nanoarray fabrication and use in nanotechnology. *Beilstein Journal of Nanotechnology* **5**, 1918-1925, doi:10.3762/bjnano.5.202 (2014).

50 Pease, R. F. W. Electron beam lithography. *Contemporary Physics* **22**, 265-290, doi:10.1080/00107518108231531 (1981).

51 Kravets, V. G., Kabashin, A. V., Barnes, W. L. & Grigorenko, A. N. Plasmonic Surface Lattice Resonances: A Review of Properties and Applications. *Chemical Reviews* **118**, 5912-5951, doi:10.1021/acs.chemrev.8b00243 (2018).

52 Auguié, B. & Barnes, W. L. Collective Resonances in Gold Nanoparticle Arrays. *Physical Review Letters* **101**, 143902, doi:10.1103/PhysRevLett.101.143902 (2008).

53 Zou, S., Janel, N. & Schatz, G. C. Silver nanoparticle array structures that produce remarkably narrow plasmon lineshapes. *The Journal of chemical physics* **120**, 10871-10875, doi:10.1063/1.1760740 (2004).

54 Prodan, E., Radloff, C., Halas, N. J. & Nordlander, P. A Hybridization Model for the Plasmon Response of Complex Nanostructures. *Science* **302**, 419-422, doi:10.1126/science.1089171 (2003).

55 Nordlander, P., Oubre, C., Prodan, E., Li, K. & Stockman, M. I. Plasmon Hybridization in Nanoparticle Dimers. *Nano Letters* **4**, 899-903, doi:10.1021/nl049681c (2004).

56 Rechberger, W. *et al.* Optical properties of two interacting gold nanoparticles. *Optics Communications* **220**, 137-141, doi:10.1016/S0030-4018(03)01357-9 (2003).

57 Konijnenberg, A., Adam, A. J. L. & Urbach, H. P. Optical Resonator. *BSc Optics* (2023).

58 Swinehart, D. F. The Beer-Lambert Law. *Journal of Chemical Education* **39**, 333, doi:10.1021/ed039p333 (1962).

59 Törmä, P. & Barnes, W. L. Strong coupling between surface plasmon polaritons and emitters: a review. *Reports on Progress in Physics* **78**, 013901, doi:10.1088/0034-4885/78/1/013901 (2015).

60 Ebbesen, T. W. Hybrid Light–Matter States in a Molecular and Material Science Perspective. *Accounts of Chemical Research* **49**, 2403-2412, doi:10.1021/acs.accounts.6b00295 (2016).

Chapter 3

Quantum-coherence-induced enhancement mechanisms in the modal strong coupling system

3.1 Introduction

In the previous chapter, the modal strong coupling behaviors of the ATA systems were experimentally and numerically demonstrated. The observed energy splittings exceeded the threshold criterion of strong coupling, confirming the establishment of hybridized plasmon-photon states. For ATA structures with low PND, the splitting energy exhibited a square-root dependence on PND, consistent with the behavior typically observed in ensemble strong coupling systems. However, several distinct and unexplained phenomena emerged beyond the scope of conventional ensemble coupling theory. Unlike ordinary absorbing systems that obey the Lambert-Beer law, the ATA structures displayed a saturation in integrated absorption intensity as PND increased, indicating that absorption no longer scales linearly with the number of plasmonic particles. Furthermore, even an isolated single Au-ND exhibited a measurable splitting energy comparable to that of an Au-NDs array with a low PND, suggesting that a strong-coupling-like interaction also exists at the single-particle level. In addition, for arrays with higher PND values, the energy splitting deviated positively from the expected square-root dependence, implying the emergence of additional coupling effects or higher-order modal interactions.

These unique and nontrivial phenomena strongly suggest that a distinct interaction mechanism operates within the ATA modal strong coupling systems, one that cannot be fully described by classical ensemble strong coupling models. Therefore, in this chapter, I will delve deeper into the underlying mechanisms of modal strong coupling, combining experimental observations, electromagnetic simulations, and theoretical analysis to provide a comprehensive and physically reasonable explanation for these unconventional behaviors. Specifically, I will investigate hot-electron injection efficiency, near-field spatial distributions, and the PEC analysis to elucidate the effect

of quantum coherence in the modal strong coupling system.

3.1.1 Electron transfer dynamics in metal-semiconductor heterojunctions

Before addressing the transient spectroscopic results, it is essential to first understand how photoexcited charge carriers behave at the metal-semiconductor interface, since the interfacial electron transfer dynamics fundamentally determine the subsequent hot-electron injection and photocatalytic efficiency. In plasmonic and PEC systems, the formation of a heterojunction between a metal and a semiconductor fundamentally governs the pathways of light-induced charge transfer and energy conversion. When a metallic nanoparticle is brought into contact with a semiconductor, their Fermi levels equilibrate through interfacial charge redistribution, resulting in the formation of a Schottky barrier or an ohmic junction depending on the relative work functions[1,2]. For an n-type semiconductor such as TiO_2, the Fermi level lies closer to its conduction band, while that of a metal is typically lower. Upon contact, electrons flow from TiO_2 into the metal until equilibrium is established, bending the semiconductor bands upward near the interface and forming a Schottky barrier (**Figure 3.1**)[3,4]. This potential barrier allows the flow of photogenerated electrons from the metal into the semiconductor under illumination but prevents the reverse flow in the dark, thereby facilitating rectified charge transfer[5,6].

In the case of the Au-TiO_2 heterojunction investigated in this work, light irradiation excites the LSPR of Au-NDs. The collective oscillation of conduction electrons leads

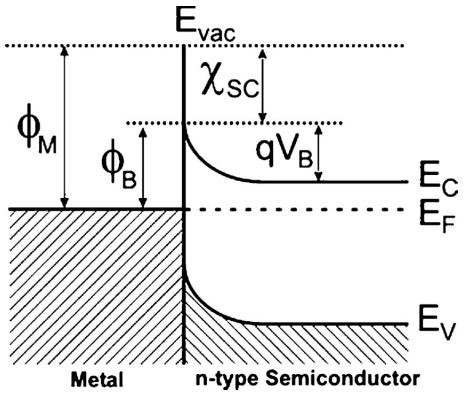

Figure 3.1 Schematic illustration of Schottky barrier[4].

to the generation of energetic “hot” carriers through nonradiative damping, such as Landau damping. Among them, hot electrons with sufficient energy to overcome the Schottky barrier are injected into the TiO_2 conduction band, where they can participate in reduction reactions at the semiconductor surface or be probed by transient spectroscopic techniques. The corresponding hot holes remain in the Au nanoparticle, typically participating in oxidation reactions. This charge separation, driven by the asymmetric interfacial potential, is the key to plasmon-induced photocatalysis and underlies the transient absorption features analyzed in the following section.

Conversely, when the semiconductor is p-type (for example, Cu_2O or NiO), the situation is reversed. The Fermi level of the semiconductor lies closer to the valence band, generally higher than that of the metal. Upon contact, electrons flow from the metal into the p-type semiconductor, bending the bands downward near the interface and forming a barrier for hole transport. Under light excitation, hot holes generated in the metal can be injected into the valence band of the semiconductor, where they drive oxidation reactions, while the corresponding hot electrons remain in the metal to participate in reduction. This opposite carrier flow direction highlights the critical role of the semiconductor type in dictating whether hot electrons or hot holes dominate the photocatalytic behavior[7].

Beyond metal-semiconductor junctions, it is noteworthy that even pure metallic nanoparticles can sustain both oxidation and reduction reactions simultaneously on different facets or sites. Due to the strong local electric fields and rapid electron redistribution within metallic nanostructures, spatially separated redox reactions can proceed on a single particle—oxidation at high-index or positively charged facets, and reduction at regions of negative potential[8]. This intrinsic bidirectional charge flow enables metallic nanostructures to catalyze complete redox cycles without requiring an external semiconductor support, emphasizing the versatility of plasmonic metals in driving surface chemical transformations.

Altogether, understanding these fundamental electron transfer processes in heterojunctions—across n-type, p-type, and even all-metal configurations—is essential for interpreting the transient absorption results and elucidating how plasmonic

excitation couples with interfacial charge dynamics in the subsequent analyses.

3.1.2 Transient absorption spectroscopy

After understanding the fundamental mechanisms of electron transfer at metal-semiconductor interfaces, it becomes crucial to experimentally verify these dynamics and evaluate how efficiently hot carriers are generated and injected across the junction. Various techniques have been developed to measure and analyze the generation and injection efficiency of hot electrons in plasmonic systems, including two-photon photoemission spectroscopy (2PPE)[9,10], surface photovoltage spectroscopy (SPV)[11-13], ultrafast terahertz spectroscopy (TRTS)[14,15], and femtosecond transient absorption spectroscopy (TAS)[16]. Among these, TAS offers distinct advantages in investigating ultrafast charge carrier dynamics in metal-semiconductor heterostructures[17,18], particularly for quantitatively evaluating the hot electron injection efficiency from Au-NDs into the TiO_2 layer[19,20]. TAS enables real-time monitoring of photoinduced processes with femtosecond temporal resolution, allowing direct observation of carrier excitation, transfer, and recombination dynamics.

During a TAS measurement, two femtosecond laser pulses—designated as the pump and probe pulses—are used with a precisely controlled time delay between them. The pump pulse excites the plasmonic Au-NDs, inducing the generation of hot electrons through non-radiative decay of LSPR. Some of these hot electrons are injected into the conduction band of TiO_2, forming a transient charge-separated state[21]. The subsequent probe pulse interrogates the sample at varying time delays, detecting changes in optical density (ΔOD) that correspond to the presence of these transient states. To obtain the ΔOD signal, the pump pulse train is periodically modulated using a mechanical chopper—allowing every other pulse to be alternately blocked and transmitted—so that the probe intensity with and without pump excitation can be sequentially measured. The difference between these two probe signals (pump-on and pump-off) is then recorded to determine the ΔOD. By systematically varying the time delay between pump and probe pulses, a ΔOD-time profile is constructed, revealing the temporal evolution of the excited-state population. The rise dynamics of ΔOD reflect the hot electron injection

process, the maximum value of ΔOD (ΔOD_{max}) approximately indicates the total amount of the injected electrons, whereas the decay dynamics correspond to the recombination or relaxation of the injected electrons. Therefore, TAS serves as a powerful tool to directly elucidate the ultrafast kinetics of hot electron generation, transfer, and recombination within the ATA modal strong coupling system.

3.1.3 Near-field mapping

To directly visualize the spatial distribution of optical near-fields at the nanometer scale, several advanced characterization techniques have been developed, including scattering-type scanning near-field optical microscopy[22,23] (s-SNOM), electron energy-loss spectroscopy (EELS) in scanning or transmission electron microscopy[24,25], cathodoluminescence (CL)[26,27], and photoemission-based methods[28]. Among these, photoemission-based near-field mapping stands out as one of the most intuitive and direct approaches, as it visualizes the local photoemission intensity that is intrinsically linked to the optical near-field enhancement on the sample surface[29].

Photoemission (PE) is a nonlinear relaxation process in which electrons are emitted from a material surface via multiphoton excitation under intense light illumination[30]. When the photon energy of the incident light is lower than the material's work function (Φ), multiple photons must be simultaneously absorbed to excite an electron above the vacuum level. The corresponding photoemission yield (I_{PE}) can be expressed as a power-law dependence on the local electric field (I_E) as:

$$I_{PE} = |I_E|^{2n}$$

where n is the nonlinear order (typically n = 2-4 for femtosecond laser excitation). Because the photoemission intensity scales strongly with the near-field amplitude, the spatial distribution of PE signals directly reflects the near-field intensity profile on the nanostructure surface ($I_{NF} \propto |I_E|^2$ where I_{NF} is the near-field intensity). Therefore, PE-based imaging provides a powerful, indirect but quantitative probe of plasmonic near-field localization.

A particularly effective technique utilizing this mechanism is PEEM. In PEEM, the sample is placed inside an ultrahigh-vacuum chamber and biased with a high negative

potential (typically several kVs). Upon irradiation with femtosecond laser pulses, multiphoton PE occurs preferentially at regions of enhanced near-field intensity, where the local electric field is sufficiently strong to overcome the nonlinear emission threshold[31]. The emitted electrons are then accelerated toward an electrostatic lens system and projected onto a phosphor screen or detector, forming a magnified image of the spatial distribution of photoemission intensity (**Figure 3.2**)[32]. Since PEEM imaging directly originates from the nonlinear near-field-enhanced photoemission process, the resulting PEEM contrast provides nanoscale visualization of local optical field enhancement, plasmonic mode distribution, and coupling behavior. Moreover, by tuning the excitation wavelength or polarization, PEEM enables the selective excitation of distinct plasmonic modes, making it a powerful diagnostic tool for studying complex hybrid systems such as the ATA modal strong coupling structure.

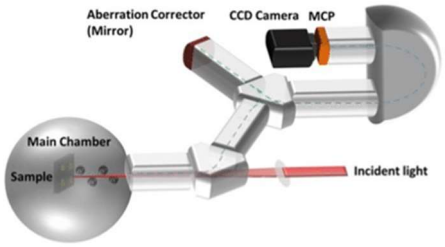

Figure 3.2 Schematic illustration of PEEM[32].

3.1.4 PEC performance evaluation

To verify the practical functionality of the designed photoelectrode, PEC performance tests are ultimately conducted. These measurements provide direct evidence of the light-driven charge generation, separation, and transfer efficiency, thereby linking the optical and electronic properties of the nanostructured materials to their catalytic activity. In a typical PEC setup, a three-electrode configuration is employed, focusing on the photoelectrode's reaction behavior (**Figure 3.3**)[33,34]. The photoelectrode serves as the working electrode, where photoinduced redox reactions occur. A reference electrode, such as Ag/AgCl or saturated calomel electrode (SCE), is placed in close proximity to monitor the absolute potential applied to the working electrode. Meanwhile, an inert counter electrode, often composed of platinum mesh or carbon rod,

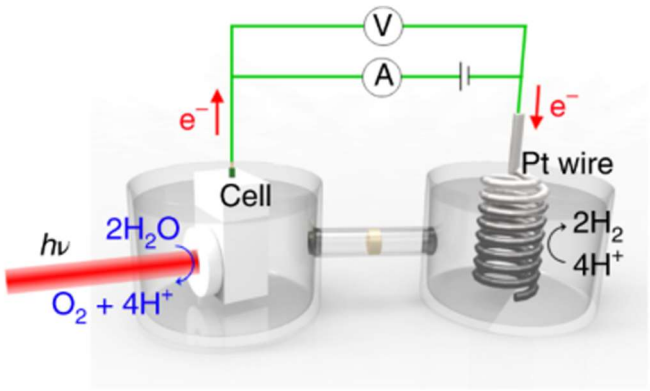

Figure 3.3 Schematic illustration of the PEC measurement[34].

is positioned in a separate compartment to complete the circuit and facilitate the counter reaction. All electrodes are connected via conductive leads to an external potentiostat, enabling precise control of the applied potential and measurement of photocurrent.

To comprehensively assess PEC performance, several key metrics are used:

Photocurrent-voltage characteristic (I-V Curve):

The most fundamental evaluation is the measurement of the photocurrent density (I, in mA) as a function of the applied potential (V). The onset potential, saturation photocurrent, and overall I-V curve shape provide insight into charge separation efficiency and the energetic alignment between the photoelectrode and electrolyte.

Incident photon-to-current conversion efficiency (IPCE):

The IPCE quantifies the ratio of the number of collected electrons to the number of incident photons at a specific wavelength, thereby reflecting the wavelength-dependent light-to-current conversion efficiency. It is mathematically expressed as:

$$IPCE = \frac{1240 \times I_p(A/cm^2)}{\lambda(nm) \times P_{in}(W/cm^2)} \times 100\%$$

where I_p is the measured photocurrent density, λ is the wavelength of incident light, and P_{in} is the irradiance of the incident beam. The IPCE spectrum directly reveals the active photoresponse region and allows comparison of the spectral dependence with the optical absorption characteristics of the material.

Internal and External Quantum Efficiencies:

The internal quantum efficiency (IQE) represents the fraction of absorbed photons that

successfully generate collected electrons:

$$IQE = \frac{IPCE}{Abs}$$

where Abs is the optical absorption of the photoelectrode at each wavelength. On the other hand, the external quantum efficiency (EQE) accounts for both optical and electrical processes, and is defined as:

$$EQE = \frac{Number\ of\ collected\ electrons}{Number\ of\ incident\ photons}$$

In many PEC and photovoltaic systems, EQE and IPCE are used interchangeably when optical reflection and transmission losses are negligible.

Applied Bias Photon-to-Current Efficiency (ABPE):

To evaluate the overall solar-to-hydrogen conversion capability, the ABPE is calculated under simulated solar illumination as[35]:

$$ABPE(\%) = \frac{I_p \times (1.23 - V_{bias})}{P_{in}} \times 100\%$$

where V_{bias} is the externally applied potential. This parameter directly correlates with the energy conversion efficiency of the PEC cell. Through these evaluations, the PEC performance of the photoelectrodes can be quantitatively analyzed and compared.

3.2 Experimental details

3.2.1 TAS measurements

To evaluate the hot-electron generation and injection dynamics of the modal strong coupling ATA systems, TAS was employed to probe their ultrafast carrier behavior. Prior to the measurements, large-area (1.5 × 1.5 mm^2) arrays of Au-NDs was prepared. An additional 7-nm TiO_2 layer was conformally deposited on the ATA samples using ALD to recover surface damage and contamination on the TiO_2 film caused during the EBL fabrication process. This post-treatment ensured a clean semiconductor interface for efficient charge transfer from the plasmonic nanostructures[34].

During TAS measurement, a regenerative amplified Ti:sapphire laser system (fundamental wavelength 800 nm, pulse duration ~25 fs, repetition rate 1 kHz) served as the light source. The fundamental output beam was divided into two parts: one as the pump pulse and the other as the probe pulse. The pump pulse was directed into a

collinear optical parametric amplifier (OPA; Light Conversion, TOPAS-C) to generate a tunable excitation wavelength that matches the absorption band of the sample. The pump beam was mechanically chopped at 500 Hz, allowing alternate measurement of the reflected probe signal with and without excitation, which enables the calculation of the ΔOD. For the probe pulse, a noncollinear difference frequency generator (NDFG) was employed to produce a mid-infrared probe with a center wavelength of approximately 3500 nm. This wavelength corresponds to the intraband transition energy of TiO_2, thus serving as a sensitive probe for the injected electron population. The time delay between the pump and probe pulses was precisely controlled by a motorized linear delay stage, providing a temporal resolution better than 50 fs. Both pulses were weakly focused onto the sample surface using a concave mirror to achieve a loosely focused beam (spot diameter > 200 μm) to avoid damage on sample and ensure homogeneous excitation. The pump pulse was normally incident on the sample, while the probe pulse was introduced at an oblique angle of ~22° (the Brewster angle)[36] to maximize reflection detection efficiency and reduce interference artifacts. The pump power was adjusted between 0.6-1.0 mW, while the probe power was maintained around 0.1 mW at the sample surface.

The reflected probe signal was detected by a liquid-nitrogen-cooled mercury cadmium telluride (MCT) detector, and the differential signal between pump-on and pump-off conditions was processed to obtain the ΔOD. The ΔOD signal represents the change in optical density corresponding to the population of injected or excited electrons in the TiO_2 layer. By scanning the time delay between the pump and probe pulses, a transient kinetic trace was acquired, reflecting both the hot-electron injection dynamics and the subsequent recombination or trapping processes. To quantitatively describe the transient behavior, the rising edge of the ΔOD curve (electron injection process) was fitted by a Gaussian function representing the instrument response, while the decay process was fitted using a second-order reaction model that accounts for bimolecular recombination[37,38]:

$$[e^-] = \frac{[e^-]_0}{kt \times [e^-]_0 + 1} + C$$

where $[e^-]$ is the transient electron population at delay time t (derived from ΔOD), $[e^-]_0$ is the initial injected electron concentration (corresponding to ΔOD_{max}), k is the recombination rate constant, and C is a constant background offset.

The maximum transient signal (ΔOD_{max}) corresponds to the maximum population of injected hot electrons, and can therefore be used to evaluate the efficiency of hot-electron generation. The apparent quantum efficiency (AQE) for hot-electron injection from Au-NDs into TiO_2 was calculated by:

$$AQE = \frac{\Delta OD_{max}}{n \times Abs}$$

where n is the number of incident photons per unit area, and Abs is the optical absorption of the ATA structure at the excitation wavelength. This parameter represents the fraction of absorbed photons that successfully produce detectable injected electrons, serving as an effective figure-of-merit for comparing different ATA configurations and correlating their optical coupling strength with carrier dynamics.

3.2.2 Near-field distribution mapping

PEEM was employed to visualize and compare the near-field distributions of the modal strong coupling ATA structures and the conventional LSPR-type AT structures. Since it is challenging to resolve the near-field pattern of periodic arrays, a series of Au-ND clusters with various particle numbers (PNs) were fabricated to serve as simplified models for near-field observation. These clusters provide a bridge between isolated nanoparticles and periodic arrays, allowing us to understand the evolution of field coupling with increasing PN. Each Au-ND cluster consisted of 80-nm-diameter Au-NDs separated by an interparticle gap of 64 nm, identical to that of the periodic array corresponding to a PND of 56. The clusters were designed with point symmetry centered on the central Au-ND, and the number of surrounding Au-NDs was systematically varied, forming structures with 1 (PN = 1) up to 6 (PN = 91) concentric layers.

In the PEEM system, a Ti:sapphire femtosecond laser delivering pulses of approximately 100 fs duration and a tunable central wavelength range from 690 to 970 nm was used as the excitation source. The excitation beam was circularly polarized

using a quarter-wave (λ/4) plate to ensure isotropic excitation of plasmonic modes, and the incident laser power was set to 164 mW. During operation, a negative bias of –20 kV was applied to the sample stage to accelerate the photoemitted electrons, and the nonlinear coefficient was ~3.84. The emitted electrons were amplified by a microchannel plate (MCP) under an applied voltage of ~1.55 kV to enhance the signal intensity and then projected onto a phosphor screen for imaging. The PEEM measurements were conducted under a field of view (FOV) of approximately 2.5 μm in diameter, with 0.5 s exposure time per frame, and the images were accumulated 32 times to improve the signal-to-noise (S/N) ratio. The resulting PEEM images represent the spatial distribution of PE intensity, which directly reflects the near-field enhancement and localization associated with the modes of the structures. The acquired PEEM images were quantitatively analyzed using ImageJ software. The experimental results were then compared with finite element method (FEM) simulations performed in collaboration with the Sasaki group. By systematically comparing the PE maps of ATA and AT structures, as well as clusters with increasing PN and the corresponding simulation results, the evolution of near-field coupling behavior and the emergence of quantum coherence within the system can be comprehensively elucidated.

3.2.3 PEC performance evaluation

The PEC properties of the modal strong coupling ATA structures and the conventional LSPR-type AT structures were systematically evaluated by IPCE measurements using a standard three-electrode configuration. All samples used in this measurement were using large-area Au-NDs arrays inlaid with a 7-nm- TiO_2 layer deposited by ALD, identical to the samples used in TAS experiments, to ensure a consistent interface quality and reproducibility of hot-electron injection. The backside and sidewalls of the substrate were coated with an In/Ga alloy (weight ratio 2:1) and affixed to a sealed Teflon cell using silver paste. Only a circular aperture of 1 cm in diameter was exposed to the electrolyte and illuminated during measurement.

In the PEC setup, the ATA or AT structure served as the working electrode, a SCE was employed as the reference electrode, and a Pt wire functioned as the counter electrode.

These electrodes were connected through an electrochemical analyzer system (ALS/CH Instruments 852C, ALS Co. Ltd.) to control and monitor the applied bias and current response. The electrolyte consisted of a 0.1 mol·dm^{-3} aqueous KOH solution containing 1 vol% triethanolamine (TEOA), which acted as a sacrificial electron donor to efficiently scavenge photogenerated holes and promote unidirectional single-electron transfer reactions at the photoelectrode surface[39]. This electrolyte composition is known to suppress charge recombination and thus accurately reflect the photoinduced electron injection efficiency. A constant potential of +0.6 V vs. SCE was applied to the working electrode during the measurements to ensure sufficient driving force for electron extraction from the semiconductor conduction band. The photocurrent response was determined by measuring the difference between the current densities recorded under light illumination and in the dark condition, effectively eliminating background contributions from non-photoactive processes.

The light source was a broadband halogen lamp, providing continuous spectral illumination across the UV to NIR regions. To obtain wavelength-dependent IPCE spectra, a series of bandpass optical filters (bandwidth < 15 nm) were used to select specific excitation wavelengths. The photon flux at each wavelength was carefully calibrated using a power meter to ensure accurate conversion from light intensity to photon number. The measured photocurrent density at each wavelength was then used to calculate IPCE. By comparing the IPCE spectra of the ATA and AT structures, the influence of modal strong coupling on hot-electron generation, transport, and collection efficiencies can be directly evaluated. Particularly, enhancement trends at resonance wavelengths reflect the effect of quantum coherence in optical absorption, carrier dynamics, and interfacial charge transfer pathways.

3.3 Results and discussions

3.3.1 AQE evaluation

Large-area Au-ND arrays with various PND were fabricated for both ATA and AT configurations, and subsequently coated with a 7-nm TiO_2 layer. These samples were subjected to TAS measurements to evaluate their hot-electron generation and injection

efficiencies, quantitatively expressed by the AQE. For the ATA structures, due to the formation of upper and lower branches under modal strong coupling, two distinct excitation conditions were applied: one excited at the upper branch and another at the lower branch. In contrast, the AT structures were excited only once at their LSPR resonance wavelength, as they exhibit a single plasmonic absorption band. To avoid possible sample degradation under high-energy illumination, the pump power for the upper-branch excitation (0.6 mW) was set slightly lower than that for the lower-branch excitation of ATA structures and LSPR excitation of AT structures (1.0 mW).

Figure 3.4(a–c) shows the transient ΔOD time profiles obtained from the ATA and AT structures with varying PND. A clear trend can be observed: for both types of structures, the ΔOD_{max} increases with increasing PND, indicating a greater number of injected hot electrons. This increase is, however, more pronounced in the ATA systems compared with their AT counterparts. Particularly, at high PND values, the ΔOD_{max} of ATA structures was nearly twice that of the AT structures, implying a substantial enhancement in hot-electron generation or transfer efficiency enabled by modal strong coupling.

To eliminate the influence of absorption difference among the samples, the AQE was calculated, and the resulting AQE values are plotted in **Figure 3.4**(d). For the AT structures, the AQE remains nearly constant across different PNDs, reflecting the localized and non-interacting nature of their plasmonic resonances. In sharp contrast,

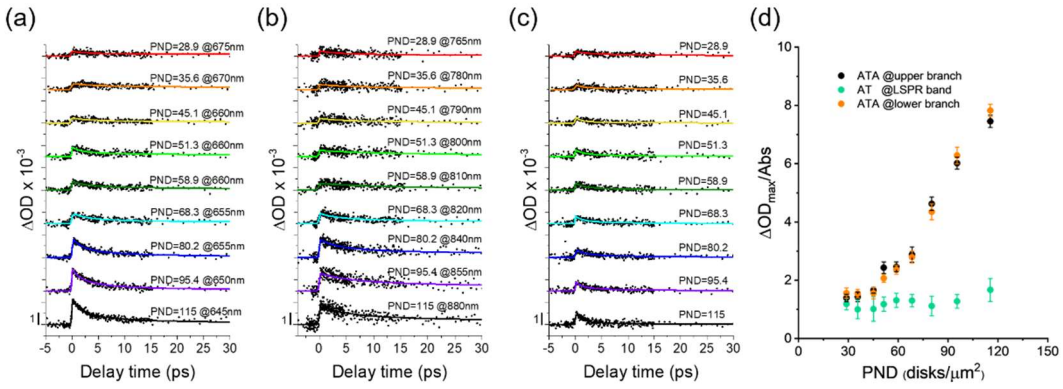

Figure 3.4 Time profiles of the transient absorption measurements performed at (a) the upper branch of ATA, (b) the lower branch of ATA, and (c) the LSPR band of AT for various PND. (d)AQE as a function of the PND.

the ATA structures exhibit a distinct increase in AQE with rising PND, particularly when PND > 45, for both upper- and lower-branch excitations. This monotonic enhancement demonstrates that modal strong coupling promotes more efficient photoinduced carrier processes as the PND increases. It is worth emphasizing that this AQE enhancement cannot be attributed solely to stronger near-field intensity, since the integral near-field peak areas of ATA structures was found to saturate with increasing PND (as shown in **Chapter 2**). This observation implies that the improvement in AQE arises from collective coupling effects unique to the modal strong coupling regime, which effectively increase the hot-electron generation and injection probabilities beyond the limits of conventional LSPR systems.

3.3.2 Near-field distribution mapping

To further elucidate the spatial near-field characteristics associated with the modal strong coupling in the ATA systems, PEEM was performed on Au-ND clusters with various PN. In these samples, the Au-NDs were not inlaid in TiO_2 to avoid weakening the PE signal, which primarily originates from the interfacial edges between the Au-NDs and the TiO_2 layer. This design allows the intrinsic optical near-field behavior to be directly visualized. The obtained PE spectra are presented in **Figure 3.5**. Although no distinct energy splitting was observed in the PE band of ATA clusters—likely due to the large intercluster gap and low surface coverage of the entire area—the ATA clusters exhibit significantly broader PE bandwidths and markedly stronger emission intensities

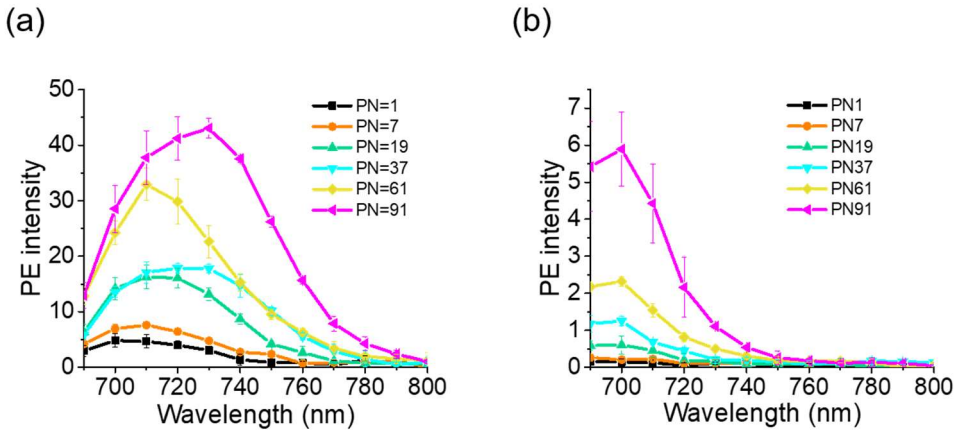

Figure 3.5 PE spectra of (a) ATA and (b) AT structures

compared to their AT counterparts. This spectral broadening and intensity enhancement indicate the coupling between LSPR and FP nanocavity modes and enhanced local field confinement within the ATA clusters.

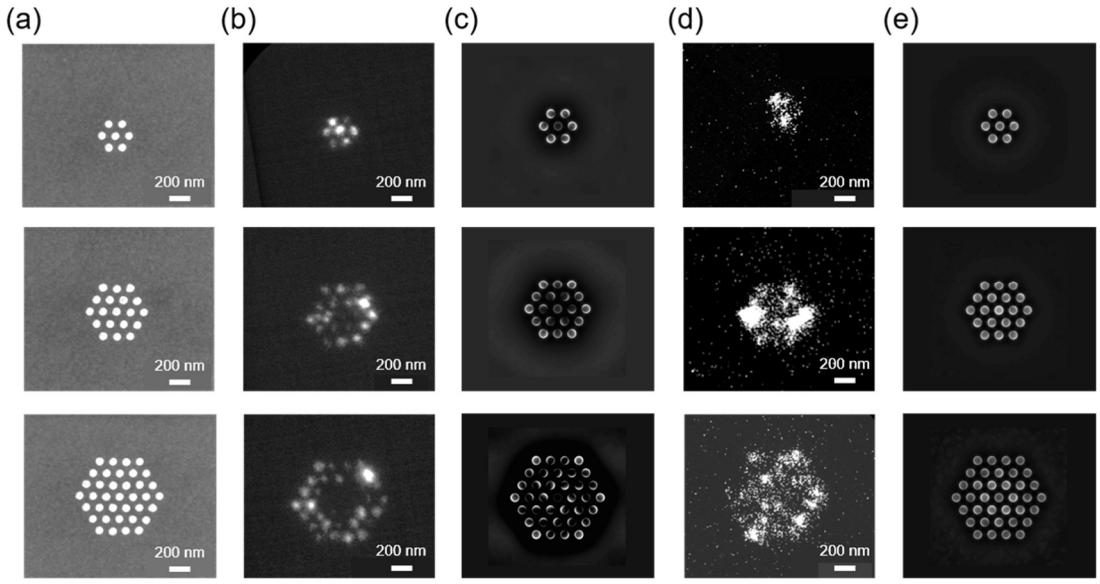

Figure 3.6 (a) SEM images of ATA structures with PNs of 7, 19, and 37 (from top to bottom). (b) Corresponding PE distribution images and (c) simulated near-field distributions (all Au-NDs in the cluster irradiated) obtained by FEM. (d) PE distribution images of AT structures with the corresponding PNs, and (e) their simulated near-field distributions under full-cluster irradiation.

Representative SEM images are shown in **Figure 3.6**(a). In **Figure 3.6**(b,d), which display the PE intensity mappings of ATA and AT clusters respectively, notable differences in spatial distribution can be observed. For the ATA clusters, the PE intensity is highly localized at the rim regions of the clusters, while the central areas remain relatively dark, particularly for clusters with higher PNs. In contrast, the AT clusters exhibit a more uniform PE distribution across the entire cluster, suggesting conventional dipole-dipole near-field coupling behavior. To provide a theoretical reference, FEM simulations of the near-field distributions were conducted by Sasaki group (**Figures 3.6**(c,e)). The simulated near-field patterns reproduce the experimental tendencies remarkably well: enhanced local fields at the edge and suppressed central field amplitudes in ATA clusters, in contrast to the homogeneous field profiles observed in AT clusters. This consistency between PEEM observations and numerical simulations validates that the PE intensities indeed reflect the real-space near-field

distributions.

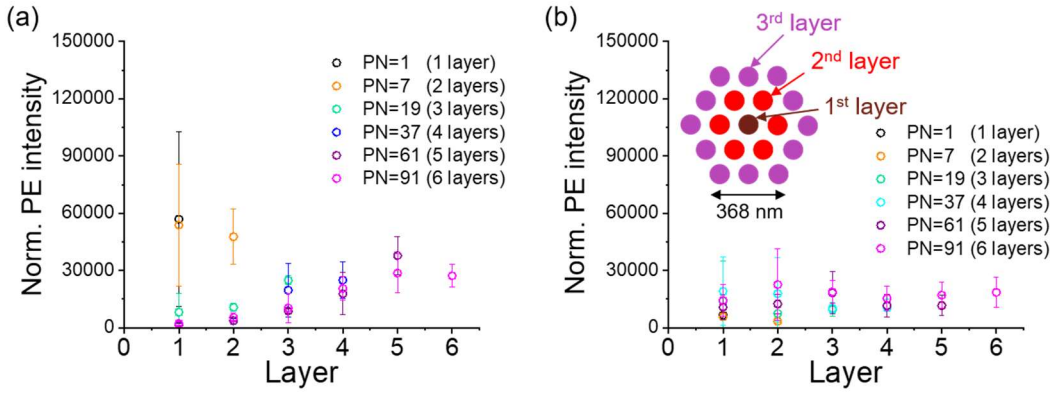

Figure 3.7 Normalized PE intensity of each layer of the Au-ND clusters of (a) ATA and (B) AT structures.

A quantitative analysis of the layer-resolved PE intensity for each cluster is summarized in **Figure 3.7**, which clearly reveals that the outer layers of ATA clusters contribute disproportionately to the overall emission intensity as the PN increases. This spatial asymmetry of field localization becomes more pronounced with larger cluster size, indicating a progressive modification of the collective optical response under modal strong coupling. The unique near-field pattern observed exclusively in the ATA structures strongly suggests that interparticle interactions within the coupled cavity cannot be explained merely by conventional dipole-dipole coupling or local field enhancement effects. Instead, the results imply the presence of a cooperative, coherence-driven energy redistribution mechanism among the Au-NDs mediated by the photonic mode of the FP nanocavity. Combining the insights from the TAS and AQE results in **Section 3.3.1** and the near-field mapping presented here, we can conclude that the enhanced photoresponse and spatially structured field distributions in the ATA systems stem from a quantum-coherence-assisted energy transfer process. This mechanism enables the delocalization and phase correlation of excitations across multiple nanoparticles, facilitating efficient energy exchange beyond the scope of classical plasmonic interactions. The detailed theoretical formulation and discussion of this mechanism will be developed in the following section.

3.3.3 Quantum coherence in modal strong coupling ATA

When comparing the modal strong coupling ATA structures and the LSPR-only AT structures, the key distinction lies in the interaction channels available to the Au-NDs. In both ATA and AT, neighboring Au-NDs can interact through conventional dipole-dipole near-field coupling, characterized by the coupling strength g_2 (**Figure 3.8**(a)). However, only in the ATA structures, where Au-NDs are placed on a FP nanocavity, an additional interaction channel g_1 arises due to coupling between the LSPR mode and the FP cavity mode. This additional term g_1 not only modifies the optical mode landscape but also establishes a phase correlation among the Au-NDs mediated by the cavity field. Because the FP nanocavity mode sustains a standing wave with a uniform phase distribution, all Au-NDs coupled to the cavity mode are driven in phase. This phase synchronization effectively induces spatial quantum coherence among Au-NDs within a finite region, defined as the coherence area. Within this area, the Au-NDs are no longer independent units but instead form a collective hybrid quantum state that coherently exchanges energy via the shared cavity mode. In other words, under modal strong coupling, the Au-NDs and the FP cavity field must be treated as a single inseparable quantum entity. Such collective coherence enables a new interaction channel among Au-NDs, mediated through the FP nanocavity—denoted as g_2'—in addition to the direct dipole-dipole coupling g_2 (**Figure 3.8**(b)). The effective Hamiltonian of this system thus includes both local (LSPR-LSPR) and nonlocal (LSPR-cavity-LSPR) coupling terms, resulting in delocalized optical excitation that allows energy transfer and redistribution across the coherence area. This mechanism bears strong analogy to the quantum-coherence-assisted energy migration observed in natural photosynthetic complexes, where coherence among chromophores facilitates efficient excitation energy transfer toward reaction centers[40-43].

Summarizing this concept, the FP nanocavity assists the formation of quantum coherence among Au-NDs within each coherence area, allowing them to share

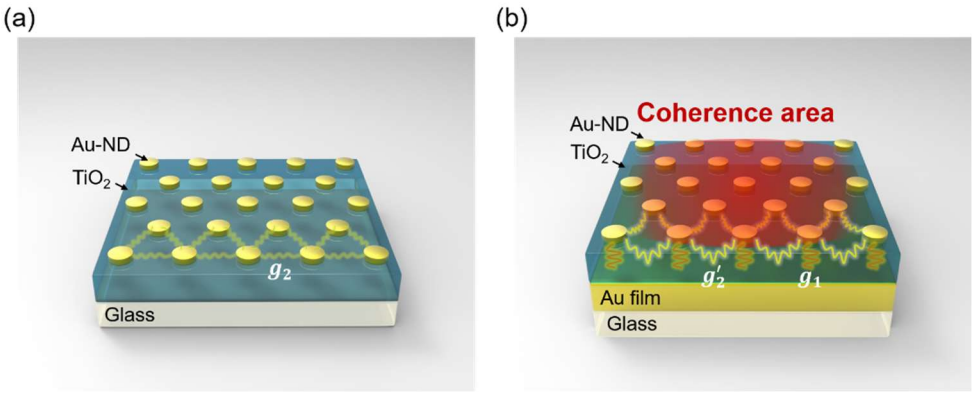

Figure 3.8 Schematic illustration of (a) the interparticle near-field interaction (g_2) between the Au-NDs in AT, (b) the coherent coupling between Au-NDs and the FP cavity (g_1) and the cavity-mediated interaction between Au-NDs within coherence area (g_2').

excitation energy collectively. In an ideal, perfectly periodic ATA array, all Au-NDs would possess identical optical and relaxation characteristics, so energy sharing alone would not directly improve the efficiency of hot-electron injection. However, in real experimental samples, structural inhomogeneities and fabrication imperfections inevitably introduce slight variations among the Au-NDs—such as differences in geometry, crystalline orientation, or defect states. These variations lead to site-dependent relaxation dynamics, where certain Au-NDs act as fast-damping sites, more efficient at converting plasmonic energy into hot electrons.

According to the theoretical model assisted by Ishihara group, when quantum coherence is established within a cluster containing a certain portion of relatively-fast-damping Au-NDs, excitation energy absorbed by any Au-ND within the coherence area can be redistributed to the more dissipative ones, enhancing the overall hot-electron injection efficiency. In contrast, in AT structures lacking coherence, each Au-ND behaves independently, and only those directly excited fast-damping sites contribute to injection. Consequently, quantum coherence in ATA allows the effective collection of excitations and their funneling into energetically favorable relaxation channels. This coherence-driven energy sharing provides a unified explanation for several experimentally observed phenomena:

1. Saturation of integral absorption and near-field intensity:

Because energy absorption in ATA occurs collectively over coherence areas rather than

individual Au-NDs, the overall absorption becomes delocalized. Once coherence areas cover the entire surface, further increases in nanoparticle density (PND) do not increase total absorption, leading to the observed saturation behavior.

2. Unique near-field patterns in PEEM:

The g_2' interaction mediated by the FP cavity introduces additional coupling modes that reshape the spatial field distribution, producing the rim-enhanced and center-dark PE patterns observed only in ATA clusters. Furthermore, FEM simulations, performed with assistance from the Sasaki group using localized excitation on only the central Au-ND of the cluster (**Figure 3.9**), reveal distinct near-field behaviors. In the AT cluster, the strong near-field enhancement is confined to the excited central Au-ND, while the surrounding Au-NDs exhibit weak responses, primarily governed by dipole-dipole interaction g_2. In contrast, in the ATA cluster, pronounced excitation is observed across nearly all Au-NDs, arising from the cavity-mediated coupling g_2' that reflects the presence of quantum coherence.

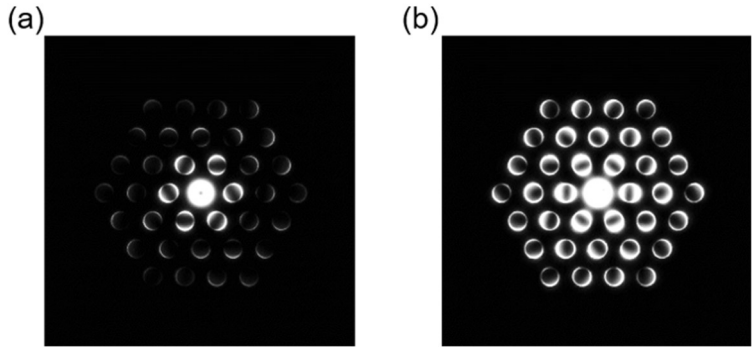

Figure 3.9 Simulated near-field distribution of (a) AT and (b) ATA clusters with only the central Au-ND excited.

3. Positive deviation from the square-root curve in the E_{spl}-PND relation:

Theoretical calculations performed assisted by Ishihara's group incorporating the g_2' term successfully reproduce the experimentally observed positive deviation from the simple square-root dependence of splitting energy on PND. In contrast, the model without g_2' shows a purely square-root dependence, identical to the ensemble strong coupling regime. Therefore, this positive deviation provides strong evidence that the

nonlocal, cavity-mediated g_2' interaction—and consequently, the formation of quantum coherence—is responsible for the enhanced splitting energy and collective photoresponse in the ATA modal strong coupling system.

4. Enhanced AQE with increasing PND:

As PND increases, the coherence areas include more Au-NDs, statistically increasing the likelihood that efficient fast-damping sites are contained within each coherent domain (**Figure 3.10**). This boosts the probability of energy transfer to those sites, resulting in the experimentally observed monotonic increase in AQE with PND. In contrast, in the AT structures, although a higher PND also increases the total number of efficient fast-damping sites, each Au-ND absorbs light independently, and the excitation probability per particle remains constant. Consequently, the AQE, in which the absorption has been normalized, shows no dependence on PND.

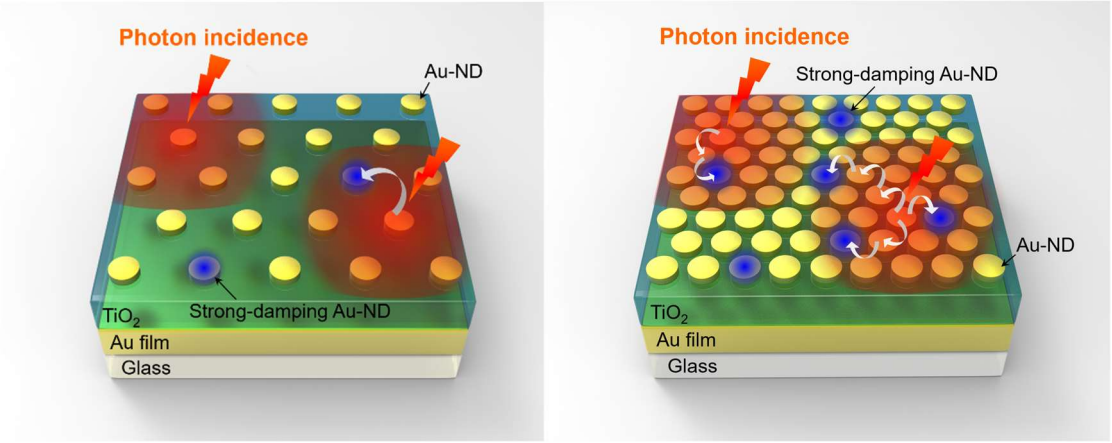

Figure 3.10 Schematic illustrations of the mechanism responsible for the enhancement of AQE. The red regions denote the coherence areas, while the blue-colored Au-NDs represent the efficient fast-damping sites.

Next, I attempted to characterize the size of the coherence area. Although direct visualization of coherence areas is experimentally challenging, their effective size can be inferred from the splitting energy-PND relation discussed in Chapter 2. The equivalence between the splitting energy of a single isolated Au-ND and that of a periodic Au-NDs array with PND ≈ 5.8 (experiment) or PND ≈ 5.2 (simulation) suggests that the optical response of an individual Au-ND already corresponds to that of each Au-ND within these periodic structures. This suggests that the effective

interaction range of a single Au-ND is comparable to the coupling range within those arrays, thereby defining the size of the coherence area. By considering the interparticle distance, the coherence area can be estimated to correspond to a circular region with a diameter of approximately 460 nm in experimental data and 495 nm in simulation.

3.3.4 PEC performance evaluation

After identifying the presence and role of quantum coherence within the modal strong coupling ATA system, the PEC performance was further investigated to examine the practical impact of this effect. The IPCE was measured using large-area Au-ND arrays inlaid with a 7-nm TiO_2 layer—similar to those used for TAS experiments. **Figure 3.11**(a,b) presents the IPCE action spectra of ATA and AT structures with different PNDs, alongside their corresponding absorption spectra. Consistent with the TAS results, the IPCE intensity under upper-branch excitation of ATA and under the LSPR excitation of AT both show a positive correlation with PND. However, when excited at the lower branch of ATA, the IPCE peak becomes much less pronounced. This suppression is most likely attributed to the reduced photon energy at longer wavelengths, resulting in hot holes with insufficient oxidation potential to effectively drive the surface reaction.

To quantitatively evaluate the photo-conversion performance, the IQEs of the upper-branch excited ATA and the LSPR band excited AT were calculated by compensating for the optical absorption of each sample (**Figure 3.11**(c)). The IQE of ATA under upper-branch excitation is markedly higher than that of AT under LSPR excitation, and it increases with PND. In contrast, AT structures show little increment in IQE values with the increased PND. This enhancement of IQE in ATA can be directly linked to the quantum-coherence-assisted energy transfer mechanism discussed earlier. Within the coherence area formed by coupling between the FP nanocavity and the Au-NDs, hot carriers generated in any Au-ND can coherently redistribute energy among neighboring Au-NDs. Consequently, energy transfer to fast-damping Au-NDs—those with efficient hot-electron injection channels—is promoted, leading to a significant improvement in overall charge-separation efficiency. This coherence-mediated process effectively

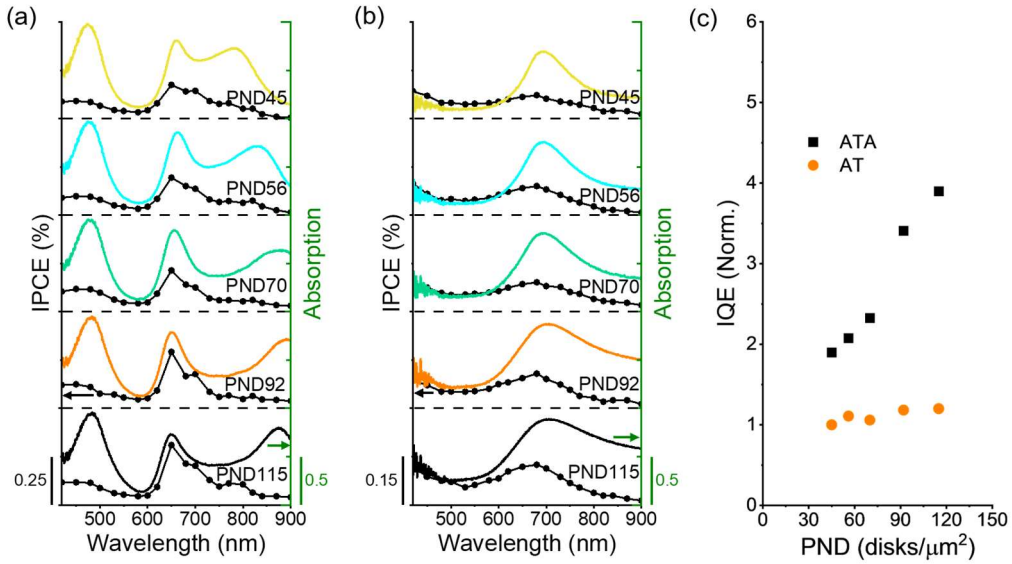

Figure 3.11 IPCE action spectra of (a) ATA and (b) AT structures. (c) Normalized IQE at the IPCE peak wavelength for both ATA and AT structures

broadens the spatial domain of light harvesting beyond individual nanoparticles.

In summary, the PEC characterization confirms that the modal strong coupling system not only enhances the hot-electron injection efficiency—consistent with the TAS results—but also significantly boosts the overall PEC conversion efficiency. Although the overall performance is still limited due to surface damage of the TiO_2 layer induced by the EBL fabrication process, the observed enhancement clearly demonstrates the effectiveness of the coupling strategy. This indicates that integrating quantum coherence via modal strong coupling offers a promising pathway toward next-generation plasmonic photoelectrodes capable of driving highly efficient PEC processes, including solar-driven water splitting and artificial photosynthesis in the near future.

3.4 Conclusions

In this chapter, the modal strong coupling ATA was systematically investigated to elucidate its optical, photophysical, and PEC characteristics in comparison with the conventional LSPR-based AT. The transient absorption spectroscopy revealed that the AQE of ATA was significantly enhanced relative to AT, with a clear positive correlation between AQE and the PND. This trend could not be explained by simple near-field

enhancement, as the integrated field intensity of ATA was found to saturate with increasing PND.

Near-field mapping by PEEM further unveiled distinctive spatial field distributions unique to ATA clusters, characterized by rim-dominated photoemission and field suppression at the cluster centers—features absent in the AT counterparts. These findings indicate that additional interactions beyond ordinary dipole-dipole coupling are operative in ATA under modal strong coupling.

By integrating these experimental observations, the existence of **quantum coherence** within the ATA system was proposed. Under strong coupling with the FP nanocavity, Au-NDs within a coherence domain interact coherently through the cavity field g_1, establishing a secondary coupling channel g_2' in addition to direct dipole-dipole coupling g_2. This coherence-assisted interaction allows collective energy sharing among Au-NDs in the same coherence area, effectively delocalizing the photonic excitation across multiple nanoparticles. The coherence mechanism accounts for several experimental phenomena:

(1) enhancement and PND-dependence of AQE,

(2) characteristic near-field patterns observed by PEEM,

(3) saturation behavior of optical absorption and near-field intensity, and

(4) positive deviation of splitting energy from the ideal square-root dependence on PND discussed in **Chapter 2**.

From the comparison between isolated single Au-ND and low-PND arrays, the coherence area was estimated to have a circular domain with a diameter of approximately 460-495 nm, based on both experimental and simulated results.

Furthermore, PEC measurements confirmed that the modal strong coupling not only enhances the hot-electron injection efficiency, but also substantially improves the IQE under upper-branch excitation. The IQE exhibited a strong positive dependence on PND, corroborating the crucial role of quantum coherence in facilitating efficient energy and charge transfer through cavity-mediated coupling.

Overall, these findings establish quantum coherence as a fundamental mechanism underlying the superior optical and PEC properties of modal strong coupling systems.

This discovery not only deepens our understanding of light-matter interactions in hybrid plasmonic-photonic nanostructures, but also provides valuable insights for the rational design of next-generation photoelectrodes. Leveraging coherence-assisted energy transfer could open new pathways toward highly efficient PEC processes and artificial photosynthesis driven by visible and near-infrared light.

3.5 References

1 Skromme, B. J. in *Encyclopedia of Materials: Science and Technology* (eds K. H. Jürgen Buschow *et al.*) 1-12 Elsevier (2003).

2 Brongersma, M. L., Halas, N. J. & Nordlander, P. Plasmon-induced hot carrier science and technology. *Nature Nanotechnology* **10**, 25-34, doi:10.1038/nnano.2014.311 (2015).

3 Altuntas, H. *et al.* Interface state density analyzing of Au/TiO_2(rutile)/n–Si Schottky barrier diode. *Surface and Interface Analysis* **42**, 1257-1260, doi:10.1002/sia.3331 (2010).

4 Polotai, A. *et al.* Effect of Cr Additions on the Electrical Properties of Ni-$BaTiO_3$ Ultra-Thin Multilayer Capacitors. *Journal of Electroceramics - J ELECTROCERAM* **23**, 6-12, doi:10.1007/s10832-008-9496-0 (2009).

5 Tian, Y. & Tatsuma, T. Mechanisms and Applications of Plasmon-Induced Charge Separation at TiO_2 Films Loaded with Gold Nanoparticles. *Journal of the American Chemical Society* **127**, 7632-7637, doi:10.1021/ja042192u (2005).

6 Clavero, C. Plasmon-induced hot-electron generation at nanoparticle/metal-oxide interfaces for photovoltaic and photocatalytic devices. *Nature Photonics* **8**, 95-103, doi:10.1038/nphoton.2013.238 (2014).

7 Zhang, X., Chen, Y. L., Liu, R.-S. & Tsai, D. P. Plasmonic photocatalysis. *Reports on Progress in Physics* **76**, 046401, doi:10.1088/0034-4885/76/4/046401 (2013).

8 Linic, S., Christopher, P. & Ingram, D. B. Plasmonic-metal nanostructures for efficient conversion of solar to chemical energy. *Nature Materials* **10**, 911-921, doi:10.1038/nmat3151 (2011).

9 Ueba, H. & Gumhalter, B. Theory of two-photon photoemission spectroscopy of surfaces. *Progress in Surface Science* **82**, 193-223, doi:10.1016/j.progsurf.2007.03.002 (2007).

10 Onda, K., Li, B. & Petek, H. Two-photon photoemission spectroscopy of TiO_2 (110) surfaces modified by defects and O_2 or H_2O adsorbates. *Physical Review B* **70**, 045415, doi:10.1103/PhysRevB.70.045415 (2004).

11 Kronik, L. & Shapira, Y. Surface photovoltage phenomena: theory, experiment, and applications. *Surface Science Reports* **37**, 1-206, doi:10.1016/S0167-5729(99)00002-3 (1999).

12 Cavalcoli, D. & Cavallini, A. Surface photovoltage spectroscopy - method and applications. *physica status solidi c* **7**, 1293-1300, doi:10.1002/pssc.200983124 (2010).

13 Donchev, V. Surface photovoltage spectroscopy of semiconductor materials for optoelectronic applications. *Materials Research Express* **6**, 103001, doi:10.1088/2053-1591/ab3bf0 (2019).

14 Spies, J. A. *et al.* Terahertz Spectroscopy of Emerging Materials. *The Journal of Physical Chemistry C* **124**, 22335-22346, doi:10.1021/acs.jpcc.0c06344 (2020).

15 Tayvah, U. T., Neu, J., Spies, J. A., Schmuttenmaer, C. A. & Brudvig, G. W. Ultrafast terahertz spectroscopy provides insight into charge transfer efficiency and dynamics in artificial photosynthesis. *Photosynthesis Research* **151**, 145-153, doi:10.1007/s11120-020-00798-9 (2022).

16 Berera, R., van Grondelle, R. & Kennis, J. T. M. Ultrafast transient absorption spectroscopy: principles and application to photosynthetic systems. *Photosynthesis Research* **101**, 105-118, doi:10.1007/s11120-009-9454-y (2009).

17 Zhang, J., Zhu, B., Zhang, L. & Yu, J. Femtosecond transient absorption spectroscopy investigation into the electron transfer mechanism in photocatalysis. *Chemical Communications* **59**, 688-699, doi:10.1039/D2CC06300J (2023).

18 Furube, A. *et al.* Femtosecond Transient Absorption Spectroscopy on

Photocatalysts: $K_4Nb_6O_{17}$ and $Ru(bpy)_3^{2+}$-Intercalated $K_4Nb_6O_{17}$ Thin Films. *The Journal of Physical Chemistry B* **106**, 3065-3072, doi:10.1021/jp011083o (2002).

19 Tamaki, Y. *et al.* Trapping dynamics of electrons and holes in a nanocrystalline TiO_2 film revealed by femtosecond visible/near-infrared transient absorption spectroscopy. *Comptes Rendus Chimie* **9**, 268-274, doi:10.1016/j.crci.2005.05.018 (2006).

20 Kafizas, A. *et al.* Where Do Photogenerated Holes Go in Anatase:Rutile TiO_2? A Transient Absorption Spectroscopy Study of Charge Transfer and Lifetime. *The Journal of Physical Chemistry A* **120**, 715-723, doi:10.1021/acs.jpca.5b11567 (2016).

21 Long, R. & Prezhdo, O. V. Instantaneous Generation of Charge-Separated State on TiO_2 Surface Sensitized with Plasmonic Nanoparticles. *Journal of the American Chemical Society* **136**, 4343-4354, doi:10.1021/ja5001592 (2014).

22 Chen, X. *et al.* Modern Scattering-Type Scanning Near-Field Optical Microscopy for Advanced Material Research. *Advanced Materials* **31**, 1804774, doi:10.1002/adma.201804774 (2019).

23 Neuman, T. *et al.* Mapping the near fields of plasmonic nanoantennas by scattering-type scanning near-field optical microscopy. *Laser & Photonics Reviews* **9**, 637-649, doi:10.1002/lpor.201500031 (2015).

24 Backx, C., de Groot, C. P. M. & Biloen, P. Electron energy loss spectroscopy and its applications. *Applications of Surface Science* **6**, 256-272, doi:10.1016/0378-5963(80)90016-1 (1980).

25 Egerton, R. F. Electron energy-loss spectroscopy in the TEM. *Reports on Progress in Physics* **72**, 016502, doi:10.1088/0034-4885/72/1/016502 (2009).

26 Yacobi, B. G. & Holt, D. B. in *Cathodoluminescence Microscopy of Inorganic Solids* (eds B. G. Yacobi & D. B. Holt) 55-88 Springer US (1990).

27 Ronald Marcus, C., Volker, E., Ralf, H. & Ludwig Josef, B. Near-field detection cathodoluminescence investigations. *Journal of Physics D: Applied Physics* **31**, 1918, doi:10.1088/0022-3727/31/15/022 (1998).

28 Grubisic, A., Schweikhard, V., Baker, T. A. & Nesbitt, D. J. Coherent Multiphoton Photoelectron Emission from Single Au Nanorods: The Critical Role of Plasmonic Electric Near-Field Enhancement. *ACS Nano* **7**, 87-99, doi:10.1021/nn305194n (2013).

29 Dai, Y. Ultrafast photoemission electron microscopy: A multidimensional probe of nonequilibrium physics. *Chinese Physics B* **33**, 038703, doi:10.1088/1674-1056/ad174a (2024).

30 Pendry, J. B. Theory of photoemission. *Surface Science* **57**, 679-705, doi:10.1016/0039-6028(76)90355-1 (1976).

31 Feng, J. & Scholl, A. in *Science of Microscopy* (eds Peter W. Hawkes & John C. H. Spence) 657-695 Springer New York (2007).

32 Yu, H. *et al.* Exploring Coupled Plasmonic Nanostructures in the Near Field by Photoemission Electron Microscopy. *ACS nano* **10**, doi:10.1021/acsnano.6b06206 (2016).

33 Ueno, K., Oshikiri, T. & Misawa, H. Plasmon-Induced Water Splitting Using Metallic-Nanoparticle-Loaded Photocatalysts and Photoelectrodes. *ChemPhysChem* **17**, 199-215, doi:10.1002/cphc.201500761 (2016).

34 Shi, X. *et al.* Enhanced water splitting under modal strong coupling conditions. *Nature Nanotechnology* **13**, 953-958, doi:10.1038/s41565-018-0208-x (2018).

35 Hamid, S. B. A., Teh, S. J., Lai, C. W., Perathoner, S. & Centi, G. Applied bias photon-to-current conversion efficiency of ZnO enhanced by hybridization with reduced graphene oxide. *Journal of Energy Chemistry* **26**, 302-308, doi:10.1016/j.jechem.2016.11.006 (2017).

36 Hönig, D. & Möbius, D. Reflectometry at the Brewster angle and Brewster angle microscopy at the air-water interface. *Thin Solid Films* **210-211**, 64-68, doi:10.1016/0040-6090(92)90169-C (1992).

37 Tamaki, Y., Hara, K., Katoh, R., Tachiya, M. & Furube, A. Femtosecond Visible-to-IR Spectroscopy of TiO_2 Nanocrystalline Films: Elucidation of the Electron Mobility before Deep Trapping. *The Journal of Physical Chemistry C* **113**, 11741-11746, doi:10.1021/jp901833j (2009).

38 Rossi, G. *et al.* Charge carrier dynamics and visible light photocatalysis in vanadium-doped TiO_2 nanoparticles. *Applied Catalysis B: Environmental* **237**, 603-612, doi:10.1016/j.apcatb.2018.06.011 (2018).

39 Pellegrin, Y. & Odobel, F. Sacrificial electron donor reagents for solar fuel production. *Comptes Rendus Chimie* **20**, 283-295, doi:10.1016/j.crci.2015.11.026 (2017).

40 Engel, G. S. *et al.* Evidence for wavelike energy transfer through quantum coherence in photosynthetic systems. *Nature* **446**, 782-786, doi:10.1038/nature05678 (2007).

41 Scholes, G. D., Fleming, G. R., Olaya-Castro, A. & van Grondelle, R. Lessons from nature about solar light harvesting. *Nature Chemistry* **3**, 763-774, doi:10.1038/nchem.1145 (2011).

42 Brédas, J.-L., Sargent, E. H. & Scholes, G. D. Photovoltaic concepts inspired by coherence effects in photosynthetic systems. *Nature Materials* **16**, 35-44, doi:10.1038/nmat4767 (2017).

43 Rather, S. R. & Scholes, G. D. From Fundamental Theories to Quantum Coherences in Electron Transfer. *Journal of the American Chemical Society* **141**, 708-722, doi:10.1021/jacs.8b09059 (2019).

Chapter 4

Dephasing effect on AQE in the modal strong coupling ATA

4.1 Introduction

In the previous chapter, quantum coherence was identified as a key factor governing the enhancement of AQE in the modal strong coupling ATA system. Within the coherence area, multiple Au-NDs can coherently exchange and redistribute optical energy through the FP nanocavity. When the included Au-NDs in the coherence area act as relatively fast-damping efficient sites, the collective energy can be funneled toward these sites, leading to more efficient hot-electron injection into the TiO_2 layer. This mechanism suggests that the damping behavior of individual Au-NDs plays a decisive role in determining the overall performance of the coherence area. Since the damping of LSPR is intrinsically linked to its dephasing time, any modification in dephasing behavior should directly influence the degree of quantum coherence sustained within the system.

In this chapter, we focus on elucidating the dephasing effect on quantum coherence in the ATA modal strong coupling system. To achieve this, faster-dephasing nanostructures are deliberately introduced as model systems, enabling a systematic investigation of how increased plasmon dephasing affects the collective optical response, hot-electron dynamics, and coherence-related enhancement mechanisms. Through both experimental observation and theoretical calculation, we aim to clarify how coherence collapses or persists under different dephasing conditions, thereby deepening the understanding of coherence-assisted processes in the modal strong coupling systems.

4.1.1 Coherence and dephasing in coupled nanophotonic systems

In the previous chapter, the role of quantum coherence was identified as a key factor governing the unconventional optical responses and PEC efficiencies observed in the ATA modal strong coupling systems. To further deepen the understanding of this phenomenon, this chapter begins by introducing the fundamental concepts of coherence. Quantum coherence represents the phase correlation between different quantum states

or oscillating dipoles[1], and serves as the fundamental element that distinguishes coherent light-matter interactions from classical, incoherent processes. In strong-coupled nanophotonic systems, such as the ATA structure, coherence manifests through the synchronized oscillation of electromagnetic fields and collective electron motion across multiple resonant components. This phase-locked oscillation allows the system to behave as a unified hybrid mode rather than as separate plasmonic or photonic entities, giving rise to phenomena such as mode splitting, Rabi oscillation, and energy delocalization across spatially separated nanostructures.

From a temporal perspective, coherence can be understood as the persistence of a well-defined phase relationship between oscillating dipoles or quantum states over time. Its lifetime—often characterized by the dephasing time (τ)—determines how long the system retains its wave-like nature before random scattering events, electron-phonon interactions, or inhomogeneous broadening destroy the phase alignment[2-4]. A longer coherence time implies that the system can maintain collective oscillation for more optical cycles, enabling quantum interference and energy exchange to occur coherently between modes. Conversely, rapid dephasing causes the hybrid system to revert to a classical regime, where the oscillators act independently and energy transfer proceeds incoherently[5].

In contrast, from a spatial viewpoint, coherence reflects how consistently the oscillation phase is maintained across different regions of the coupled system[6,7]. For example, in the ATA geometry, spatial coherence (coherence area) governs whether the LSPR modes of individual nanostructures can oscillate in-phase and collectively couple to the FP nanocavity mode. When the coherence length exceeds the interparticle separation, constructive interference reinforces the hybrid field distribution, producing delocalized polaritonic modes. However, when dephasing mechanisms shorten the coherence length to below this spatial scale, phase randomness emerges, leading to localization of energy and a breakdown of collective mode formation.

The interplay between temporal and spatial coherence thus lies at the heart of the system's optical behavior. Dephasing acts as the primary process that disrupts these coherent correlations, progressively converting the system's dynamics from a quantum-

coherent to an incoherent regime. Therefore, understanding and controlling dephasing is essential for determining whether quantum coherence can survive within practical plasmonic-photonic hybrid systems. In the following section, we focus on dephasing time manipulation, introducing model nanostructures with tunable damping rates to experimentally and theoretically probe how increasing dephasing influences coherence persistence and the resulting optical performance and hot carrier transfer behavior.

4.1.2 Dephasing time manipulation

To investigate the influence of dephasing on quantum coherence in the modal strong coupling ATA system, it is essential to introduce nanostructures with relatively faster dephasing times while maintaining a comparable resonance wavelength to the periodic Au-ND arrays. Several strategies have been reported to tune the plasmonic dephasing time of metallic nanostructures. These include substituting the metallic material (e.g., replacing Au with Ag, Al, Cu, or even alloy)[8], modifying the adhesion or spacer layer thickness to alter energy dissipation at the metal-substrate interface[9,10], changing the dielectric environment surrounding the nanostructure[11], introducing surface roughness or grain boundaries[12], and reshaping the nanostructure geometry to modify its local field confinement and radiative damping characteristics[13]. Among these approaches, tailoring the shape of the nanostructure is the most straightforward and compatible method for the ATA system, as it can be readily achieved through a single-step EBL process without complex multilayer alignment. The structural dependence of dephasing time thus becomes a key parameter.

Previous studies have revealed that the plasmon dephasing time is strongly affected by several structural factors, including the aspect ratio[14], surface curvature[15], sharpness of edges or tips[16], particle size[17], and interparticle coupling strength[18]. In particular, nanostructures featuring sharp tips or low-coordination site, exhibit substantially shorter dephasing times than those with smooth and symmetric geometries (e.g., disks or spheres)[19,20]. This is attributed to enhanced nonradiative damping and electron-surface scattering at high-curvature regions, leading to faster plasmon relaxation and broader linewidths in the optical spectra. In the following sections, I incorporated

nanotriangle structures as the faster-dephasing sites into the ATA system to examine how plasmon dephasing affects the coherence-mediated mechanisms discussed in the previous chapter.

4.2 Experimental details

4.2.1 Sample fabrication

The fabrication procedure followed a similar process to that described in **Chapter 2**, with several modifications as detailed below.

A bottom Au mirror and a TiO_2 layer were sequentially deposited on a clean SiO_2 substrate to form the FP nanocavity. In this work, the resonance wavelength of the FP cavity mode was tuned to approximately ~775 nm by adjusting the TiO_2 thickness to ~210 nm. During the EBL process, special care was taken to realize nanostructures with sharp tips. A thinner layer of positive photoresist (ZEP-520A, Zeon Chemicals; diluted with anisole at a 1:2 ratio) was spin-coated onto the TiO_2 surface at 300 rpm for 5 s followed by 2500 rpm for 60 s, resulting in a resist thickness of about 110 nm. To minimize charging effects on the resist surface—which can lead to pattern rounding—an additional conductive coating (e-spacer Z) was spin-coated at 300 rpm for 5 s and 3000 rpm for 60 s after the soft-bake step.

For the nanostructure design, larger structures were intentionally selected to ensure high tip sharpness of the Au nanotriangles (Au-NTs). The Au-NDs were designed with a diameter of 120 nm, and the inscribed circle diameter of the Au-NTs was also set to 120 nm to maintain an identical interparticle gap (60 nm) within the array. During EBL exposure, an additional electron dose was locally applied to the tips of the Au-NTs to further enhance their tip definition and minimize edge rounding. After exposure, the substrates were developed in ZED-N50 developer for 4 minutes, followed by rinsing in ZMD-B solution for 1 minute to terminate the reaction and stabilize the developed pattern. The substrates were then left to air dry. Finally, arrays composed of both Au-NDs and Au-NTs were fabricated with varying ratios of the two components to systematically control the dephasing characteristics. The percentage of triangles (PoT) in each array was varied from 0% (pure Au-ND array) to 100% (pure Au-NT array).

The resulting mixed arrays are hereafter referred to as Au-ND-NT mixed structures (Au-NDTms).

4.2.2 Optical properties and AQE characterization

The methods used for optical characterization and surface morphology analysis were generally identical to those described in **Chapter 2**, with several modifications specific to the Au-NDTms. For the optical spectrum measurements, in addition to the spectra measured by PMA, spectra with wavelengths longer than 955 nm were additionally obtained using Fourier-transform infrared spectroscopy (FTIR; FT/IR-6000TM-M, JASCO Inc.). This supplementary measurement enabled continuous spectral coverage across the entire plasmonic resonance region of the modal strong coupling structures.

The transient absorption spectroscopy (TAS) measurements were also performed following the procedure introduced in **Chapter 3**, with minor adjustments. Specifically, the probe beam wavelength was set to 2500 nm to achieve a stronger signal intensity. In this wavelength region, no distinct absorption features of the Au-NDTms were observed, thus eliminating the risk of spectral overlap or interference with the transient signals. The absence of intrinsic absorption ensured that the observed dynamics originated solely from the plasmon-induced processes rather than background optical artifacts. The obtained optical and transient responses were subsequently correlated with the AQE measurements to evaluate how the introduction of faster-dephasing nanostructures (Au-NTs) influences the overall hot electron transfer processes under modal strong coupling conditions.

4.3 Results and discussions

4.3.1 FDTD simulation of dephasing times

To confirm that the Au-NTs indeed exhibit faster dephasing dynamics than the Au-NDs, FDTD simulations were performed. The simulated models were based on the AT structures, each containing a single Au-ND or Au-NT placed on the TiO_2 layer. In the simulations, a plane-wave light truncated at a specific time was used as the excitation source to trigger LSPR. The computational domain was set as a 5-μm square region surrounded by perfectly matched layer (PML) boundary conditions[21] to eliminate

artificial reflections. A time monitor was positioned 10 nm away from the edge of the Au-ND and the tip of the Au-NT, respectively, and 1 nm above the TiO_2 surface, allowing accurate tracking of the electric-field decay behavior.

The simulated temporal profiles of the dominant electric field component are shown in **Figure 4.1**, where the decay of the electric field amplitude was fitted using a single-exponential dephasing model[22]:

$$A_{EF} = A \times e^{\frac{-(t-t_0)}{\tau}}$$

where A_{EF} represents the instantaneous electric field amplitude, A is the normalized maximum amplitude (set to 1), t is the time delay, t_0 is the cutoff point of the incident pulse (set to 0), and τ denotes the dephasing time. From the fitted decay curves, the extracted dephasing time τ for Au-NTs was found to be approximately 10% shorter than that of Au-NDs, confirming that the sharper tips of Au-NTs indeed accelerate plasmon damping. This result aligns well with previous theoretical predictions that the concentration of electric fields at sharp vertices enhances nonradiative decay such as Landau damping, thereby shortening the overall dephasing time.

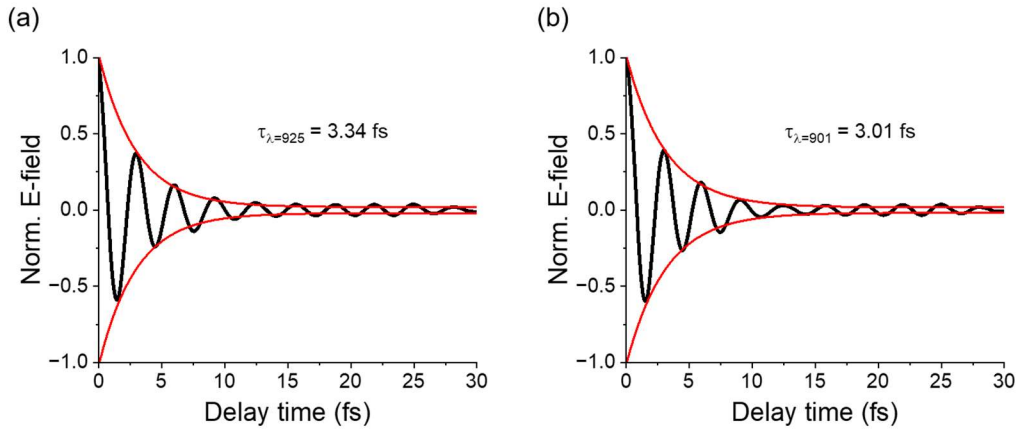

Figure 4.1 Simulated dephasing time profiles and extracted dephasing times obtained by FDTD simulations for (a) individual Au-ND and (b) individual Au-NT loaded AT structures.

4.3.2 Surface morphology of the Au-NDTms

With the dephasing dynamics of individual nanostructures confirmed by FDTD simulation, Au-NDTms with various PoT were fabricated to experimentally explore

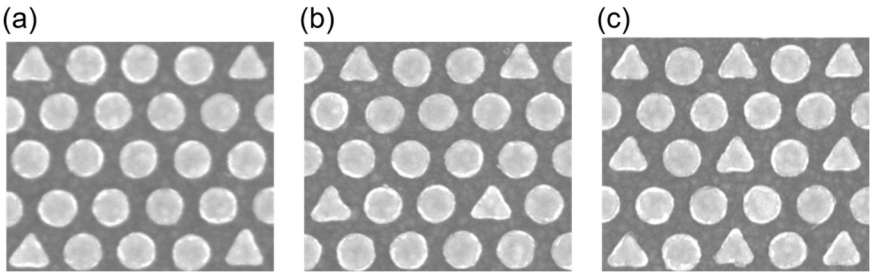

Figure 4.2 SEM images of Au-NDTms with PoTs of (a) 6%, (b) 11%, and (c) 25%.

their collective behavior. Each structure was designed with an individual nanoparticle diameter of 120 nm and an interparticle distance of 60 nm, corresponding to a PND of 36 and a surface coverage of approximately 40%. Representative SEM images of the fabricated Au-NDTms with three distinct PoTs are presented in **Figure 4.2**. As observed, the overall array periodicity and uniformity were well maintained across all PoTs, demonstrating the high reproducibility of the EBL process. The sharp tips of the Au-NTs are clearly visible, confirming the successful fabrication of tip-defined nanotriangles as designed. The proportion of Au-NTs within each array exactly matches the target PoT values, ensuring accurate structural control for subsequent optical and transient absorption measurements.

Notably, no significant aggregation or deformation of the triangular tips was detected, indicating that the optimized lithography parameters—especially the additional edge exposure dose and the thinner photoresist—were effective in preserving nanoscale tip sharpness. These structural characteristics are essential for realizing the desired faster dephasing and enhanced nonradiative damping, which are expected to play key roles in modulating quantum coherence within the modal strong coupling system.

4.3.3 spectral properties of the Au-NDTms

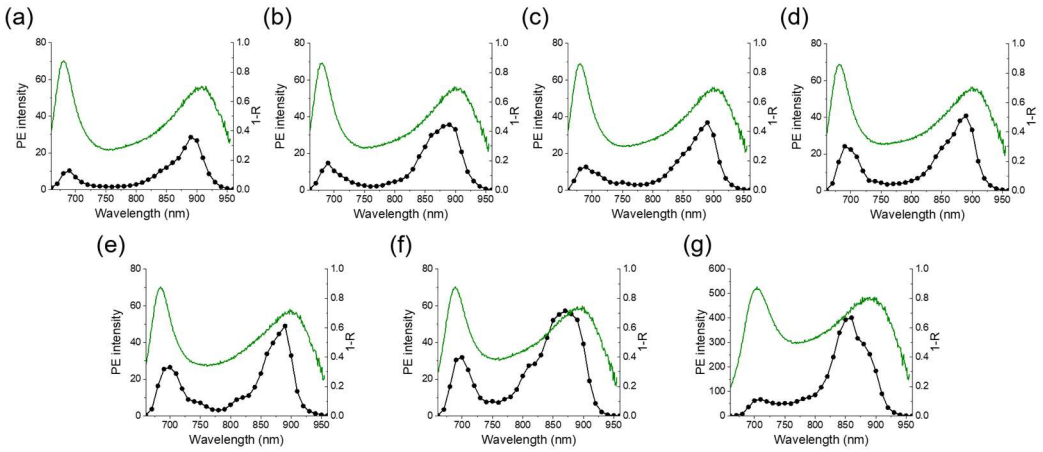

Figure 4.3 Absorption spectra (green, right Y-axis) and PE spectra (black, left Y-axis) for Au-NDTms with PoT of (a) 0%, (b) 4%, (c) 6%, (d) 11%, (e) 25%, (f) 50%, and (g) 100%. Note: the Pe intensity scale in (g) differs from those in the other panels.

Figure 4.3 presents the absorption spectra of the Au-NDTms, together with their corresponding PE spectra acquired by PEEM. From the absorption spectra, all Au-NDTms exhibit distinct energy splitting, confirming that the systems remain in the modal strong coupling regime even after the incorporation of fast-dephasing Au-NTs. Notably, as the PoT increases, the splitting energy gradually decreases, while the spectral bandwidth becomes broader. The corresponding dispersion curves are summarized in **Figure 4.4**, which clearly illustrate this reduction in mode separation and the concomitant broadening of the hybrid modes. This systematic trend can be attributed to the introduction of fast-dephasing Au-NTs, whose sharper tips induce stronger nonradiative damping and more efficient nonradiative decay channels. These processes effectively shorten the plasmonic coherence time, thereby reducing the coupling strength (g_1) between the plasmonic array and the FP nanocavity, and simultaneously broadening the resonance linewidth in accordance with the definition of the total damping rate.

On the other hand, the PE spectra also exhibit clear energy splitting, and the intensity of the lower branch is consistently stronger than that of the upper branch. Moreover, the overall PE intensity increases with increasing PoT, suggesting that the incorporation

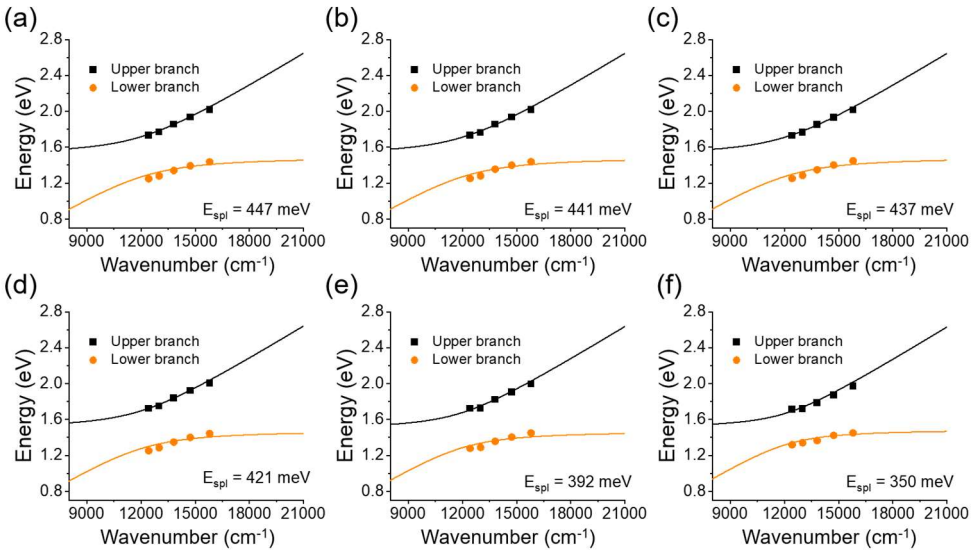

Figure 4.4 Dispersion curves of the Au-NDTms with PoT of (a) 0%, (b) 6%, (c) 11%, (d) 25%, (e) 50%, and (f) 100%.

of Au-NTs enhances the local near-field concentration and consequently the PE yield. When compared with the simulated near-field spectra shown in **Figure 4.5**, the experimentally observed enhancement in PE intensity is found to be much larger than expected from the total near-field amplitude alone. This discrepancy can be attributed to the strong field localization at the sharp tips of the Au-NTs. Because PE is a highly nonlinear process, scaling approximately with the third to fourth power of the near-field field amplitude ($|E|^{6-8}$), even a moderate concentration of near-field energy at the nanotriangle vertices can lead to a disproportionately large increase in PE intensity.

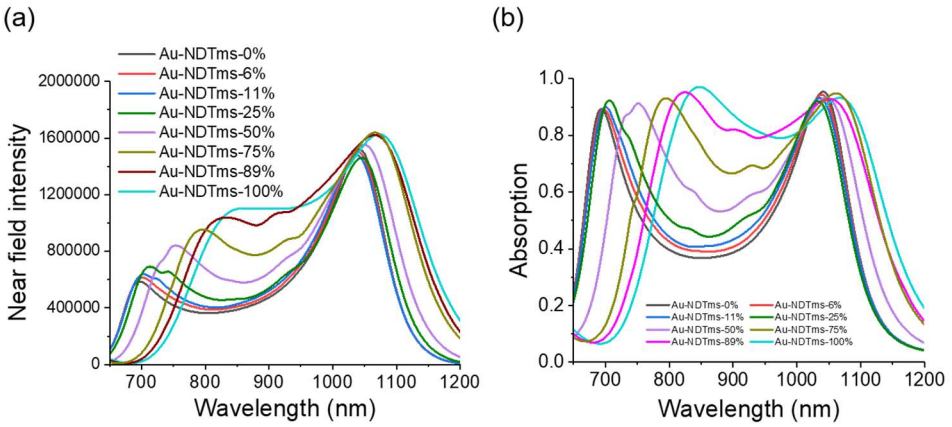

Figure 4.5 Simulated (a) near-field and (b) absorption spectra of Au-NDTms with various PoT values, obtained using FDTD simulations.

With the optical properties characterized, I will next proceed to evaluate the AQE of the Au-NDTms while systematically tuning the PoT.

4.3.4 PoT dependence on AQE

The TAS measurements were carried out to evaluate the photoexcited carrier dynamics of the Au-NDTms with different PoT. Representative transient decay profiles under lower-branch and upper-branch excitations of the ATA structures are presented in **Figure 4.6**(a,b), together with the reference AT structure excited at its LSPR band (**Figure 4.6**(c)). For all measurements, the pump power was fixed at 0.5 mW to ensure an adequate S/N ratio while avoiding photo-damage to the nanostructures. From the transient curves, distinct PoT-dependent trends are observed between the ATA and AT systems. In the AT structures, the ΔOD_{max} exhibits a monotonic increase with PoT, reflecting the stronger local field enhancement at the tips of Au-NTs. In contrast, the ATA structures display branch-dependent and nonmonotonic ΔOD_{max} dependences, suggesting the involvement of additional, coherence-related processes.

To quantify these differences, the AQEs of all samples were extracted from the transient signals and plotted as a function of PoT, as shown in **Figure 4.6**(d). Several noteworthy behaviors emerge: under the LSPR excitation of AT structures, the AQEs remain nearly constant across all PoTs, indicating that although Au-NTs generate stronger local near-fields at their tips, these enhancements are already accounted for in the absorption

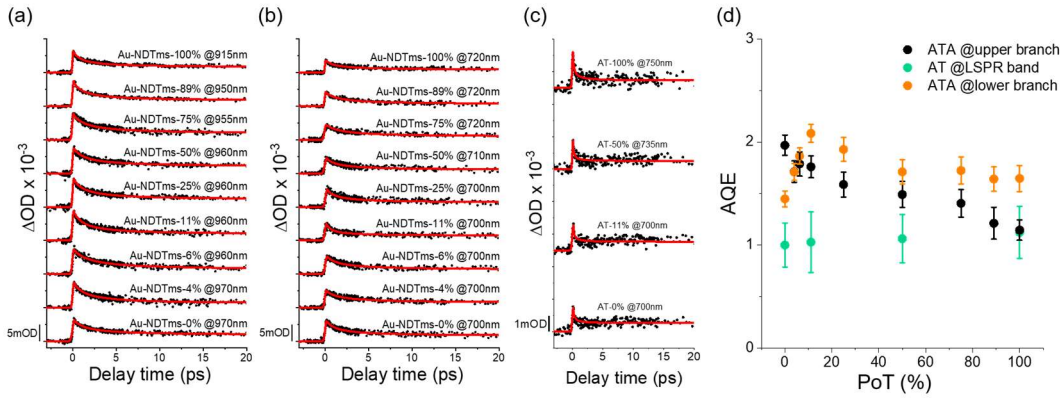

Figure 4.6 Transient absorption time profiles of (a) ATA pumped at the lower branch, (b) ATA pumped at the upper branch, and (c) AT pumped at the LSPR band. (d) AQE as a function of PoT, where all the values are normalized to the minimal AQE.

process and do not lead to higher carrier injection efficiency. This could be expected that in the absence of modal coherence, energy dissipation remains localized and incoherent.

On the other hand, under the lower-branch excitation of ATA structures, AQE initially increases for ~1.5 times with PoT and reaches a maximum around PoT ≈ 11%. When PoT further increases, AQE gradually decreases and eventually saturates at a level slightly higher than the original (PoT = 0%) value. This trend suggests the presence of competing mechanisms under lower-branch excitation, leading to the observed nonmonotonic dependence of AQE on PoT. In contrast, under the upper-branch excitation of ATA structures, AQE decreases almost monotonically with increasing PoT. This branch-dependent asymmetric AQE behavior is intriguing and unconventional warrants further investigation to elucidate the underlying mechanism of quantum coherence and the dephasing effect in the modal strong coupling system.

4.4 Conclusions

Au-NDTms structures incorporating relatively fast-dephasing Au-NTs within an Au-NDs array were successfully fabricated. Both the far-field absorption and near-field spectral measurements revealed clear energy splitting, confirming the realization of modal strong coupling. As the PoT increased, the coupling strength gradually decreased, accompanied by a broadening of the upper and lower branches. Notably, the AQE exhibited asymmetric, branch-dependent variations with PoT, which may arise from the interplay between quantum coherence and dephasing dynamics. These results indicate that the quantum coherence could play an important role in governing the hot-electron transfer efficiency under modal strong coupling. The possible mechanisms underlying this coherence-mediated behavior will be further explored in the next chapter.

4.5 References

1 Scully, M. O. & Zubairy, M. S. *Quantum optics*. Cambridge university press (1997).

2 Cohen-Tannoudji, C., Dupont-Roc, J. & Grynberg, G. *Atom-photon interactions: basic processes and applications*. John Wiley & Sons (2024).

3 Del Fatti, N. *et al.* Nonequilibrium electron dynamics in noble metals. *Physical Review B* **61**, 16956-16966, doi:10.1103/PhysRevB.61.16956 (2000).

4 Kreibig, U. & Vollmer, M. *Optical properties of metal clusters*. Vol. 25 Springer Science & Business Media (2013).

5 Auffèves-Garnier, A., Simon, C., Gérard, J.-M. & Poizat, J.-P. Giant optical nonlinearity induced by a single two-level system interacting with a cavity in the Purcell regime. *Physical Review A* **75**, 053823, doi:10.1103/PhysRevA.75.053823 (2007).

6 Zayats, A. V., Smolyaninov, I. I. & Maradudin, A. A. Nano-optics of surface plasmon polaritons. *Physics Reports* **408**, 131-314, doi:10.1016/j.physrep.2004.11.001 (2005).

7 Vasa, P. & Lienau, C. Strong Light–Matter Interaction in Quantum Emitter/Metal Hybrid Nanostructures. *ACS Photonics* **5**, 2-23, doi:10.1021/acsphotonics.7b00650 (2018).

8 Brown, A. M., Sundararaman, R., Narang, P., Goddard, W. A., 3rd & Atwater, H. A. Nonradiative Plasmon Decay and Hot Carrier Dynamics: Effects of Phonons, Surfaces, and Geometry. *ACS Nano* **10**, 957-966, doi:10.1021/acsnano.5b06199 (2016).

9 Cao, E. *et al.* Improving Charge Transfer under Strong Coupling Conditions via Interfacial Modulation. *ACS Photonics* **11**, 1205-1212, doi:10.1021/acsphotonics.3c01733 (2024).

10 Wang, L. *et al.* Wide-range control of surface plasmon dephasing time by the strong coupling between surface lattice and gap modes. *Opt Express* **33**, 8819-8829, doi:10.1364/oe.551591 (2025).

11 Niu, J. *et al.* Shifting of surface plasmon resonance due to electromagnetic coupling between graphene and Au nanoparticles. *Opt. Express* **20**, 19690-19696, doi:10.1364/OE.20.019690 (2012).

12 Krzemińska, Z., Jacak, J. E. & Jacak, W. A. On Damping of Plasmons and Plasmon-Polaritons in Metallic Nanostructures and Its Influence onto Numerical Simulations. *Plasmonics* **18**, 1211-1222, doi:10.1007/s11468-023-

01838-5 (2023).

13 Qin, Y., Xu, Y., Ji, B., Song, X. & Lin, J. Coaction effect of radiative and non-radiative damping on the lifetime of localized surface plasmon modes in individual gold nanorods. *The Journal of chemical physics* **158**, 104701, doi:10.1063/5.0134709 (2023).

14 Toffoletti, F. & Collini, E. Direct quantification of the plasmon dephasing time in ensembles of gold nanorods through two-dimensional electronic spectroscopy. *Nanoscale Advances* **7**, 1384-1390, doi:10.1039/D4NA00917G (2025).

15 Grześkiewicz, B., Ptaszyński, K. & Kotkowiak, M. Near and Far-Field Properties of Nanoprisms with Rounded Edges. *Plasmonics* **9**, 607-614, doi:10.1007/s11468-014-9671-x (2014).

16 Li, Y. *et al.* Correlation between Near-Field Enhancement and Dephasing Time in Plasmonic Dimers. *Physical Review Letters* **124**, 163901, doi:10.1103/PhysRevLett.124.163901 (2020).

17 Bosbach, J., Hendrich, C., Stietz, F., Vartanyan, T. & Träger, F. Ultrafast Dephasing of Surface Plasmon Excitation in Silver Nanoparticles: Influence of Particle Size, Shape, and Chemical Surrounding. *Physical Review Letters* **89**, 257404, doi:10.1103/PhysRevLett.89.257404 (2002).

18 Allard, T. F. & Weick, G. Quantum theory of plasmon polaritons in chains of metallic nanoparticles: From near- to far-field coupling regime. *Physical Review B* **104**, 125434, doi:10.1103/PhysRevB.104.125434 (2021).

19 Kong, X.-T., Wang, Z. & Govorov, A. O. Plasmonic Nanostars with Hot Spots for Efficient Generation of Hot Electrons under Solar Illumination. *Advanced Optical Materials* **5**, doi:10.1002/adom.201600594 (2017).

20 Kang, Y. *et al.* Effect of crystal facets in plasmonic catalysis. *Nature Communications* **15**, 3923, doi:10.1038/s41467-024-47994-y (2024).

21 Berenger, J.-P. A perfectly matched layer for the absorption of electromagnetic waves. *Journal of Computational Physics* **114**, 185-200, doi:10.1006/jcph.1994.1159 (1994).

22 Link, S. & El-Sayed, M. A. Spectral Properties and Relaxation Dynamics of Surface Plasmon Electronic Oscillations in Gold and Silver Nanodots and Nanorods. *The Journal of Physical Chemistry B* **103**, 8410-8426, doi:10.1021/jp9917648 (1999).

Chapter 5

Quantum coherence-mediated asymmetric hot carrier transfer in modal strong coupling systems

5.1 Introduction

In the previous chapter, Au-NDTms with tunable dephasing properties were successfully fabricated, and their optical responses were comprehensively characterized. Notably, asymmetric, branch-dependent AQE behaviors as a function of PoT were experimentally observed, suggesting that the efficiency of hot-carrier generation and transfer is influenced by factors beyond conventional light-matter coupling strength.

To elucidate the origin of these asymmetric features, this chapter focuses on the detailed investigation of the near-field distributions and the dephasing dynamics of Au-NDTms under lower and upper branch excitations. Through a combination of near-field simulations and experimental analyses, the interplay between quantum coherence, dephasing, and hot-carrier transfer is examined. Based on these results, a new mechanism of quantum coherence-mediated hot-carrier transfer is proposed, providing a coherent explanation for the observed asymmetric AQE behavior and offering new insight into the role of quantum coherence in modal strong coupling systems.

5.1.1 Natural photosynthesis and functional division of light-harvesting complexes

In **chapter 3**, I drew comparisons between the artificial modal strong coupling systems and natural photosynthesis, highlighting how coherence can govern energy transfer pathways. Building upon these insights, this chapter takes the comparison with natural photosynthesis from a qualitative analogy to a more concrete, function-level analysis. Therefore, I begin with a brief introduction of natural photosynthetic systems to establish the biological context for subsequent discussion. In nature, photosynthesis represents one of the most sophisticated examples of efficient light energy conversion.

Within photosynthetic organisms, solar energy is captured, transferred, and converted into chemical energy through a precisely orchestrated sequence of photophysical and photochemical events. The process begins in the light-harvesting antenna complexes (LHCs), which consist of pigment-protein assemblies that absorb incident photons over a broad spectral range. The absorbed excitonic energy is then funneled, through a series of highly efficient energy transfer processes[1], toward the reaction centers (RCs) — specialized molecular sites where charge separation and redox reactions occur, ultimately driving the conversion of light into chemical potential.

The functional division between LHCs and RCs is one of nature's most elegant design strategies. The antenna complexes act as optical "collectors," maximizing photon capture and ensuring that even weak or scattered light can be harvested. In contrast, the reaction centers function as "energy converters," where the localized excitons are rapidly separated into electrons and holes before recombination can occur. The success of this architecture arises not only from the structural arrangement but also from the presence of quantum coherence among the pigments, which allows excitons to migrate coherently across multiple sites within a few hundred femtoseconds before dephasing sets in[2-4]. This coherence-assisted energy migration ensures minimal energy loss and high transfer efficiency, with quantum yield approaching unity in some biological systems[5-8].

The discussion above underscores the critical role of dephasing in determining how excitations propagate and how efficiently energy can be utilized within a system. In plasmonic and modal strong coupling structures, dephasing similarly governs the temporal and spatial coherence of collective excitations, directly influencing the efficiency of hot-carrier generation and transfer. To rigorously investigate these effects, it is therefore essential to experimentally measure the dephasing times of the nanostructures, providing quantitative insight into how coherence evolves and dissipates under different structural and excitation conditions.

5.1.2 Dephasing time characterization

Experimental characterization of dephasing time poses an additional challenge

compared with the optical analyses, TAS measurements and PEC performance evaluations presented in the previous chapters. To date, various approaches have been employed to estimate the dephasing dynamics of plasmonic objects. The most common method involves evaluating the linewidth or full-width at half-maximum of a single-mode spectral peak obtained from extinction or scattering spectra, and relating it to the damping constant through Fourier-transform relations[9-11]. Others, for example, time-resolved pump-probe spectroscopy has been widely used to estimate coherence lifetimes from transient bleach recovery signals[12,13], while interferometric scattering (iSCAT) and Fourier-transform spectral interferometry techniques have provided indirect estimations of the plasmonic coherence decay through phase-sensitive detection[14,15]. However, most of these approaches rely heavily on model-dependent analysis or indirect spectral inference, making it difficult to experimentally visualize the actual dephasing process in the time domain.

In the past decade, PEEM has emerged as a powerful tool to directly observe plasmonic dephasing dynamics at the nanoscale. Unlike optical far-field measurements, PEEM enables real-space and time-resolved observation of PE signals induced by interfering ultrashort laser pulses[16,17]. In this technique, a pair of few-cycle pulses are used and temporally delayed with sub-femtosecond precision. When the delay time is an integer multiple of the optical wavelength ($n\lambda$), constructive interference occurs, resulting in strong PE intensity, whereas destructive interference appears at half-integer multiples $(n+1/2)\lambda$, leading to a significant suppression of the signal. By recording the PE intensity as a function of time delay, one obtains a temporal interference envelope, also known as the dephasing curve. This dephasing curve can then be analyzed using a damped harmonic oscillator model, allowing the extraction of the lifetime (or dephasing time) of the localized plasmonic mode. Through this approach, the ultrafast coherence decay can be directly measured in the time domain without relying solely on spectral approximations, thus providing a more reliable and experimentally grounded estimation of the dephasing characteristics of complex plasmonic systems.

5.2 Experimental details

5.2.1 Dephasing time measurement

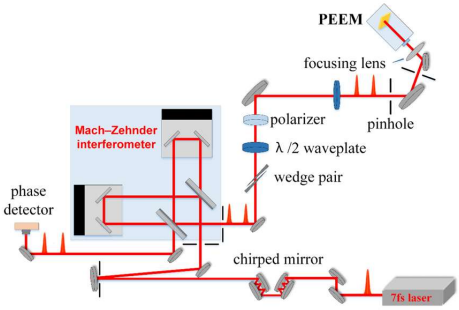

Figure 5.1 Schematic illustration of the dephasing time measurement using PEEM[19].

The dephasing times of Au-NDTms with different PoTs were quantitatively determined in this experiment using PEEM. Besides, PE spectra measurements and spatial distribution mappings under a small FOV were also performed using PEEM, following the procedure described in **Chapter 3**. In dephasing time measurement, an ultrafast laser system with a central wavelength of approximately 830 nm and a spectral bandwidth exceeding 200 nm was employed as the excitation source. After transmission through all optical components—including a 4/λ plate for generating circularly polarized light—the final pulse duration at the sample plane was optimized to ~7 fs, enabling delicate observation of the ultrafast dephasing dynamics (**Figure 5.1**)[18,19]. The total incident power was maintained at 70 mW, and the illuminated area was confined within a 30 μm-diameter FOV. The femtosecond pulses were divided into two temporally delayed replicas using a stabilized Mach-Zehnder interferometer, and the time delay between the two pulses was finely controlled in 0.104 μm steps. For each delay step, a PE image over the entire FOV was recorded. The integrated PE intensity as a function of delay time yielded the plasmon dephasing curve of the target structure, with four data points acquired per optical cycle to ensure temporal precision.

The dephasing dynamics were modeled using a damped harmonic oscillator model[20,21], expressed as:

$$E_l(t) \propto \int_{-\infty}^{t} \sum_j \frac{A_j}{\omega_j} (K(t') e^{-\gamma_j (t-t')} \sin\left[\omega_j (t-t')\right] dt'$$

where A_j and ω_j are the oscillator strength and resonance frequency of the j-th

mode, respectively, and $\gamma_j = 1/2\tau_i$ is the damping constant corresponding to the dephasing time τ_i. The driving term $K(t)$ represents the temporal interference of two time-delayed excitation pulses, defined as:

$$K(t) = E_0(t) + E_0(t + t_d)$$

where t_d is the time delay between the two pulses, with the electric field envelope of a single pulse given by:

$$E_0(t) = \mathrm{sech}[2\ln(1+\sqrt{2})t/T_0]\cos(\omega_0 t)$$

where T_0 = 7 fs denotes the pulse duration and ω_0 corresponds to the 830 nm central frequency. Since the PE process is inherently multiphotonic, the delay-dependent PE intensity $I(t_d)$ was calculated by integrating the nonlinear optical response over time:

$$I(t_d) \propto \int_{-\infty}^{+\infty} |E_l(t)|^{2N}\, dt$$

where the nonlinear order N was empirically determined from the PE intensity contrast at zero and infinite delay as:

$$N = \log_4\left[\frac{2I(0)}{I(\infty)}\right]$$

In the present Au-NDTm structures, two distinct plasmonic peaks were observed within the broad excitation bandwidth, corresponding to the lower and upper branches. To accurately model their temporal response, a two-component damped harmonic oscillator model was adopted, where the total plasmonic field was treated as the superposition of two temporally shifted oscillators. The resulting PE intensity was then computed based on the nonlinear power-law relation applied to the combined field[22,23]. This approach effectively captured the interference and coherence effects between the two strong coupling modes, enabling precise extraction of their respective dephasing times and providing insight into the branch-dependent coherence dynamics that govern hot-carrier transfer under modal strong coupling conditions.

5.3 Results and discussions

5.3.1 Branch-dependent near-field distribution patterns

To gain physical insight into the origin of the asymmetric AQE behavior, FDTD

simulations were performed to examine the near-field distributions of the Au-NDTms under different excitation conditions. Since the near-field intensity is proportional to the square of the local electric field, the spatial near-field patterns can be directly inferred from the simulated electric-field amplitude maps[24].

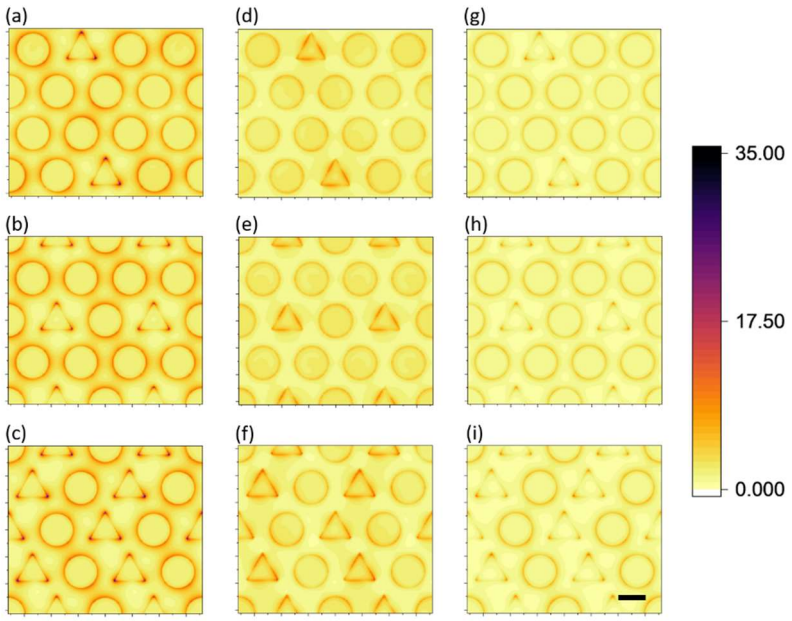

Figure 5.2 Simulated electric field distributions of ATA structures with PoT values of (a) 11%, (b) 25%, and (c) 50% under lower-branch excitation; (d)-(f) corresponding distributions under upper-branch excitation; and (g)-(h) those of AT structures with the same PoT values excited at the LSPR band. Note that for PoT = 11%, the displayed field map does not represent the exact simulation domain but is expanded to match the spatial scale of the other panels for visual comparison. The X and Y axes denote spatial coordinates (in nm), and the scale bar corresponds to 100 nm.

Figure 5.2 presents the simulated field distributions of Au-NDTms with three representative PoTs under (a-c) lower-branch excitation, (d-f) upper-branch excitation, and (g-h) LSPR excitation of the AT structures. For reference, the AT structures exhibit the typical plasmonic behavior expected from isolated nanostructures: the near-fields are localized at the particle rims corresponding to their absorption modes, with Au-NTs showing significantly stronger enhancement at their sharp tips than along their linear edges due to the classic "lightning-rod effect"[25]. In contrast, the ATA structures under modal strong coupling reveal distinctly branch-dependent field distributions. Under lower-branch excitation, the overall near-field intensities are noticeably higher than those under upper-branch excitation. The field enhancements are more uniformly

distributed across both Au-NDs and Au-NTs; and within this distribution, the Au-NTs still exhibit localized intensities at their sharp tips compared to their linear edges. Under upper-branch excitation, however, the spatial distribution drastically changes. The near-field intensities around Au-NDs become significantly weaker, whereas the fields at the Au-NTs dominate the system. Notably, the field maxima now shift from the tips toward the linear edges of the triangles. This branch-dependent redistribution of field localization reflects the asymmetric participation of the constituent nanostructures in the hybrid mode formation.

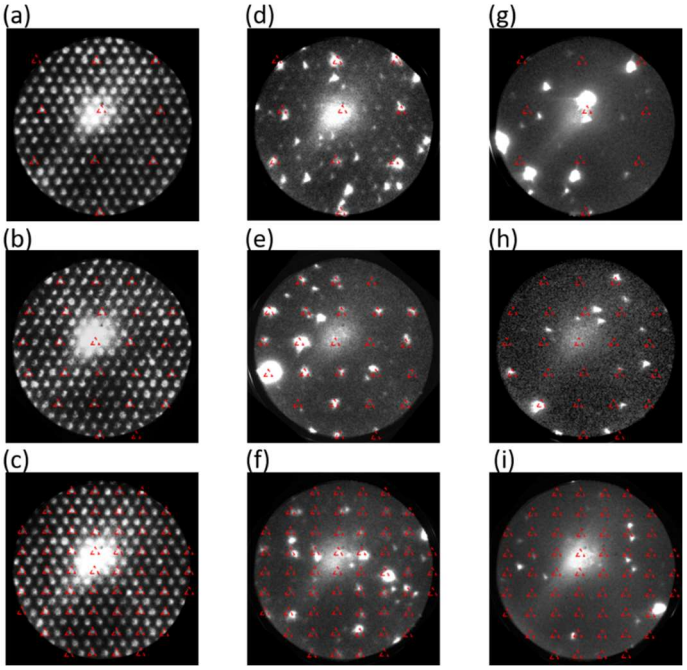

Figure 5.3 PEEM images of ATA structures with PoTs of (a) 6%, (b) 11%, and (c) 25% under 266 nm excitation, used to visualize all nanostructures. (d)-(f) Corresponding PEEM images acquired under upper-branch excitation, and (g)-(i) those under lower-branch excitation. The positions of Au-NTs are overlaid based on the identification from the 266 nm reference images.

The experimental observations obtained by PEEM support the simulation results. As shown in **Figure 5.3**, PE maps of the ATA structures (recorded within a 2.5 μm FOV) display similar branch-dependent contrasts. Under lower-branch excitation, the overall PE intensities are stronger, and the emission spots appear rather randomly distributed across both Au-NDs and Au-NTs. These slight spatial irregularities are likely attributed to structural imperfections introduced during fabrication; otherwise, the hot-spot

distribution should be more spatially uniform. Conversely, under upper-branch excitation, the total PE signal becomes weaker, but the emission is preferentially localized on the Au-NTs, consistent with the simulated near-field maps. These results clearly indicate that the near-field coupling topology and energy localization pathways in the ATA system are strongly dependent on the excitation branch. Such branch-dependent field distributions are expected to have a significant impact on the subsequent hot carrier generation and transfer dynamics, which will be discussed in the following sections.

5.3.2 Dephasing time characterization

To further elucidate the dephasing dynamics of ATA, the dephasing times of Au-NDTms with various PoTs were experimentally characterized by PEEM. As a reference, measurements were first performed on isolated single Au-NDs and single Au-NTs. Because recording the dephasing profile of an individual nanostructure is technically challenging owing to the extremely weak signal, sparse arrays of Au-NDs and Au-NTs were fabricated with an interparticle spacing of 3 μm—a distance much larger than the estimated coherence length. This large separation ensures that adjacent nanostructures reside well outside each other's coherence area, thereby eliminating quantum

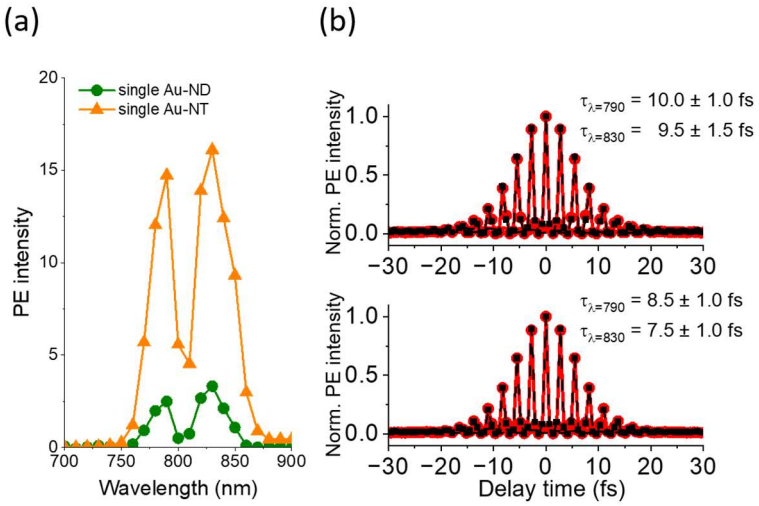

Figure 5.4 (a) PE spectra of a single Au-ND and a single Au-NT placed on an FP nanocavity. (b) Dephasing time profiles of a single Au-ND (top) and a single Au-NT (bottom) The red solid lines show the experimental data, while the black dashed lines indicate the fitted results.

coherence-induced coupling (g_2') and minimizing classical near-field coupling (g_2). At the same time, this configuration allows reliable signal collection within a 30 μm FOV during PEEM measurements. Under these conditions, each nanostructure behaves as an optically independent emitter, referred to hereafter as a "single Au-ND" or "single Au-NT."

Due to the extremely low surface coverage, far-field absorption spectra could not be reliably acquired. Nevertheless, the PE spectra of both single Au-NDs and single Au-NTs exhibited distinct energy splittings (**Figure 5.4**(a)), confirming that their LSPR modes remained coupled to the FP nanocavity (g_1) under a certain level even in the isolated condition. The dephasing time profiles extracted from these measurements are shown in **Figure 5.4**(b), with the fitted dephasing times noted therein. It is evident that the single Au-NTs exhibited shorter dephasing times ($\tau_{\lambda=790nm}$: 8.5 ± 1.0 fs, $\tau_{\lambda=830nm}$: 7.5 ± 1.0 fs) compared to single Au-NDs ($\tau_{\lambda=790nm}$: 10 ± 1.0 fs, $\tau_{\lambda=830nm}$: 9.5 ± 1.5 fs), in excellent agreement with both the FDTD simulations and theoretical expectations. These results confirm that the sharper edges and anisotropic geometry of Au-NTs indeed lead to enhanced damping and thus faster dephasing.

Subsequently, the dephasing time profiles for ATA structures with varying PoTs were obtained under both lower- and upper-branch excitations, as shown in **Figure 5.5**, and

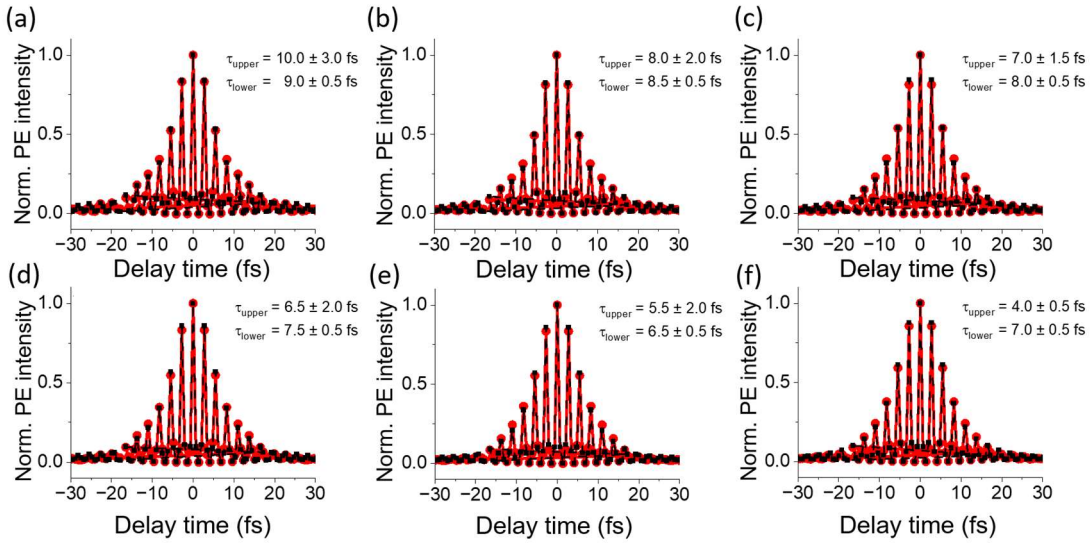

Figure 5.5 Dephasing time profiles of Au-NDTms with PoT of (a) 0%, (b) 6%, (c) 11%, (d) 25%, (e) 50%, and (f) 100%, respectively.

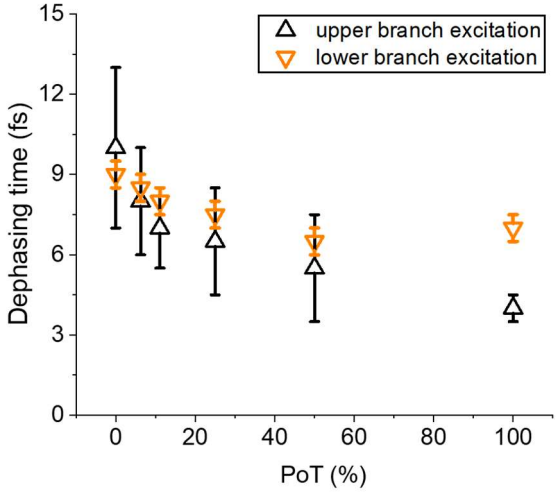

Figure 5.6 Dephasing time of ATA as a function of its PoT.

their extracted dephasing times are summarized in **Figure 5.6**. The results reveal that the dephasing times of ATA decrease concurrently for both branches when the PoT is below ~25%. Beyond this threshold, the dephasing times of the lower branch exhibit only slight variation, whereas those of the upper branch continue to decrease monotonically with increasing PoT. This trend can be rationalized by considering the anisotropic plasmonic coupling of Au-NTs. Compared with isotropic Au-NDs, Au-NTs support multiple spatially distinct plasmonic modes, each possessing different damping constants and radiative loss rates. As the PoT increases, these anisotropic interactions introduce mode mixing and spectral broadening, thereby accelerating the overall dephasing. Furthermore, the upper-branch excitation, being closer to the high-energy LSPR component, excites a larger number of spatial modes with stronger dispersion, resulting in a more pronounced reduction in dephasing time compared to the lower branch.

Because quantum coherence arises from the phase correlation among the nanostructures within a coherence area, faster dephasing directly implies a shorter coherence length and consequently a smaller coherence area[26]. Therefore, the observed PoT-dependent shortening of dephasing times—particularly under upper-branch excitation—indicates that increasing PoT progressively reduces the effective coherence area within the Au-NDTms array. This reduction limits the spatial extent over which delocalized energy

can propagate coherently, thereby decreasing the likelihood that energy reaches the efficient hot-electron transfer sites within the coherence area.

5.3.3 Quantum coherence-mediated mechanism for branch-dependent AQE

Based on the near-field distributions and dephasing characteristics discussed above, a new mechanism is proposed to explain the branch-dependent asymmetric AQE in the ATA system from the perspective of quantum coherence. Previous studies have demonstrated that localized electromagnetic fields are significantly enhanced at sites with high curvature or low coordination, such as the tips of Au nanorods or nanotriangles, where hot-carrier generation via nonradiative damping[27] becomes highly efficient. In our Au-NDTms system, it is therefore reasonable to regard the sharp tips of the Au-NTs as the most efficient hot-electron generation sites, followed by the rounded edges of the Au-NDs, while the flat, linear edges of the Au-NTs—lacking curvature—are the least efficient. On the other hand, the dephasing-time measurements revealed that single Au-NDs possess longer dephasing times than single Au-NTs, indicating that the Au-NDs exhibit higher optical quality factors (Q-factors)[28]. As a result, Au-NDs can be regarded as more effective optical antennas, capable of collecting and retaining incident energy for a longer period compared with Au-NTs. It is important to emphasize that the antenna efficiency does not necessarily correlate with optical absorption. While the optical antenna collects electromagnetic energy, this energy may subsequently dissipate via several decay channels, including radiative scattering and nonradiative processes such as Landau damping and electron-phonon relaxation. Among them, Landau damping is the dominant channel responsible for generating hot carriers, whereas optical absorption represents the integrated outcome of these nonradiative processes and thus reflects energy dissipation rather than energy retention[29]. Furthermore, under modal strong coupling, multiple nanostructures can acquire quantum coherence mediated by the FP nanocavity. The antenna effect is therefore extended beyond individual nanoparticles, spreading over the entire coherence area. When the dephasing time shortens with increasing PoT, the

corresponding coherence area contracts, implying a reduced spatial extent of energy sharing among neighboring nanostructures[30,31]. Consequently, although local near-field intensities may remain high, the overall efficiency of energy redistribution within the coherence area decreases.

Integrating these findings, the complete mechanism can be described as follows. Under lower-branch excitation of the ATA, the LSPR energy tends to be delocalized across the coherence area through quantum coherence. When an Au-NT with a shorter dephasing time is included within this coherence area, its sharp tips act as "efficient fast-dephasing sites," funneling the shared plasmonic energy toward regions of intense near-field localization. For Au-NDTms with PoT values between 0-11%, each coherence area statistically contains at most one Au-NT, and some may contain none. As PoT increases, the probability of including an Au-NT within a coherence area rises, expanding its influence on the overall region. Considering that the coherence area estimated in **Chapter 3** is approximately 460-495 nm, a PoT of ~11% corresponds to roughly one Au-NT per coherence area. At this composition, the dephasing time shortens by only ~16% relative to the PoT = 0% case, yet the AQE reaches its maximum because most of the delocalized energy converges to the Au-NT tips where hot-electron generation is most efficient. When the PoT exceeds 11%, multiple Au-NTs coexist within each coherence area. The LSPR energy, while still shared across the coherence area, preferentially converges to one of these Au-NTs, should lead to saturation in the AQE. However, because increasing PoT simultaneously decreases the number of Au-NDs that act as effective antennas, the system's overall energy-harvesting capacity declines. This trade-off between the increasing number of efficient reaction sites (Au-NTs) and the decreasing number of effective antennas (Au-NDs) causes a gradual decline and eventual saturation of the AQE at a level above its initial value.

In contrast, under upper-branch excitation, the LSPR energy preferentially localizes along the flat linear edges of Au-NTs, which are inefficient sites for hot-carrier generation even compared with the rounded edges of Au-NDs. Therefore, whether a coherence area includes fewer than one (PoT < 11%) or multiple (PoT > 11%) Au-NTs, their presence does not enhance the AQE. Instead, as PoT increases, these less efficient

Au-NTs progressively replace Au-NDs, leading to a monotonic decline in AQE. Moreover, the faster dephasing observed under upper-branch excitation results in a smaller coherence area, which further diminishes both the spatial extent of the antenna effect and the probability of including efficient sites. At high PoT (>75%), most coherence areas contain only one or fewer Au-NDs, and their scarcity leads to the loss of both active sites and collective antenna effects, producing a sharp decline in AQE.

In summary, under lower-branch excitation in the modal strong coupling ATA, long-dephasing Au-NDs act as energy-harvesting antennas with high Q-factors, while the delocalized plasmonic energy is funneled toward the sharp tips of the Au-NTs, where low-coordinated regions facilitate efficient hot-carrier generation through nonradiative damping (**Figure 5.7**). This complementary functional division—Au-NDs serving as energy collectors and Au-NTs as reaction centers—bears a striking resemblance to the antenna complexes and reaction centers in natural photosynthesis[1,32-34]. In contrast, under upper-branch excitation, the near-field distribution becomes concentrated along the less efficient linear edges of the Au-NTs, so the increase of PoT indicates the reduction of both collective antennas and efficient sites. The distinct distribution

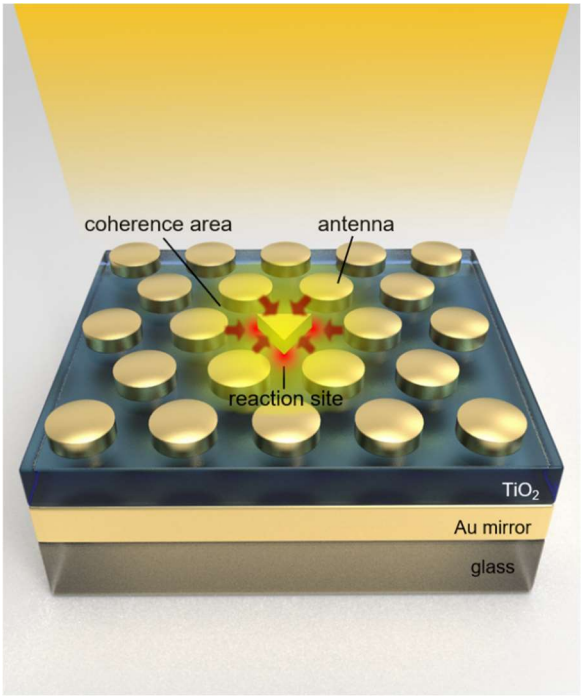

Figure 5.7 Schematic illustration of the quantum coherence-mediated hot electron transfer process.

patterns of near-fields between branches and nanostructures result in asymmetric, branch-dependent AQE behaviors that are unique in quantum coherence-mediated modal strong coupling ATA systems and are absent in conventional LSPR-based AT structures.

5.4 Conclusions

In conclusion, these investigations demonstrate that the AQE behavior in the modal strong coupling ATA system is delicately governed by the intricate interplay among near-field spatial distribution, quantum coherence, and dephasing dynamics. The combination of near-field mapping and dephasing analyses elucidates a coherent mechanism: Au-NDs, exhibiting relatively long dephasing times and high Q-factors, function as **efficient energy-harvesting antennas** that collect and retain plasmonic energy, whereas the sharp tips of the Au-NTs act as the **principal sites for hot-electron generation**.

Under lower-branch excitation, the delocalized plasmonic energy is coherently shared within a coherence area. As the PoT increases, more Au-NT sharp tips are incorporated into this coherence area, allowing the collected energy to be funneled efficiently toward these active sites. However, the simultaneous reduction in the number of Au-NDs decreases the system's overall light-harvesting capacity. The competition between these two effects leads to a characteristic evolution of the AQE: it first increases with PoT, reaches a maximum around PoT = 11%, and then gradually decreases, eventually saturating at a level still higher than the initial one. In contrast, under upper-branch excitation, the plasmonic energy is preferentially localized along the linear edges of Au-NTs, which are inefficient for hot-carrier generation even compared with the rounded edges of Au-NDs. Furthermore, the concurrent reduction in coherence area and the number of effective antennas progressively suppress both energy delocalization and hot-carrier generation, resulting in a monotonic decline in AQE with increasing PoT.

Collectively, these findings provide deeper insight into how quantum coherence governs the energy redistribution pathways in heterogeneous plasmonic systems under modal strong coupling. Beyond serving as a collective optical phenomenon, quantum

coherence enables dissimilar nanostructures to assume complementary roles as energy collectors and reaction centers—an artificial analogue to the light-harvesting complexes and reaction centers in natural photosynthesis. This conceptual framework not only deepens the understanding of coherence-assisted photochemical processes but also establishes a new design principle for next-generation strong-coupling photoelectrodes. Such coherence-mediated architectures hold great promise for advancing the efficiency of artificial photosynthesis and other light-driven energy conversion systems.

5.5 References

1 Engel, G. S. *et al.* Evidence for wavelike energy transfer through quantum coherence in photosynthetic systems. *Nature* **446**, 782-786, doi:10.1038/nature05678 (2007).

2 Collini, E. *et al.* Coherently wired light-harvesting in photosynthetic marine algae at ambient temperature. *Nature* **463**, 644-647, doi:10.1038/nature08811 (2010).

3 Ishizaki, A. & Fleming, G. R. Theoretical examination of quantum coherence in a photosynthetic system at physiological temperature. *Proceedings of the National Academy of Sciences* **106**, 17255-17260, doi:10.1073/pnas.0908989106 (2009).

4 Harel, E. & Engel, G. S. Quantum coherence spectroscopy reveals complex dynamics in bacterial light-harvesting complex 2 (LH2). *Proceedings of the National Academy of Sciences* **109**, 706-711, doi:10.1073/pnas.1110312109 (2012).

5 Romero, E. *et al.* Quantum coherence in photosynthesis for efficient solar-energy conversion. *Nature Physics* **10**, 676-682, doi:10.1038/nphys3017 (2014).

6 Scholes, G. D. *et al.* Using coherence to enhance function in chemical and biophysical systems. *Nature* **543**, 647-656, doi:10.1038/nature21425 (2017).

7 Panitchayangkoon, G. *et al.* Long-lived quantum coherence in photosynthetic complexes at physiological temperature. *Proceedings of the National Academy*

of Sciences **107**, 12766-12770, doi:10.1073/pnas.1005484107 (2010).

8 Ishizaki, A. & Fleming, G. R. Quantum Coherence in Photosynthetic Light Harvesting. *Annual Review of Condensed Matter Physics* **3**, 333-361, doi:10.1146/annurev-conmatphys-020911-125126 (2012).

9 Bosbach, J., Hendrich, C., Stietz, F., Vartanyan, T. & Träger, F. Ultrafast Dephasing of Surface Plasmon Excitation in Silver Nanoparticles: Influence of Particle Size, Shape, and Chemical Surrounding. *Physical Review Letters* **89**, 257404, doi:10.1103/PhysRevLett.89.257404 (2002).

10 Hoggard, A. *et al.* Using the plasmon linewidth to calculate the time and efficiency of electron transfer between gold nanorods and graphene. *ACS Nano* **7**, 11209-11217, doi:10.1021/nn404985h (2013).

11 Olson, J. *et al.* Optical characterization of single plasmonic nanoparticles. *Chemical Society Review* **44**, 40-57, doi:10.1039/c4cs00131a (2015).

12 Grumstrup, E. M. *et al.* Ultrafast Carrier Dynamics in Individual Silicon Nanowires: Characterization of Diameter-Dependent Carrier Lifetime and Surface Recombination with Pump–Probe Microscopy. *The Journal of Physical Chemistry C* **118**, 8634-8640, doi:10.1021/jp502737e (2014).

13 Dong, P.-T. & Cheng, J. X. Pump-probe microscopy: Theory, instrumentation, and applications. *Spectroscopy (Santa Monica)* **32**, 24-36 (2017).

14 Velasco, L., Islam, A. N., Kundu, K., Oi, A. & Reinhard, B. M. Two-color interferometric scattering (iSCAT) microscopy reveals structural dynamics in discrete plasmonic molecules. *Nanoscale* **16**, 11696-11704, doi:10.1039/D4NR01288G (2024).

15 Ortega-Arroyo, J. & Kukura, P. Interferometric scattering microscopy (iSCAT): new frontiers in ultrafast and ultrasensitive optical microscopy. *Physical Chemistry Chemical Physics* **14**, 15625-15636, doi:10.1039/C2CP41013C (2012).

16 Sun, Q. *et al.* Direct imaging of the near field and dynamics of surface plasmon resonance on gold nanostructures using photoemission electron microscopy. *Light: Science & Applications* **2**, e118-e118, doi:10.1038/lsa.2013.74 (2013).

17 Koo, N. T. W., Woo, K. C., Lim, J. W. X. & Loh, Z.-H. Lifetime mapping using femtosecond time-resolved photoemission electron microscopy. *The Journal of chemical physics* **161**, 174201, doi:10.1063/5.0232059 (2024).

18 Sun, Q., Zu, S. & Misawa, H. Ultrafast photoemission electron microscopy: Capability and potential in probing plasmonic nanostructures from multiple domains. *The Journal of chemical physics* **153**, 120902, doi:10.1063/5.0013659 (2020).

19 Li, Y. *et al.* Correlation between Near-Field Enhancement and Dephasing Time in Plasmonic Dimers. *Physical Review Letters* **124**, 163901, doi:10.1103/PhysRevLett.124.163901 (2020).

20 Lamprecht, B., Krenn, J. R., Leitner, A. & Aussenegg, F. R. Resonant and Off-Resonant Light-Driven Plasmons in Metal Nanoparticles Studied by Femtosecond-Resolution Third-Harmonic Generation. *Physical Review Letters* **83**, 4421-4424, doi:10.1103/PhysRevLett.83.4421 (1999).

21 Sun, Q. *et al.* Dissecting the Few-Femtosecond Dephasing Time of Dipole and Quadrupole Modes in Gold Nanoparticles Using Polarized Photoemission Electron Microscopy. *ACS Nano* **10**, 3835-3842, doi:10.1021/acsnano.6b00715 (2016).

22 Ishioka, K. *et al.* Selective coupling of coherent optical phonons in $YBa_2Cu_3O_{7-\delta}$ with electronic transitions. *Physical Review B* **107**, 184302, doi:10.1103/PhysRevB.107.184302 (2023).

23 Xu, Y. *et al.* Flexible manipulation of plasmon dephasing time via the adjustable Fano asymmetric dimer. *Photon. Research* **10**, 2267-2277, doi:10.1364/PRJ.460638 (2022).

24 Yu, H. *et al.* Exploring Coupled Plasmonic Nanostructures in the Near Field by Photoemission Electron Microscopy. *ACS Nano* **10**, 10373-10381, doi:10.1021/acsnano.6b06206 (2016).

25 Ermushev, A. V., Boris, V. M., Oleĭnikov, V. A. & Petukhov, A. V. Surface enhancement of local optical fields and the lightning-rod effect. *Quantum Electronics* **23**, 435, doi:10.1070/QE1993v023n05ABEH003090 (1993).

26 Moix, J. M., Khasin, M. & Cao, J. Coherent quantum transport in disordered systems: I. The influence of dephasing on the transport properties and absorption spectra on one-dimensional systems. *New Journal of Physics* **15**, 085010, doi:10.1088/1367-2630/15/8/085010 (2013).

27 Kang, Y. *et al.* Effect of crystal facets in plasmonic catalysis. *Nature Communications* **15**, 3923, doi:10.1038/s41467-024-47994-y (2024).

28 Gustafsson, M. & Nordebo, S. *Bandwidth, Q factor, and resonance models of antennas*. Vol. TEAT-7138 (2005).

29 Brongersma, M. L., Halas, N. J. & Nordlander, P. Plasmon-induced hot carrier science and technology. *Nature Nanotechnology* **10**, 25-34, doi:10.1038/nnano.2014.311 (2015).

30 Wang, B. *et al.* High-Q Plasmonic Resonances: Fundamentals and Applications. *Advanced Optical Materials* **9**, 2001520, doi:10.1002/adom.202001520 (2021).

31 Hergert, G. *et al.* Long-lived electron emission reveals localized plasmon modes in disordered nanosponge antennas. *Light: Science & Applications* **6**, e17075-e17075, doi:10.1038/lsa.2017.75 (2017).

32 Scholes, G. D., Fleming, G. R., Olaya-Castro, A. & van Grondelle, R. Lessons from nature about solar light harvesting. *Nature Chemistry* **3**, 763-774, doi:10.1038/nchem.1145 (2011).

33 Brédas, J.-L., Sargent, E. H. & Scholes, G. D. Photovoltaic concepts inspired by coherence effects in photosynthetic systems. *Nature Materials* **16**, 35-44, doi:10.1038/nmat4767 (2017).

34 Rather, S. R. & Scholes, G. D. From Fundamental Theories to Quantum Coherences in Electron Transfer. *Journal of the American Chemical Society* **141**, 708-722, doi:10.1021/jacs.8b09059 (2019).

Chapter 6

Conclusions and future perspectives

6.1 Conclusions

In this thesis, modal strong coupling systems between localized surface plasmon resonance (LSPR) and Fabry-Pérot (FP) nanocavity modes were successfully established by integrating well-designed Au nanodisks (Au-NDs) or mixed Au ND-nanotriangle (NT) (Au-NDTm) arrays on FP nanocavities. These hybrid structures—referred to as ATAs—exhibited clear energy splitting in their absorption spectra, satisfying the criterion for strong coupling. Their absorption intensity and near-field intensity both displayed saturation with increasing particle number density (PND), and the photoemission mappings revealed a distinctive rim-bright and center-dark field distribution pattern that is absent in conventional LSPR Au-NDs/TiO_2 (AT) structures. By systematically tuning the PND of the Au-NDs, the apparent quantum efficiency (AQE), which reflects the hot-electron injection efficiency evaluated by transient absorption spectroscopy (TAS), showed a positive correlation with PND. In contrast, the AQE of conventional LSPR AT structures remained nearly independent of PND. This enhancement of AQE, together with the observed spectral saturation and unique near-field pattern, provides compelling evidence for the involvement of **quantum coherence** in the modal strong coupling system. Within the coherence area supported by the FP nanocavity, individual Au-NDs can coherently interact and share LSPR energy. Such collective coupling enables energy harvested by one Au-ND to be funneled toward a spatially distinct, fast-damping site, facilitating efficient hot-electron generation even in nanostructures not directly excited by incident light.

The coherence area was quantitatively estimated by correlating the square-root dependence between the energy splitting and PND with that of a single Au-ND. The coherence area was found to be a circular area with a diameter of approximately 460-495 nm. Furthermore, the positive deviation of splitting energy from the ideal square-root trend at higher PND values can be attributed to additional coupling among Au-

NDs through FP nanocavity mediated by quantum coherence. These findings establish that the modal strong coupling in Au-ND ATAs is not merely a photonic phenomenon but also a manifestation of coherent plasmonic interactions extending across hundreds of nanometers.

When fast-dephasing Au-NTs were intentionally incorporated into the Au-ND arrays to construct Au-NDTms, the hybrid ATA system retained the characteristics of strong coupling, showing pronounced spectral splitting. However, the spectral bandwidth broadened with increasing percentage of triangles (PoT), reflecting the faster dephasing dynamics introduced by Au-NTs. Most notably, the AQE of the ATA exhibited a **branch-dependent and asymmetric dependence on PoT**, whereas the conventional AT system remained nearly invariant with PoT.

The lower-branch excitation produced nearly uniform near-field distributions across the structure, with intense localization at the sharp tips of Au-NTs—sites known for efficient hot-carrier generation through nonradiative damping. Conversely, under upper-branch excitation, the near-fields were preferentially confined along the linear edges of Au-NTs, which are inefficient for carrier generation. Dephasing analysis revealed that the coherence area shrank a bit with increasing PoT, and the reduction was more pronounced for the large PoT regime under upper-branch excitation. Consequently, under lower-branch excitation, long-dephasing Au-NDs acted as **effective optical antennas** that collected and retained energy, while the sharp Au-NT tips within the coherence area served as **efficient reaction sites**. The interplay between these two roles resulted in an AQE that increased with PoT, peaked at PoT = 11%, and then gradually decreased to a saturated value higher than the initial one. Under upper-branch excitation, however, the AQE decreased monotonically with increasing PoT, owing to the replacement of efficient Au-ND antennas by inefficient Au-NTs and the concurrent reduction in coherence area and dephasing time.

Overall, this thesis elucidates the **underlying mechanism of modal strong coupling and quantum coherence** in modal strong coupling systems. It establishes that the observed optical and photochemical responses arise from a coherent interplay between near-field spatial distributions, dephasing dynamics, and the extent of quantum

coherence. Furthermore, it highlights how heterogeneous nanostructures—through modal strong coupling—can assume complementary roles analogous to those found in natural photosynthetic complexes: Au-NDs act as energy-harvesting antennas, while Au-NTs serve as catalytic reaction sites. This coherent division of functionality presents a great applicability in photoelectrochemical (PEC) reactions.

6.2 Future perspectives

The present study has provided valuable insights into the mechanisms and manifestations of modal strong coupling and quantum coherence within plasmonic-photonic hybrid systems. Nevertheless, as these concepts remain relatively new and complex, many fundamental questions are yet to be answered. So far, my research has primarily focused on the dependence of coupling and coherence behaviors on PND and dephasing dynamics, PoT. In the future, it will be essential to explore additional variables—such as the choice of plasmonic materials (e.g., Ag, Al, or Cu), the refractive index of surrounding dielectrics, cavity geometry, and even temperature or external field modulation—to further clarify the underlying physical mechanisms. These efforts will contribute to a more complete understanding of how modal strong coupling strength and coherence area can be precisely tuned.

In terms of quantitative analysis, the coherence area discussed in this work has so far been inferred from theoretical correlations and spectral trends, without direct experimental visualization. Future research should therefore aim to experimentally validate and map coherence areas. Such studies could reveal the spatial and temporal evolution of coherence in real time and help identify the key parameters—such as local field enhancement, cavity Q-factor, or plasmon dephasing dynamic—that determine the extent of coherent interactions.

From an application perspective, the established modal strong coupling structures hold great promise as efficient photoelectrodes capable of harvesting visible and near-infrared light. A deeper understanding of the underlying quantum coherence mechanisms will enable the rational design of coherence-assisted photocatalytic platforms. With the advancement of nanofabrication, ultrafast spectroscopy, and surface

chemistry, it is foreseeable that future systems could achieve orders-of-magnitude improvement in light-to-charge conversion efficiency. Ultimately, such progress may pave the way toward the realization of high-efficiency, scalable artificial photosynthetic systems, offering a sustainable pathway for converting solar energy into chemical fuels and contributing to the broader utilization of renewable energy.

Publication lists

1. **Yen-En Liu**, Xu Shi, Tomohiro Yokoyama, Soshun Inoue, Yuji Sunaba, Tomoya Oshikiri, Quan Sun, Mamoru Tamura, Hajime Ishihara, Keiji Sasaki, Hiroaki Misawa,
   "Quantum-Coherence-Enhanced Hot-Electron Injection under Modal Strong Coupling"
   ACS Nano **2023**, 17, 9, 8315-8323, doi:10.1021/acsnano.2c12670
2. **Yen-En Liu**, Xu Shi, Yaolong Li, Tomoya Oshikiri, Yasutaka Matsuo, Soshun Inoue, Hajime Ishihara, Keiji Sasaki, Hiroaki Misawa,
   "Asymmetric Hot-Carrier Transfer Mediated by Quantum Coherence in Au Nanodisk–Nanotriangle Arrays"
   ACS Photonics **2025**, 12, 12, 6994-7001, doi:10.1021/acsphotonics.5c02320
3. Xiaoqian Zang, Xu Shi, Yoshiki Suganami, **Yen-En Liu**, Tomoya Oshikiri, Hiroaki Misawa,
   "Investigation of Enhanced Water Oxidation under Plasmon-Nanocavity Strong Coupling Using In Situ Electrochemical Surface-Enhanced Raman Spectroscopy"
   J. Phys. Chem. C **2023**, 127, 31, 15087-15095, doi:10.1021/acs.jpcc.3c03625
4. Yoshiki Suganami, Tomoya Oshikiri, Hideyuki Mitomo, Keiji Sasaki, **Yen-En Liu**, Xu Shi, Yasutaka Matsuo, Kuniharu Ijiro, Hiroaki Misawa,
   "Spatially Uniform and Quantitative Surface-Enhanced Raman Scattering under Modal Ultrastrong Coupling Beyond Nanostructure Homogeneity Limits"
   ACS Nano **2024**, 18, 6, 4993-5002, doi:10.1021/acsnano.3c10959
5. En Cao, Xu Shi, Tomoya Oshikiri, **Yen-En Liu**, Quan Sun, Keiji Sasaki, Hiroaki Misawa,

"Improving Charge Transfer under Strong Coupling Conditions via Interfacial Modulation"

ACS Photonics **2024**, 11, 3, 1205-1212, doi:10.1021/acsphotonics.3c01733

6. En Cao, Xu Shi, Haruo Inoue, Tomoya Oshikiri, **Yen-En Liu**, Hiroaki Misawa, "Activation Energy in the Electron Transfer Process and Water Oxidation Intermediate Generation under Plasmon-Nanocavity Strong Coupling"

   J. Phys. Chem. C **2025**, 129, 3, 1590-1597, doi:10.1021/acs.jpcc.4c07398